

The Atmospheric Circulation of Tidally Locked Terrestrial Exoplanets



Mark Hammond
Hertford College
University of Oxford

A thesis submitted for the degree of
Doctor of Philosophy
Michaelmas Term 2019

Acknowledgements

Abstract

This thesis aims to better understand the atmospheric circulation and global temperature distribution of tidally locked planets, and to apply this to interpreting the observed temperature distribution of the tidally locked “lava planet” 55 Cancri e.

The first two chapters address the atmospheric dynamics of tidally locked planets. Chapter 1 uses the Gierasch-Rossow-Williams mechanism to explain the angular momentum budget of the atmospheres of tidally locked planets, and to predict the formation of different zonal flow patterns. Chapter 2 uses a shallow-water model linearised about an equatorial jet to show how this zonal flow produces the global circulation pattern seen in GCM simulations, particularly the hot-spot shift seen in observations.

The last two chapters apply this theory to direct and interpret simulations of 55 Cancri e, for comparison with an observed thermal phase curve. Chapter 3 uses an idealised three-dimensional atmospheric model to simulate atmospheres with different bulk properties, to test predictions of how this should affect the global circulation and phase curve. Chapter 4 uses a model with more realistic radiative transfer to run similar tests and simulate spectrally resolved observations. These chapters will conclude that the thermal phase curve is evidence of an atmosphere that is heavier than H₂ and thicker than 10 bar.

I will conclude by summarising the proposed theory for the formation of zonal flow on tidally locked planets, and how this flow produces observable effects. I will suggest that this allows us to interpret climate observations in terms of the large-scale properties of the planet and its atmosphere.

Contents

Introduction	1
Review: The Atmospheres of Hot, Tidally Locked Planets	4
1 The Gierasch-Rossow-Williams Mechanism on Tidally Locked Planets	19
1.1 Linear Shallow-Water Model of a Tidally Locked Planetary Atmosphere	20
1.2 The Meridional Circulation on a Tidally Locked Planet	29
1.3 Non-Linear Model of the Meridional and Zonal Circulation on a Tidally Locked Planet	43
1.4 Scaling Regimes for Zonal Jets on Tidally Locked Planets	48
1.5 Discussion	52
1.6 Conclusions	54
2 Wave-Mean Flow Interactions in a Linear Theory of Tidally Locked At- mospheres	55
2.1 Linear Shallow-Water System in Zonal Flow	56
2.2 Free Modes in Shear Flow on the Beta-Plane	59
2.3 Forced Response in Shear Flow on the Beta-Plane	65
2.4 Wave Interactions with Shear Flow on a Sphere	70
2.5 Scaling Relations	74
2.6 Discussion	79
2.7 Conclusion	82
3 Linking the Climate and Thermal Phase Curve of 55 Cancri e	85
3.1 Observations of 55 Cancri e	87
3.2 Simplified Scaling Theory	92
3.3 Simulating a Lava Planet	97
3.4 Results	99
3.5 Simulated Observations	109
3.6 Discussion	116
3.7 Conclusions	117
4 Realistic Modelling of Lava Planets	119
4.1 An Improved Lava Planet GCM	121

4.2	Control Simulations	123
4.3	Best-Fit Simulation	131
4.4	100 bar Simulation	136
4.5	Discussion	139
4.6	Conclusions	144
	Conclusions	145
	Bibliography	149
A	Exo-FMS	157
A.1	Structure	157
A.2	Finite-Volume Dynamical Core	159
B	Pseudo-Spectral Methods for the Shallow-Water Equations	161
B.1	Pseudo-Spectral Collocation Method for a Single Equation	161
B.2	Beta-Plane Shallow Water Equations	163
B.3	Spherical Shallow-Water Equations	165

List of Figures

0.1	The population of known exoplanets plotted by semi-major axis and stellar mass. All the planets below the line have a timescale to reach a tidally locked state of less than 0.1 billion years, so are expected to be in this state.	2
0.2	The population of known exoplanets plotted by planetary radius and orbital period. The planets are labelled by the method used to discover them.	6
0.3	Figure from Leconte et al. (2015) showing the effect of atmospheres of 1 or 10 bar on the spin state of Earth-like planets, demonstrating that a thin atmosphere can prevent some planets from becoming tidally locked.	10
0.4	The thermal phase curve observed at 4.5 μm by Demory et al. (2016) , showing an offset of the maximum flux from the secondary eclipse, corresponding to a hot-spot shift.	13
0.5	The temperature map reconstructed by Demory et al. (2016) from the phase curve in Figure 3.2, showing a a hot-spot shift of 41°, a day-side temperature of (2700 ± 270) K, and a night-side temperature of (1380 ± 400) K.	13
0.6	The global temperature field at 500 mbar of a simulation of a tidally locked Earth-sized planet with a 10 day rotation period and a 1 bar N_2 atmosphere, showing an eastward shifted hot-spot and night-side cold stationary waves, reproduced from Pierrehumbert and Hammond (2018)	18
1.1	The height and velocity fields of the lowest order free modes of a shallow-water system on an equatorial beta-plane.	22
1.2	Response of Equation 1.3 to forcing $Q(x, y) = Q_0 \sin(x) e^{-y^2/2}$, showing the maximum of the Rossby wave west of the maximum of the forcing (i.e. the substellar point) and the maximum of the Kelvin wave east of this point.	24
1.3	Terms in the zonal-mean zonal momentum equation (Equation 1.11) without the correction R to the momentum.	25

1.4	Terms in the zonal-mean zonal momentum equation (Equation 1.11) with the correction R to the momentum.	27
1.5	The global circulation of a typical tidally locked Earth-like planet, with prograde zonal flow at all latitudes at the level of maximum jet flow.	31
1.6	The spin-up of angular momentum globally and at the pressure level of the jet, showing how both regions gain momentum over time then equilibrate.	32
1.7	The Gierasch-Rossow-Williams (GRW) mechanism as applied to tidally locked planets. The solid line shows the mean momentum transport, which produces subtropical jets at high latitudes. The dashed lines show the horizontal and vertical eddy momentum transports, which accelerate and decelerate the equatorial superrotation respectively.	33
1.8	The Fourier series of the realistic forcing.	35
1.9	Time-mean results from the first day after spin-up from rest of two tests in Exo-FMS. The top row shows a tidally locked planet, and the bottom row shows a planet with axisymmetric forcing with the same zonal mean. The zonal mean zonal velocity and mean mass streamfunction are the same in both cases, despite the large differences in the longitudinal distribution of zonal velocity.	37
1.10	Acceleration terms in the zonal-mean zonal momentum equation (Equation 1.11), with an imposed uniform zonal-mean meridional velocity $\bar{V}(y) = V_0 \sin y / y_0 e^{-y^2/2}$, showing prograde westerly acceleration at all latitudes.	38
1.11	The zonal-mean zonal velocity of the tidally locked planet in Test 1, and the axisymmetrically forced planet in Test 2, as they spin up from rest. .	40
1.12	Zonal velocity and drag	42
1.13	Mean and eddy acceleration.	42
1.14	Acceleration terms in the zonal-mean zonal momentum equation for Test 1 in Exo-FMS, showing how Terms Ia and IIa in Equation 1.21 balance at high latitudes, and that Term IIb balances Terms IIa and Ib at the equator (as in Figures 1.10 and 1.18).	43
1.15	Test A, sinusoidal forcing	47
1.16	Test B, axisymmetric forcing	47
1.17	Test C, realistic forcing	47
1.18	The terms in the zonal-mean zonal momentum equation (Equation 1.25) for Test 3 with realistic forcing in the non-linear shallow-water model, showing how balance is achieved differently at the equator and at high latitudes. Note the same balance of forces as in Figures 1.10 and 1.14. . .	48

1.19	The scaling of the equatorial and subtropical jet speeds in the non-linear shallow-water model, for cases with realistic forcing with variable values of forcing magnitude Q	50
1.20	Zonal-mean zonal flow of a suite of tests in the GCM Exo-FMS, showing how the equatorial and subtropical jet speeds and positions depend on instellation and rotation rate (Pierrehumbert and Hammond, 2018).	51
2.1	The linear responses to a forcing with magnitude $Q_0 = 1.0$ and $\alpha = 0.2$ unless specified. The positions of the various modes depends on the terms in the denominator of Equation 2.5.	59
2.2	The eigenvalues of the free modes of Equation 2.7, showing how eastward flow makes the eigenvalues more positive. This corresponds to an eastward shift in the response to forcing.	62
2.3	The meridional structure of the free Kelvin mode, with and without a background shear flow (Hammond and Pierrehumbert, 2018). The flow introduces a non-zero meridional velocity.	62
2.4	The meridional structure of the free Rossby mode, with and without a background shear flow. The shear affects the meridional structure, effectively changing the y coordinate (Hammond and Pierrehumbert, 2018) .	62
2.5	The time-mean height field from a simulation of a tidally locked planet in the model Exo-FMS, showing the typical eastward equatorial jet, shifted hot-spot, and night-side stationary Rossby waves.	65
2.6	The effect of a background shear flow $\bar{U}(y)$ on the forced solutions of Equation 2.9. The eastward flow Doppler-shifts the maximum of the response eastwards, corresponding to the hot-spot shift seen in GCM simulations (Tsai et al., 2014).	67
2.7	The forced response in zero background flow and a shear background flow, for dynamical damping $\alpha_{dyn} = 0$. These plots have the same form as those in Figure 2.6, showing that the dynamical damping is not critical.	69
2.8	Height fields of various responses to forcing, showing how the sum of the Doppler-shifted height field and the height field due to the zonal jet produces the distinctive pattern in Figures 2.5 and 2.6.	70
2.9	The effect of a background shear flow $\bar{U}(\phi)$ on the forced solutions of Equation 2.12, matching the form of the beta-plane solutions in Figure 2.6.	73
2.10	Spherical solutions with low and high forcing F_0 , showing how this affects the strength of the wave-1 component relative to the unchanged wave-0 jet component, affecting the longitudinal variation and day-night contrast.	77

2.11	Spherical solutions with low and high damping α , showing how this affects the strength of the wave-1 component and also the magnitude of the Doppler-shift of the wave components.	77
2.12	Spherical solutions with low and high rotation rate Ω , showing how this affects the magnitude of the wave-0 height perturbation $\bar{H}(\phi)$ balancing the imposed shear flow $\bar{U}(\phi)$	78
2.13	The temperature at the 500 mbar level from a suite of tests in the GCM Exo-FMS, with different rotation periods and instellations (Pierrehumbert and Hammond, 2018). All other parameters are the same as those in Figure 2.5.	79
2.14	The time-mean eddy temperature, velocity, and streamfunction fields on the half-surface pressure level of the GCM simulation shown in Figure 2.5.	81
2.15	Observed day-night contrast and hot-spot shift versus planetary equilibrium temperature showing an increased contrast and decreased shift at higher temperatures, from Komacek et al. (2017)	83
3.1	A schematic of the phase curve observed of the flux from a planet as it orbits its star. Position (1) is the secondary eclipse, (2) is the phase of the maximum thermal emission, and (3) is the primary eclipse.	88
3.2	The thermal phase curve observed at $4.5\text{ }\mu\text{m}$ by Demory et al. (2016) , showing an offset of the maximum flux from the secondary eclipse, corresponding to a hot-spot shift.	91
3.3	The temperature map reconstructed by Demory et al. (2016) from the phase curve in Figure 3.2, showing a a hot-spot shift of 41° , a day-side temperature of $(2700 \pm 270)\text{ K}$, and a night-side temperature of $(1380 \pm 400)\text{ K}$	91
3.4	The atmospheric parameter space, where the green region is predicted by the relations of Zhang and Showman (2017) to support both a significant hot-spot shift and day-night contrast. The black points show the GCM tests. The hot-spot shift and day-night contrast were calculated with advection speed 1000 m s^{-1} and mean temperature 2000 K . The two lines correspond to a hot-spot shift of 20° and a day-night contrast of 80%	96
3.5	10-day time-averaged maps of different temperature fields for Tests 1, 2, and 3. Each row is a different test. The first column shows the surface air temperature, which has the strongest day-night contrast as it is closely coupled to the surface temperature and stellar forcing. The second column is the temperature at the half-surface-pressure level, which can support both a large hot-spot shift and day-night contrast. The third column is the grey brightness temperature, which generally corresponds to a low atmospheric pressure, due to the high optical thickness.	102

3.6	10-day time-averaged temperatures at half-surface-pressure, for atmospheres with $\mu = 4.6 \text{ gmol}^{-1}$ and 15 gmol^{-1} $\text{H}_2 + \text{N}_2$ atmospheres with surface pressures of 3, 5, and 10 bar.	104
3.7	The temperature at the half-surface-pressure level for Tests 10, 11, and 12, with $\mu = 4.6 \text{ gmol}^{-1}$, surface pressure 5 bar and optical thicknesses of 2.0, 4.0, and 8.0.	105
3.8	The vertical structure of Test 4, and the hot-spot shift and day-night contrast of Tests 1, 2, and 4. The temperature profiles tend to follow the dry adiabat at high pressures on the day-side, but can become isothermal or inverted on the night-side. The lower atmospheres have a larger day-night contrast, and the upper atmospheres have a larger hot-spot shift – hence the focus on the middle atmosphere to match the observed phase curve, with both of these features.	107
3.9	Thermal phase curves calculated at different radiating levels in Test 4. Moving the radiating level to lower pressures has a similar effect to decreasing the mean molecular weight, as shown in Figures 3.12 and 3.13, producing a degeneracy in interpreting the observed phase curve. The black point shows the maximum (day-side) observed flux, and the black line shows the minimum (night-side) observed flux.	109
3.10	Phase curves calculated using the emission from the half-surface-pressure level of the 4.6 gmol^{-1} $\text{H}_2 + \text{N}_2$ atmospheres with surface pressures of 3, 5, and 10 bar, corresponding to the temperature maps in Figure 3.6.	112
3.11	Phase curves calculated using the emission from the half-surface-pressure level of the 5 bar 4.6 gmol^{-1} $\text{H}_2 + \text{N}_2$ atmospheres with optical thicknesses of 2.0, 4.0, and 8.0, corresponding to the temperature maps in Figure 3.7.	113
3.12	Simulated $4.5 \mu\text{m}$ phase curves calculated from the brightness temperature of the grey-gas OLR. The red curve is the 10 bar H_2 atmosphere, which has such efficient heat transport that it has a large peak offset and very small amplitude. The blue curve is the 10 bar N_2 atmosphere, with very weak heat transport so a large amplitude and peak offset. The green curve is the 5 bar $\text{H}_2 + \text{N}_2$ atmosphere, with a significant offset and amplitude. The offset and amplitude are not as large as the Demory et al. (2016) measurements, shown by the black point and line (with their errors shown by the bars and the shaded area).	113

3.13	Simulated phase curves for the emission from a radiating level at half-surface-pressure. The amplitude and offset are larger than the phase curves of the OLR. The offset and amplitude are not as large as the Demory et al. (2016) measurements, but Figure 3.14 shows that the H ₂ +N ₂ atmosphere (green curve) could match the observations with the night-side cloud formation discussed in Section 3.5.1.	114
3.14	Simulated phase curves for different possible equilibrium surface partial pressures of SiO in the 4.6 g mol ⁻¹ , 5 bar H ₂ + N ₂ atmosphere, based on the range of temperatures on the day-side surface. The 300 mbar curve shows that clouds could form on the day-side at high enough surface partial pressures. The offset and amplitude of the 100 mbar case almost agrees with the ? measurements within error.	116
4.1	Absorption coefficient versus wavenumber for CO at 2500 K and 1 bar from the HITEMP database (Rothman et al., 2010). For the simulations in this chapter, the longwave radiation from the surface peaks at about 5000 cm ⁻¹ and the incoming stellar radiation peaks at about 10 000 cm ⁻¹ , so the longwave optical depth of the atmosphere is higher than the short-wave optical depth.	122
4.2	Global temperature maps of the simulations with 1% CO, at the pressure level corresponding to the maximum zonal-mean zonal velocity.	125
4.3	Zonal-mean zonal wind of the simulations with 1% CO.	126
4.4	Temperature profiles of the simulations with 1% CO.	126
4.5	Spectral radiance of the outgoing longwave radiation (OLR) of Tests 1 and 2.	128
4.6	Emission spectra of the day-side and night-side of Tests 1 and 2. The green, orange, and blue dashed lines show the wavelengths corresponding to the phase curves of the same colours in Figure 4.7.	129
4.7	Thermal phase curves of the simulations with 1% CO. The thick black line shows the phase curve observed by Demory et al. (2016) in the Spitzer 4.5 μm channel. The thick red line is the phase curve simulated from each test using the same 4.5 μm bandpass. The other coloured lines show phase curves calculated at the representative wavelengths plotted in the same colours in Figure 4.6.	131
4.8	Global temperature maps of tests 3 and 4 at the pressure level with the maximum zonal-mean zonal wind.	132
4.9	Zonal-mean zonal wind of tests 3 and 4.	133
4.10	Temperature profiles around the equators of tests 3 and 4.	133
4.11	Thermal OLR of tests 3 and 4.	134

4.12	Thermal emission spectra of tests 3 and 4.	134
4.13	Phase curves at different wavelengths and in the Spitzer bandpass of tests 3 and 4.	135
A.1	The old latitude-longitude grid and the new cubed-sphere grid used in Exo-FMS.	160
B.1	The basis functions used for the pseudo-spectral methods to solve the shallow-water equations on a beta-plane and on a sphere.	165

Introduction

Lava planets are rocky, very hot, and orbit so close to their host stars that they are expected to be tidally locked to them. This means that they always present the same side to the star, so have a permanent day-side and night-side. Tidally locked planets appear to be common, and tidally locked lava planets are particularly well suited to observations. This thesis investigates the question of what the global circulation is on these planets, and how it can be observed.

Why are tidally locked planets important? Their unusual situation could make them seem like oddities, unrelated to the majority of planets. On the contrary, Figure 0.1 shows that a large fraction of known exoplanets are expected to be tidally locked. It shows the stellar masses and semi-major axes for all exoplanets listed on the NASA Exoplanet Archive at the time of writing, with all the planets below the line expected to be tidally locked ([Pierrehumbert and Hammond, 2018](#)).

These planets are also generally more easily characterised due to their proximity to their host stars, giving larger signals for spectroscopy when they transit them. This tendency may have created a detection bias, where close-in exoplanets are more likely to be detected so it appears that a greater fraction are tidally locked than is actually the case. Even if this is true, it does not detract from the relevance of tidally locked planets – we can only study planets we know about.

This thesis addresses the current question of the nature of the global circulation

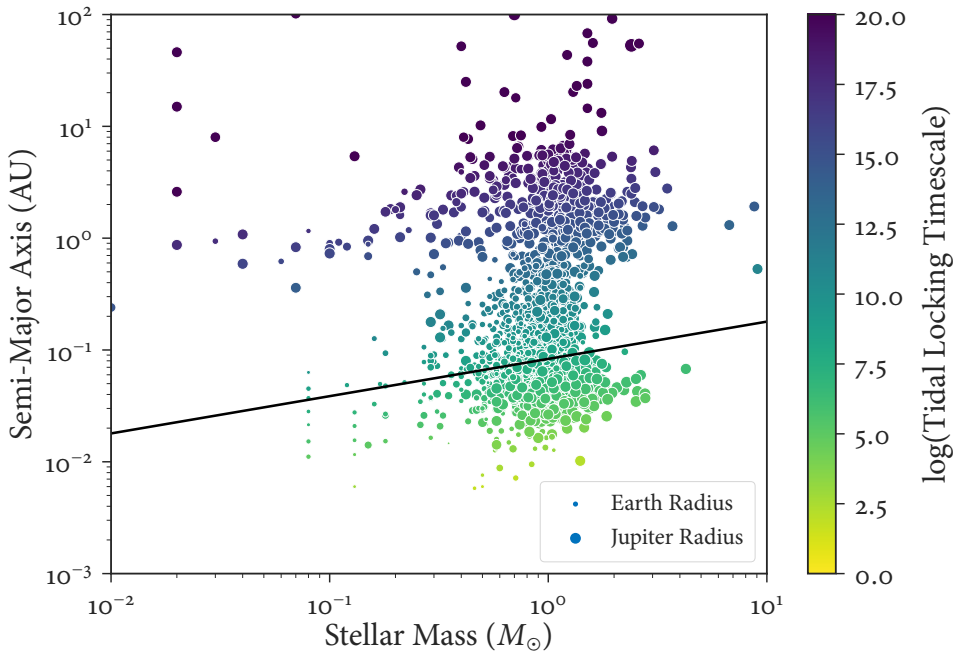


Figure 0.1: The population of known exoplanets plotted by semi-major axis and stellar mass. All the planets below the line have a timescale to reach a tidally locked state of less than 0.1 billion years, so are expected to be in this state.

on tidally locked planets in general, and lava planets in particular. In Chapter , “Review: The Atmospheres of Hot, Tidally Locked Planets”, I discuss the concept of a “lava planet” and review the literature of discovery, characterisation, and modelling of such planets.

In Chapter 1, “The Gierasch-Rossow-Williams Mechanism on Tidally Locked Planets”, I propose a modified mechanism for the formation of the zonal flow on tidally locked planets. The mechanism considers the role of the meridional circulation in the angular momentum budget of the atmosphere, and predicts the number of jets in the atmosphere and their strength.

Chapter 2, “Wave-Mean Flow Interactions in a Linear Theory of Tidally Locked Atmospheres”, is based on [Hammond and Pierrehumbert \(2018\)](#). In it, I linearise the shallow-water model used in [Showman and Polvani \(2011\)](#) about the equatorial jet

discussed in Chapter 1, and show how the response to stationary forcing explains the formation of the global circulation and hot-spot shift in GCM simulations.

Chapter 3, “Linking the Climate and Thermal Phase Curve of 55 Cancri e” is based on [Hammond and Pierrehumbert \(2017\)](#). It compare simulations of the atmosphere of the tidally locked planet 55 Cancri e to the observations of [Demory et al. \(2016\)](#), to constrain the properties of the atmosphere.

Chapter 4, “Realistic Modelling of Lava Planets” uses an improved model to investigate the climates simulated in Chapter 3 in more detail. It shows how the scaling relations and grey-gas approximation used in Chapter 3 are still a good description of more realistic simulations. I will show that the simulations with surface pressures of 1 bar do not have observable hot-spot shifts in their thermal emission at any wavelength, and conclude that the hot-spot shift observed by [Demory et al. \(2016\)](#) is evidence for a thick atmosphere.

In the Conclusion, I summarise my work on the global circulation of tidally locked planets, and its relevance for 55 Cancri e. I will conclude that the shallow-water models of the atmosphere of a tidally locked planet provide a prediction of its equilibrium flow and global temperature distribution. I will suggest that the phase curve of 55 Cancri e is consistent with an atmosphere of surface pressure significantly larger than than 10 bar and a mean molecular weight greater than that of H₂, with intermediate opacity in the Spitzer 4.5 μm bandpass. I will conclude that the global circulation of tidally locked planets is a rich geophysical fluid dynamical system, which we have the opportunity to understand in even more detail with upcoming observations of exoplanets.

Review: The Atmospheres of Hot, Tidally Locked Planets

In this chapter, I will review the studies and ideas that this thesis is based on. I will discuss the discovery and characterisation of exoplanets, focusing on the measurements relevant to their atmospheric composition and dynamics. Next, I will discuss tidally locked planets, both how they form and what atmospheric dynamics could take place on them. Finally, I will review the previous work on lava planets, and 55 Cancri e in particular, which motivated much of the work in this thesis.

Exoplanets

Exoplanets are planets orbiting stars other than our Sun. As far as we know, there is nothing fundamental to distinguish the planets in our Solar System from those elsewhere, so it is possible that this specific nomenclature may eventually disappear. I will use the word “exoplanet” when discussing specific planets or issues related to their distance, and “planet” in a more general or idealised context (such as the first sentence of this paragraph).

There is no better way to date a piece of writing on exoplanets than by announcing how many have been discovered, so I will just note that we know of several thousand and anticipate many more to come. The number of exoplanets which are favourable for detailed observations is still quite small, and we can observe atmospheric details

for perhaps only a few dozen planets. In fact, while the title of this thesis suggests it looks at “lava planets”, there is really only one that is currently observable – 55 Cancri e. Despite this, I hope to draw general conclusions about the circulation of many types of planet, and contribute to an understanding of tidally locked planets and lava planets for future observations.

Figure 0.2 shows all the exoplanets from the NASA Exoplanet Archive (exoplanetarchive.ipac.caltech.edu) for which radii and orbital periods were available at the time of writing. The population can firstly be divided approximately in two, with rocky planets below $R = 3R_E$, and gaseous planets above $R = 3R_E$. The planets in the lower left-hand corner are “lava planets”, which are in short-period orbits close to their star, and are very hot as a result. The other rocky planets to their left are more like Earth, Mars, or Venus. Above these, in the centre of the plot, we have the “Super-Earths”, rocky planets with radii around $2R_E$, and the “Mini-Neptunes”, of larger size and expected to be gaseous rather than rocky. The exact divide between these populations is not clear (or, for that matter, expected to be exact). At the top of the plot, we have the Jupiter-sized gas giants. On the left are the short-period “Hot Jupiters”, which are generally well suited for characterisation via transit observations. On the right are the cooler gas giants, which are more suited for detection by radial velocity or direct imaging techniques.

Discovering Exoplanets

Most exoplanets discovered to date have been found using either a “radial velocity” method or a “transit” method. In the first method, the motion of a star around its common center of mass with a planet orbiting it is detected by measuring the Doppler-shift of emission lines of the star. The magnitude and period of this motion gives the period of the planet’s orbit, and a limit on its mass.

In the second method, a planet passing across the line of sight from an observer

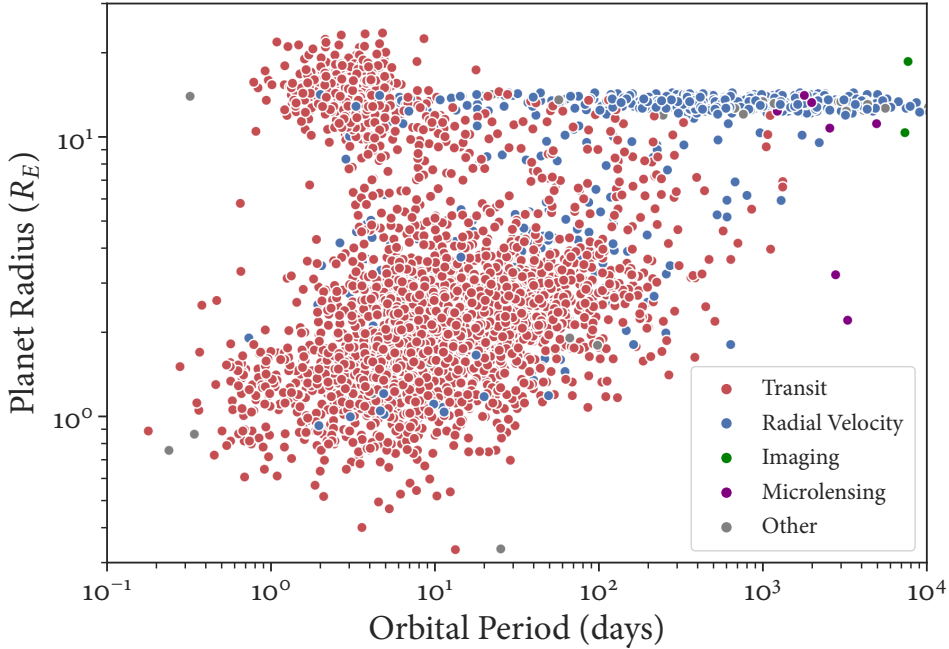


Figure 0.2: The population of known exoplanets plotted by planetary radius and orbital period. The planets are labelled by the method used to discover them.

to the star produces a dip in the light seen by the observer. A periodic dip gives the period of the planet, and the size of the dip gives its radius. So, if a planet can be measured with both methods the observer retrieves its period, mass, radius, density, semi-major axis, and equilibrium temperature.

Figure 0.2 shows how different discovery methods apply to different types of planet. The red dots show planets discovered by the transit method, which are currently the most common due to the success of the Kepler mission to detect transits. These planets are clustered to the left of the plot, as transits are more likely to be observed for close-in planets. This is because they are more likely to occur geometrically, and also produce a greater signal (a greater reduction in the flux from the star), the closer they orbit the star. The blue dots show planets detected by the radial velocity method, which applies mostly to larger gas giants, as the signals produced

by smaller planets are currently difficult to detect.

The planets shown in green have been detected by direct imaging, by blocking the light from their host star with a coronagraph and observing the planet directly. This is currently only possible for young, large, self-luminous planets orbiting far from their star, so these planets are found to the top right of the plot.

Characterising Exoplanets

The atmospheres of exoplanets can be characterised through transmission and emission spectroscopy. In transmission spectroscopy, light from the host star passes through the atmosphere of the exoplanet before it reaches the observer, and the spectrum is measured. An alternative (but equivalent) view is that the planet appears to have a different radius as it transits its star at different wavelengths – at a wavelength the atmosphere is more opaque to, the planet appears larger – so the absorption spectrum of the gases in the atmosphere can be retrieved.

In emission spectroscopy, the spectrum of the light emitted thermally by the planet and its atmosphere is measured. Hotter planets emit more light in this way, so are better suited to this method. [Stevenson et al. \(2014\)](#) used the thermal emission spectrum of a Hot Jupiter at different phases of its orbit to reconstruct its thermal structure.

Atmospheric Observations

It is possible to measure the bulk wind speed of the atmosphere of an exoplanet via the Doppler-shift of absorption lines in its transmission spectrum ([Louden and Wheatley, 2015; Brogi et al., 2016](#))

Phase curves are a major source of observations of exoplanet atmospheres, which I will discuss in more detail later in this chapter.

Tidally Locked Planets

An asynchronously rotating planet like the Earth has a different rotation period (1 day) to its orbital period (1 year). A synchronously rotating planet, commonly known as tidally locked, has the same rotation period as its orbital period. This means that it always presents the same face to its host star, having a permanent day-side and a permanent night-side.

Previously, I showed that many of the exoplanets discovered so far are expected to be tidally locked. There is some observational bias towards the discovery of planets orbiting close to their host stars as they produce greater observational effects in general. I will show next that such close-in planets are also more likely to be tidally locked, so there is an observational bias towards their detection. Regardless of whether the actual fraction of planets that are tidally locked is smaller than observations suggest, for the foreseeable future they will be some of our best sources of observations of exoplanets (REFS). It is therefore vital to connect these observations with theoretical work, especially as there are no examples of tidally locked planets in our Solar System for comparison.

Formation

All planets are affected by tidal stress due to gravity. At the centre of mass of the planet, the gravitational force exactly balances the centrifugal force. For the part of the planet closer to the star, gravity is stronger than the centrifugal force, and vice versa for the part of the planet further from the star. This produces a stress that elongates the planet along the axis between it and the star. If the planet is not tidally locked, the long axis of the resulting ellipse will rotate away from this axis, and the stress will deform the planet further. This continual deformation removes rotational kinetic energy from the planet, until it reaches a tidally locked state where

the long axis of the ellipsoid points towards the star permanently, so no more energy is dissipated (stable spin-orbit resonances are also possible, such as in the case of Mercury) (Pierrehumbert and Hammond, 2018).

The gravitational tidal stress acting on a planet is $\Sigma = 2GM_*/r^3$, where M_* is the mass of the star and r is the distance between the planet and the star. This means that planets orbiting close to high-mass stars are more likely to be tidally locked, and that the cubic dependence on r makes the orbital distance very important. Pierrehumbert and Hammond (2018) uses the results of Goldreich and Soter (1966) to estimate the time for a planet to become tidally locked:

$$t_{\text{lock}} = 3.01 \times 10^8 \frac{\rho \Omega_0 r^6}{M_\oplus^2} \frac{Q}{k_2} \quad (1)$$

Here, r is the mean orbital distance in AU, ρ is the mean density of the planet in units of Earth density, and Ω is the angular velocity of the planet in units of Earth angular velocity. Q corresponds to the effect of the dissipation of energy from tidal stresses, and k_2 is the Love number, which depends on the rigidity of the planet (Barnes, 2017). These last two parameters are not known for any particular planet, but Pierrehumbert and Hammond (2018) suggests that the estimated value of $Q/k_2 \approx 1000$ for Earth and Venus would be correct to within an order of magnitude for any rocky exoplanet.

This allows estimation of the time for different exoplanets to reach a tidally locked state, assuming they form with Earth's angular velocity. Pierrehumbert and Hammond (2018) uses this formula to estimate that the rocky Earth-sized planet Trappist-1d would become tidally locked in 4000 years, and that the super-Earth lava planet 55 Cancri e would take 6 years. These short timescales suggest that we can be confident that these planets are tidally locked. It is less clear whether planets with timescales of millions or billions of years will have reached this state, due to the approximations in

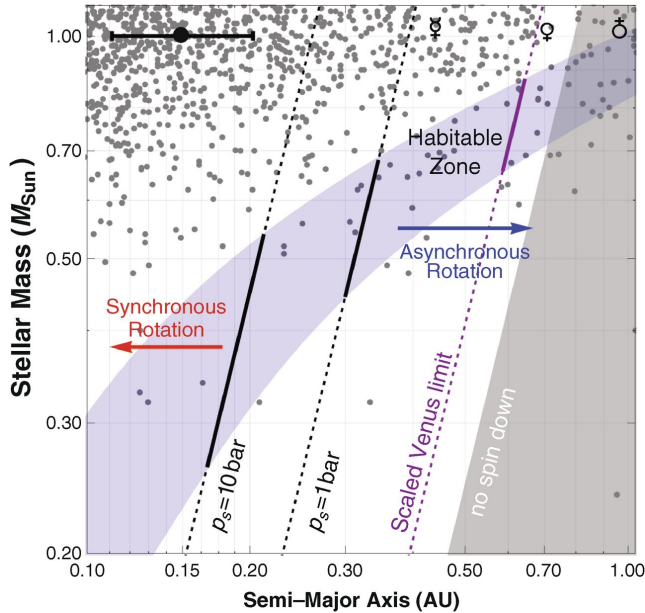


Figure 0.3: Figure from [Leconte et al. \(2015\)](#) showing the effect of atmospheres of 1 or 10 bar on the spin state of Earth-like planets, demonstrating that a thin atmosphere can prevent some planets from becoming tidally locked.

the calculation. The spin state of exoplanets can sometimes be measured indirectly with observations such as the thermal phase curves shown later.

Other factors may complicate the formation of a tidally locked state. [Leconte et al. \(2015\)](#) showed how thermal tides act against gravitational tides, and slow or prevent the progress towards tidal locking. Thermal tides are caused by the thermal inertia of the atmosphere creating an excess of mass in the atmosphere lagging behind the substellar point of an asynchronously rotating planet. The torque applied by the star's gravity on this excess is transferred to the planet, producing a torque opposing that of the gravitational tide acting directly on the planet. Figure 0.3 shows that this could inhibit tidal locking on Earth-mass planets, even those without thick atmospheres. Most of the planets considered in this thesis such as 55 Cancri e, or the variety of Hot Jupiters, will not be affected by this, but it is worth remembering that the previous simple estimate of a “tidal locking timescale” is not the whole story for many planets.

Lava Planets and 55 Cancri e

Chapters 3 and 4 focus on the atmospheric dynamics of lava planets. These are rocky planets that are hot enough to have some or all of their surface molten, producing a permanent “magma ocean”. Lava planets are favourable for atmospheric observations due to their high temperatures and proximity to their stars, giving large observational effects. This means they can be useful for understanding the global circulation of tidally locked terrestrial planets of all types, just as Hot Jupiters are useful for observing the circulation of tidally locked gaseous planets. The theory developed for lava planets can then be applied more generally to a range of planets, where the circulation may be important for other processes such as habitability.

[Miguel \(2018\)](#) [Ito et al. \(2015\)](#)

55 Cancri e is the best-characterised example of a lava planet. It is a Super-Earth with radius $1.947R_E$ and orbital period 0.737 days ([Crida et al., 2018](#)). It is expected to be tidally locked due to the short tidal locking timescale estimated above, and the sinusoidal shape of the thermal phase curve in [Demory et al. \(2016\)](#).

[Madhusudhan et al. \(2012\)](#) used interior models constrained by mass and radius measurements of 55 Cancri e to suggest that its interior is carbon-rich. More recently, [Dorn et al. \(2018\)](#) suggested that it is one of a class of similar Super-Earths with a lower interior density than the Earth, with no core.

[McArthur et al. \(2004\)](#) first detected the planet via the radial velocity method with an incorrect period of 2.808 days. [Dawson and Fabrycky \(2010\)](#) showed that this period was due to spurious aliasing caused by gaps in the observations, and corrected the period to 0.7365 days. [Demory et al. \(2011\)](#) and [Winn et al. \(2011b\)](#) detected transits of the planet, opening the possibility of atmospheric characterisation. [Tsiaras et al. \(2016\)](#) reported the detection of an atmosphere with the WFC3 instrument on the Hubble Space Telescope, which appeared to be hydrogen-rich with a possible

detection of HCN.

[Demory et al. \(2015\)](#) measured variable day-side thermal emission from 55 Cancri e over eight secondary eclipses, and suggested that this could be due to large-scale changes to the surface due to strong tidal interactions with the star.

A Thermal Phase Curve of 55 Cancri e

A “phase curve” is the radiation received from a planet as it orbits its star. They contain information about how the properties of the planet vary with position, as we observe different parts of the planet as it rotates. Phase curves of thermal wavelengths correspond to the radiating temperature of the planet or its atmosphere, so show features such as day-night temperature contrasts on tidally locked planets. Phase curves of optical wavelengths show the light from the host star reflected by the planet, so can show how the albedo of the planet varies with position due to features such as clouds ([Parmentier and Crossfield, 2017](#)).

As the magnitude of the phase curve at any point in the orbit (any “phase angle”) depends on the averaged flux received from the hemisphere facing the observer, the phase curve only contains information about the latitudinally averaged planetary features. Techniques such as “eclipse mapping” can retrieve longitudinal information, but require stronger signals from the planet ([Majeau et al., 2012](#)).

Phase curves are especially relevant to the atmospheric dynamics investigated in this thesis as the latitudinal variation of temperature on a planet can depend strongly on its global circulation. Figure 0.4 shows the thermal phase curve of 55 Cancri e measured by [Demory et al. \(2016\)](#) using the 4.5 μm channel of the Spitzer space telescope. The brightness temperature map reconstructed from this phase curve, and reproduced in Figure 0.5, shows a hot-spot shifted 41° east of the substellar point, which would be the hottest part without any atmospheric circulation. The phase curve also showed a night-side temperature of 1300 K, implying a significant warm-

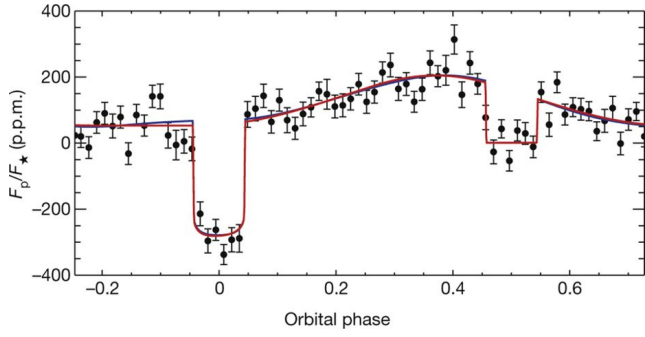


Figure 0.4: The thermal phase curve observed at $4.5 \mu\text{m}$ by Demory et al. (2016), showing an offset of the maximum flux from the secondary eclipse, corresponding to a hot-spot shift.

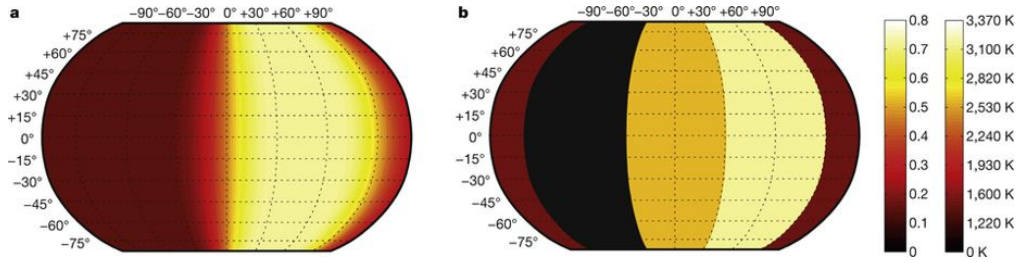


Figure 0.5: The temperature map reconstructed by Demory et al. (2016) from the phase curve in Figure 3.2, showing a hot-spot shift of 41° , a day-side temperature of $(2700 \pm 270) \text{ K}$, and a night-side temperature of $(1380 \pm 400) \text{ K}$.

ing of the night-side by atmospheric heat transport.

Angelo and Hu (2017) analysed this phase curve using a similar 1D energy balance model to Zhang and Showman (2017), which tuned parameters representing the planetary Bond albedo, atmospheric surface pressure, heat redistribution efficiency, and greenhouse effect, to match the observed phase curve. They estimated a surface pressure of 1.4 bar and a heat redistribution (ratio of radiative to advective timescales) of 1.47. Dragomir et al. (2012) measured an optical phase curve of the planet using the MOST space telescope and set an upper limit of 0.6 on its geometric albedo. The thermal phase curves of 55 Cancri e and other tidally locked planets motivated the work in this thesis to understand the atmospheric dynamics of tidally locked planets, and to simulate their observable consequences.

Atmospheric Dynamics

This thesis is concerned with understanding the atmospheric dynamics of tidally locked planets, and applying this understanding to the thermal phase curve of 55 Cancri e. In this section, I will discuss the current state of modelling the dynamics of exoplanet atmospheres and of the theory of their global circulation.

Numerical Models of Atmospheres

A General Circulation Model (GCM) is a three-dimensional fluid dynamical model of either or both of the atmosphere and ocean of a planet. Initially confined to modelling the atmosphere of Earth, they have been successfully used to model and match observations of other planets in the Solar System. They have also been used to simulate a wide variety of exoplanet atmospheres, and are now used to match and interpret observations of these planets.

GCMs typically consist of a dynamical core coupled to some representation of physical forcing such as radiative transfer or convective adjustment. The physics modelled in a GCM can range from very simple parameterisations capturing key processes (Held and Suarez, 1994) to highly detailed models of interacting clouds, radiative transfer, or other small-scale processes (Lines et al., 2018; Drummond et al., 2018)

The GCM used in this thesis is Exo-FMS (Ding and Pierrehumbert, 2016; Pierrehumbert and Ding, 2016; Hammond and Pierrehumbert, 2017, 2018). It is based on the GFDL Flexible Modelling System (gfdl.noaa.gov/fms/) and the associated cubed-sphere dynamical core (gfdl.noaa.gov/cubed-sphere-quickstart/). It has a modular structure, allowing for different physical modules to be swapped for each other – the relevant modules are discussed in more detail in each chapter. Appendix A outlines the overall structure of the model.

GCMs have perhaps been applied most successfully to modelling the atmospheres of Hot Jupiters, producing simulated observations that often match real observations well (Showman and Guillot, 2002; Mayne et al., 2014; Parmentier et al., 2016; Amundsen et al., 2016; Mayne et al., 2017). Terrestrial planets have also been investigated to suggest what circulation regimes or stable climate states could exist (Merlis and Schneider, 2010; Boutle et al., 2017; Noda et al., 2017). Other classes of exoplanet such as super-Earths or sub-Neptunes have been modelled in varying levels of detail (Heng and Showman, 2015; Carone et al., 2015; Charnay et al., 2015).

Superrotation

Superrotation refers to the situation where the atmosphere has more angular momentum than the solid planet below it. There are different ways of defining this mathematically – in this thesis, I will use the definition of Read (1986); Read and Lebonnois (2018). This defines superrotation as a positive “superrotation index”, corresponding to an excess of atmospheric angular momentum over solid-body rotation at the equator. The local superrotation index is:

$$s = \frac{m}{\Omega a^2} - 1 \quad (2)$$

where the specific angular momentum m is:

$$m = a \cos \phi (\Omega a \cos \phi + u), \quad (3)$$

An atmosphere with an “ideal” meridional circulation would homogenise the angular momentum of the equatorial surface in its upper branch, giving a superrotation index of 0 everywhere there. In reality, the meridional circulation is not perfect (see the limited extent of the Earth’s Hadley circulation) and the superrotation index will be negative in most places. A process transporting angular momentum towards

the equator, such as the stationary waves on tidally locked planets (Showman and Polvani, 2011), can produce an excess of angular momentum there, giving a positive local superrotation index.

The global superrotation index is a mass-weighted integral of the local quantity:

$$S_m = \frac{\iiint \rho m dV}{\iiint \rho \Omega a^2 \cos^2 \phi dV} - 1. \quad (4)$$

Hide's Theorem requires that the local s and global S_m cannot be positive anywhere without these up-gradient angular momentum fluxes (Hide, 1969). Superrotation is found in the atmosphere of Earth and other planets in the Solar System such as Venus and Titan (Laraia and Schneider, 2015; Read and Lebonnois, 2018; Sugimoto et al., 2019).

Dynamics of Tidally Locked Atmospheres

Tidally locked planets are forced in a very different way to the known planets in the Solar System. The main source of atmospheric dynamics is the strong contrast in heating and cooling between the day-side and the night-side. This would be expected to drive an isotropic flow from the substellar point on the day-side (Weinbaum, 1935), which is sometimes the case in simulations of very slowly rotating or strongly damped atmospheres (Pierrehumbert and Hammond, 2018; Arcangeli et al., 2019). More commonly, the day-night forcing excites stationary waves that pump eastward momentum towards the equator, producing a superrotating jet that transports heat from the day-side to the night-side (Showman and Polvani, 2011). I will investigate the formation of the zonal flow in Chapter 1.

This equatorial superrotation was predicted by GCM simulations of terrestrial and gaseous tidally locked planets before its effects were observed (Joshi et al., 1997; ?). The strongest thermal emission from many Hot Jupiters was shown to be eastward

of the substellar point, suggesting eastward transport of energy by the superrotating flow. This was considered to be due to pure advection of heat by the flow, until [Tsai et al. \(2014\)](#) showed that the eastward jet could shift the stationary waves excited by the day-night forcing eastwards. This matches the results of GCM simulations more closely than heat transport by advection. Figure 0.6 shows a typical global temperature map from a simulation of a tidally locked planet, with the hot-spot shifted east of the substellar point. I will discuss this hot-spot shift in more detail in Chapter 2, and will show how a latitudinally sheared equatorial jet produces the global circulation pattern and hot-spot shift.

The formation of the superrotating jet in models and reality is still not fully understood. Studies such as [Kataria et al. \(2015\)](#) compare real observations to the results of GCM simulations of tidally locked Hot Jupiters, confident that the dynamics formed by the GCM are reasonably accurate. However, [Thrastarson and Cho \(2010\)](#) suggested that simulations of the atmospheres of Hot Jupiters depended strongly on initial conditions, and that the equilibrium states could not be relied upon to be realistic. [Liu and Showman \(2013\)](#) suggested that this was not the case if a bottom drag was applied to the atmosphere, justified as some interaction with a deeper layer not represented in the GCM. Their simulations reached the same equilibrium state regardless of the initial conditions. However, [Cho et al. \(2015\)](#) responded to this by demonstrating that the short timescale of this drag removed the variability otherwise present in the simulations, and concluded that while a bottom drag may remove sensitivity it may also remove physically important processes from the atmosphere. More recent simulations such as [Mendonça et al. \(2016\)](#) have successfully modelled Hot Jupiters without applying a bottom drag, suggesting that this earlier problems were model-dependent. The question of the sensitivity to initial conditions and role of bottom drag is still not fully resolved, which motivates the investigation of the basic dynamics forming this global circulation later in Chapter 1, particularly its de-

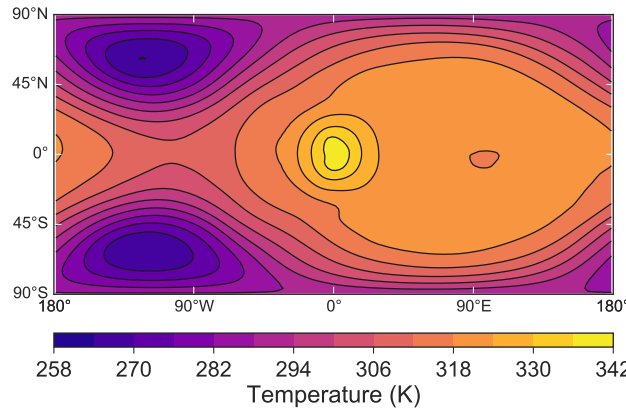


Figure o.6: The global temperature field at 500 mbar of a simulation of a tidally locked Earth-sized planet with a 10 day rotation period and a 1 bar N₂ atmosphere, showing an eastward shifted hot-spot and night-side cold stationary waves, reproduced from [Pierrehumbert and Hammond \(2018\)](#).

pendence on atmospheric drag.

[Polichtchouk et al. \(2014\)](#) further cast doubt on the results of other GCM simulations by showing significant differences between the results of different GCMs modelling the same exoplanets.

With more detailed simulations and observations, and a better theoretical understanding, it is becoming possible to predict and test scaling relations of atmospheric circulation against observations of many different planets in a large parameter space – something that was impossible when geophysical fluid dynamics was restricted to the Solar System. [Komacek and Showman \(2016\)](#) [Komacek et al. \(2017\)](#) [Zhang and Showman \(2017\)](#) applied a 1D model balancing the advection of heat against radiation and compared it to observations. In Chapters 3 and 4, I will compare simulations of the atmospheric dynamics of the tidally locked planet 55 Cancri to observations of its temperature distribution.

CHAPTER 1

The Gierasch-Rossow-Williams Mechanism on Tidally Locked Planets

Tidally locked planets are heated by their star only on their day-side, and cool freely on their night-side. This heating gradient drives the dominant dynamical feature of their atmosphere – a flow from day-side to night-side. The nature of this flow depends on the properties of the planet, and often takes the form of an eastward jet centred on the equator. The strength and forms of this jet controls the temperature distribution of the planet, affecting observations, global climate, and habitability. [Showman and Polvani \(2011\)](#) explained the formation of this equatorial flow using the linear shallow-water model of [Matsuno \(1966\)](#).

However, this shallow-water model is not always consistent with the zonal flow produced by many GCM simulations. The shallow-water model requires easterly flow at high latitudes, which is the only source of angular momentum for the equatorial jet in the model. On the other hand, GCMs often show eastward flow at all latitudes, suggesting another source of angular momentum.

I will show how combining the shallow-water model with the Gierasch-Rossow-Williams (GRW) mechanism gives a coherent description of the zonal flow in the GCM simulations. The GRW mechanism combines transport of angular momentum

by a mean meridional circulation with equatorward transport by eddies, producing a superrotating flow at the equator. This means that a superrotating equatorial jet requires subrotating flow at higher latitudes, but this subrotating flow can still be westerly – unlike the model in [Showman and Polvani \(2011\)](#), which requires easterly flow at high latitudes. This mechanism is therefore consistent with the westerly flow seen at all latitudes in some GCM simulations.

The mean meridional circulation required for this mechanism is more complex on tidally locked planets, as their equator-to-pole-forcing gradient varies with longitude. However, I will show how to lowest order only the zonal mean of the forcing matters for the mean meridional circulation, so its effect can be easily approximated on a tidally locked planet. I will discuss the balance of sources of momentum transport giving zonal acceleration in GCM simulations and in a non-linear shallow-water model, and show that the equilibrium zonal flow is governed by different balances at the equator and at high latitudes. Finally, I will use this mechanism to predict scaling relations for jet positions and speeds in both models, and will test these predictions against a suite of tests in the models.

I will conclude that the formation of zonal flow on a tidally locked planet can be explained by the GRW mechanism, with equatorward momentum transport provided by the process explained in [Showman and Polvani \(2011\)](#). I will show that the balance of acceleration due to different momentum transports in this mechanism is the same in a linear shallow-water model, a non-linear shallow-water model, and a GCM. In the following chapter, I will use this understanding of the formation of zonal flow to describe its effect on the global circulation and temperature distribution.

1.1 Linear Shallow-Water Model of a Tidally Locked Planetary Atmosphere

In this section, I will review the linear shallow-water model used by [Matsuno](#)

(1966) to investigate free and forced equatorial waves in the Earth's tropics. I will show how [Showman and Polvani \(2011\)](#) used this model to explain the formation of equatorial superrotation in tidally locked planetary atmospheres, then I will show how the linear model is not entirely consistent with the flow formed in GCM simulations.

1.1.1 Linear Shallow-Water Equations

[Matsuno \(1966\)](#) constructs a single-layer shallow-water model representing a single layer of fluid with a free upper surface on an equatorial beta-plane ($f = \beta y$), with the equations:

$$\begin{aligned} \frac{\partial u}{\partial t} - \beta y v + \frac{\partial h}{\partial x} &= 0, \\ \frac{\partial v}{\partial t} + \beta y u + \frac{\partial h}{\partial y} &= 0, \\ \frac{\partial h}{\partial t} + c^2 \left(\frac{\partial u}{\partial x} + \frac{\partial v}{\partial y} \right) &= Q(x, y), \end{aligned} \quad (1.1)$$

where h is the height and $c = \sqrt{gH}$ is the gravity wave speed. Appendix B describes the pseudo-spectral method used to solve these equations. Non-dimensionalizing with time scale $\sqrt{1/c\beta}$ and length scale $\sqrt{c/\beta}$ (the equatorial Rossby radius of deformation L_R), and assuming all quantities have the form $f(y)e^{i(kx-\omega t)}$, the equations describing free perturbations are:

$$\begin{aligned} -i\omega u - yv + ik_x h &= 0, \\ -i\omega v + yu + \frac{\partial h}{\partial y} &= 0, \\ -i\omega h + ik_u + \frac{\partial v}{\partial y} &= 0. \end{aligned} \quad (1.2)$$

[Matsuno \(1966\)](#) solves these equations analytically to find the dispersion relation of the free modes, and discusses the latitudinal structure of each mode. I will focus on the response to stationary forcing of this system so there will be no free

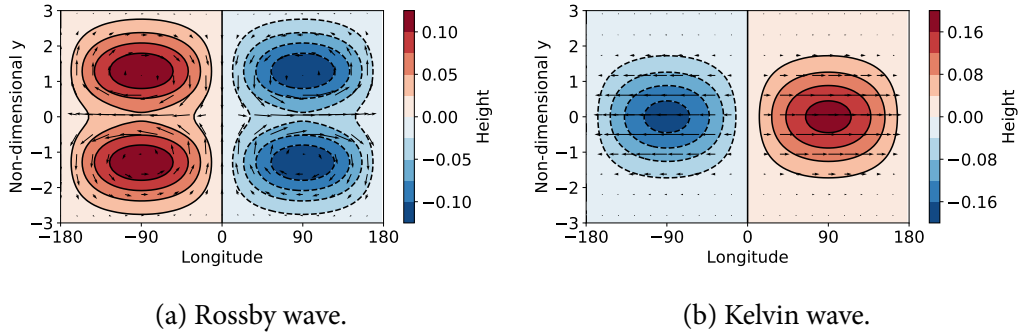


Figure 1.1: The height and velocity fields of the lowest order free modes of a shallow-water system on an equatorial beta-plane.

modes present, but understanding their behaviour is important as their structures and eigenfrequencies will determine their magnitudes and positions in the forced response.

The forcing on a tidally locked planet (and in the example used by Matsuno (1966)) is stationary and symmetric about the equator, so it will preferentially excite the lowest-order symmetric modes – the Rossby and Kelvin modes. It also has a fixed zonal wavenumber $k_x = 1$, so excites these modes with this wavenumber. Figure 1.1a shows the free Rossby mode with wavenumber 1. It has a positive eigenvalue, so travels westward as a free mode (as $c = \omega k_x$). Figure 1.1b shows the free Kelvin mode with wavenumber 0. This is a special solution of the equations with zero meridional velocity. It has a negative eigenvalue so travels eastward as a free wave.

1.1.2 Linear Response to Forcing

Showman and Polvani (2011) uses this linear shallow-water model to represent the atmosphere of a tidally locked planet. A tidally locked planet is constantly heated on its day-side and cooled on its night-side, giving a stationary forcing very similar to that used as an example by Matsuno (1966). This forcing acts on the h field, giving the equations:

$$\begin{aligned}\alpha_{dyn}u - \beta yv + \frac{\partial h}{\partial x} &= 0, \\ \alpha_{dyn}v + \beta yu + \frac{\partial h}{\partial y} &= 0, \\ \alpha_{rad}h + c^2\left(\frac{\partial u}{\partial x} + \frac{\partial v}{\partial y}\right) &= Q(x, y),\end{aligned}\tag{1.3}$$

with boundary conditions

$$u, v, h \rightarrow 0 \quad \text{for } y \rightarrow \pm\infty.\tag{1.4}$$

[Matsuno \(1966\)](#) shows how the response of Equation 1.3 to a forcing $Q(x, y) = Q_0 \sin(x) e^{-y^2/2}$ and uniform damping $\alpha_{rad} = \alpha_{dyn} = \alpha$ can be found analytically as a sum of the free modes of the system. The forced response $\chi = (u, v, h)$ is a sum of the free modes $\xi_m = (u_m, v_m, h_m)$, weighted by coefficients a_m

$$\chi = \sum a_m \xi_m,\tag{1.5}$$

where the coefficients are given by

$$a_m = \frac{1}{\alpha - i\omega_m} b_m,\tag{1.6}$$

where ω_m is the eigenvalue of the mode m , and

$$b_m = \left[\int \bar{\xi}_m(y) \sigma(y) dy \right] / \left[\int |\xi_m(y)|^2 dy \right].\tag{1.7}$$

Figure 1.2 shows the response to the forcing $Q(x, y) = Q_0 \sin(x) e^{-y^2/2}$, where all of the coefficients a_m are zero apart from those for the Kelvin wave and the $n = 1$ Rossby wave. The Rossby wave appears west of the substellar point due to its positive eigenvalue ω_m , and the Kelvin wave appears east of the substellar point due to its negative eigenvalue.

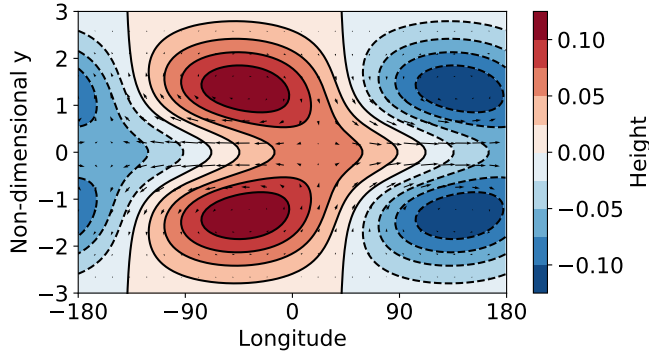


Figure 1.2: Response of Equation 1.3 to forcing $Q(x, y) = Q_0 \sin(x) e^{-y^2/2}$, showing the maximum of the Rossby wave west of the maximum of the forcing (i.e. the sub-stellar point) and the maximum of the Kelvin wave east of this point.

1.1.3 Equatorial Acceleration

The phase shift between the Rossby and Kelvin waves in the response to forcing produces a momentum transport and a zonal acceleration (Showman and Polvani, 2011; Tsai et al., 2014). Zonally averaging the zonal momentum equation in Equation 2.8 gives the zonal acceleration profile in this beta-plane shallow-water model (Thuburn and Lagneau, 1999):

$$\frac{\partial \bar{u}}{\partial t} = \underbrace{\bar{v}^* \left[f - \frac{\partial \bar{u}}{\partial y} \right]}_{I} - \underbrace{\frac{1}{\bar{h}} \frac{\partial}{\partial y} \left[(\bar{h}v)' u' \right]}_{II} + \underbrace{\frac{1}{\bar{h}} \bar{u}' Q'}_{III} - \underbrace{\frac{\bar{u}^*}{\tau_{\text{drag}}} - \frac{1}{\bar{h}} \frac{\partial (\bar{h}' u')}{\partial t}}_{IV}, \quad (1.8)$$

However, the linear shallow-water model constructed by Matsuno (1966) does not accelerate at the equator. Figure 1.3 plots the terms in Equation 1.11 for the response to forcing in Figure 1.2. It shows that the convergence of eastward momentum at the equator due to horizontal eddy fluxes (term II) is exactly cancelled by the removal of eastward momentum from the equator due to vertical momentum transport (term III).

This can be explained by rewriting Equation 1.11 in terms of the relative vorticity $\tilde{\zeta} = (v_x - u_y) \hat{k}$:

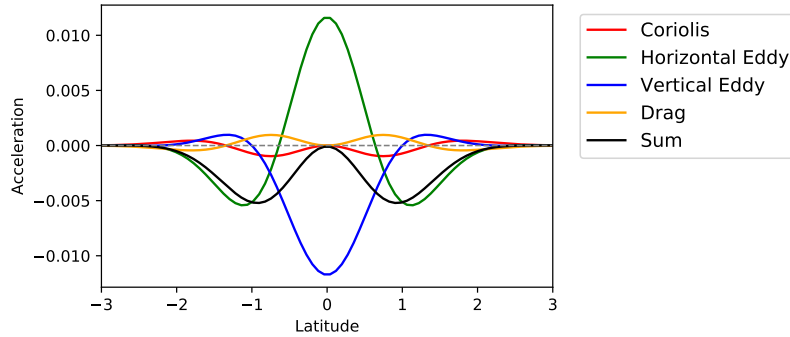


Figure 1.3: Terms in the zonal-mean zonal momentum equation (Equation 1.11) without the correction R to the momentum.

$$\frac{\partial \bar{u}}{\partial t} = \bar{v}'\bar{\zeta}' + \bar{v}(f + \bar{\zeta}) - \frac{\bar{u}}{\tau_{\text{drag}}}, \quad (1.9)$$

[Showman and Polvani \(2011\)](#) explained that for forcing that is symmetric about the equator, the solutions are symmetric about the equator in u but antisymmetric in v and therefore also in ζ . So, v and ζ are zero at the equator, and the first two terms in Equation 1.12 are zero.

[Showman and Polvani \(2010\)](#) showed that there is a missing term corresponding to the mean vertical momentum transport, and introduced a correction for this term. This correction is necessary to properly represent the effect of advection between the active upper layer and quiescent lower layer, and is the same as the correction used by [Shell and Held \(2004\)](#) to model the formation of superrotation on Earth. [Showman and Polvani \(2010\)](#) explain:

“Air moving out of the upper layer ($Q < 0$) does not locally affect the upper layer’s specific angular momentum or wind speed, hence $R = 0$ for that case. But air transported into the upper layer carries lower-layer momentum with it and thus alters the local specific angular momentum and zonal wind in the upper layer.”

[Shell and Held \(2004\)](#) impose conservation of momentum in the exchange be-

tween the stationary lower layer and the active upper layer, which corresponds to the following correction to the vertical momentum transport:

$$R(\lambda, \phi, t) = \begin{cases} -\frac{Qv}{h}, & Q > 0 \\ 0, & Q < 0 \end{cases} \quad (1.10)$$

In the axisymmetric case of [Shell and Held \(2004\)](#), the air is rising at the equator and falling at the poles, which causes a feedback between the equatorial flow speed and the forcing. In [Showman and Polvani \(2010\)](#), the air is rising at the substellar point and falling at the antistellar point, but the form of R is the same.

Figure 1.2 shows why this term produces a net westerly acceleration at the equator. On the day-side where $Q > 0$, the equatorial winds are mostly easterly, so R is non-zero and positive, giving a westerly acceleration. On the night-side, $Q < 0$ so there is no effect from R . Therefore, despite the periodicity of the wind field, the asymmetry in the effect of R means that there is a net westerly acceleration applied to the equator. Including this correction, the zonal-mean momentum equation becomes:

$$\frac{\partial \bar{u}}{\partial t} = \underbrace{\bar{v}^* \left[f - \frac{\partial \bar{u}}{\partial y} \right]}_{I} - \underbrace{\frac{1}{h} \frac{\partial}{\partial y} \left[\overline{(hv)' u'} \right]}_{II} + \underbrace{\left[\frac{1}{h} \overline{u' Q'} + \overline{R_u}^* \right]}_{III} - \underbrace{\frac{\bar{u}^*}{\tau_{\text{drag}}} - \frac{1}{h} \frac{\partial (\bar{h}' u')}{\partial t}}_{IV}, \quad (1.11)$$

and in vorticity form, it is:

$$\frac{\partial \bar{u}}{\partial t} = \overline{v' \zeta'} + \bar{v}(f + \bar{\zeta}) - \frac{\bar{u}}{\tau_{\text{drag}}} + \overline{R_u} \quad (1.12)$$

so that even at the equator with zero mean flow, when the first two terms are zero, there is a positive westerly acceleration. Figure 1.4 shows the acceleration terms and their sum when the R term is included, for the forced solution in Figure 1.2 (the same as Figure 2 in [Showman and Polvani \(2011\)](#)). As the effect of vertical transport at the equator is reduced, there is now a net eastward acceleration at the equator.

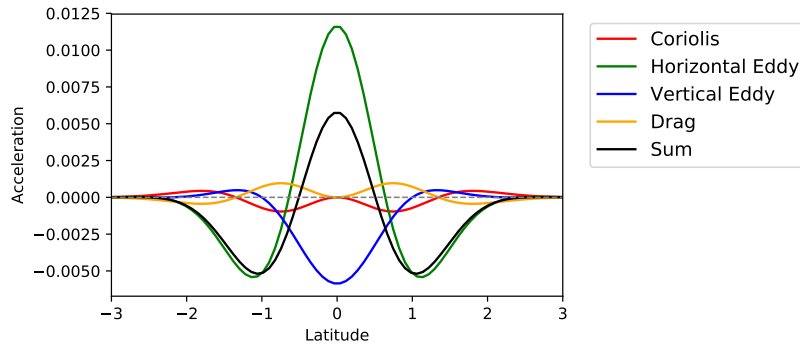


Figure 1.4: Terms in the zonal-mean zonal momentum equation (Equation 1.11) with the correction R to the momentum.

This acceleration profile explains the formation of eastward equatorial flow in the atmospheres of tidally locked planets. However, it is not consistent with GCM simulations with westerly flow at all latitudes at the level of the jet. In this chapter I will discuss how the meridional circulation, which was not considered by [Showman and Polvani \(2011\)](#), could resolve this difference.

1.1.4 Super- and Sub-Rotation

It is important to define the concept of “superrotation” precisely, to make the proposed effect of the meridional circulation clear. [Read and Lebonnois \(2018\)](#) defines superrotation using the “superrotation index”, which is a relative angular momentum excess compared to solid-body rotation at the equator ([Read, 1986](#)). The specific angular momentum m is:

$$m = a \cos \phi (\Omega a \cos \phi + u), \quad (1.13)$$

and the local superrotation index is:

$$s = \frac{m}{\Omega a^2} - 1 \quad (1.14)$$

This provides a measure of the local momentum excess provided by momentum fluxes in the atmosphere – generally, equatorward fluxes which produce a positive superrotation index. The global superrotation index is a mass-weighted integral of the local quantity:

$$S_m = \frac{\iiint \rho m dV}{\iiint \rho \Omega a^2 \cos^2 \phi dV} - 1. \quad (1.15)$$

[Read and Lebonnois \(2018\)](#) highlights that s and S_m cannot exceed zero without up-gradient fluxes of angular momentum, a condition referred to as Hide's Theorem ([Hide, 1969](#)). On a tidally locked planet, these are provided by the stationary horizontal eddy momentum fluxes discussed previously and shown in Figure 1.4.

The distinction between superrotating and subrotating flow, versus westerly and easterly flow, is vital to the conclusions of this chapter. The fluxes shown in Figure 1.4 operates on a background flow of zero. Therefore, any westerly flow at the equator requires easterly flow at high latitudes to conserve angular momentum. The GRW mechanism used in this chapter applies this system to a non-zero background flow, with a meridional circulation and westerly subtropical jet. Then, the equatorward momentum transport produces westerly superrotating flow at the equator – but, it does not necessarily need to be compensated by easterly flow as before. Instead, it must be compensated by more subrotating flow (lower s) at higher latitudes. This subrotating flow can still be westerly, leading to the westerly flow at all latitudes seen in some GCM simulations.

1.2 The Meridional Circulation on a Tidally Locked Planet

The meridional circulation of any atmosphere is driven by a difference in forcing between its equator and pole. On the Earth, it consists of multiple overturning cells which transport energy meridionally and produce zonal flows. On a tidally locked planet, it may be more complicated as the non-axisymmetric forcing means it varies with longitude. This meridional circulation has been measured by some studies of Hot Jupiters and sub-Neptunes, suggesting the presence of subtropical jets and inverse cells on day-side and night-side ([Charnay et al., 2015](#); [Showman et al., 2015](#); [Mendonça et al., 2018](#)). These were diagnostic studies, and did not consider the role of the meridional circulation on the global circulation, particularly its effect on the formation of zonal flow.

In this section, I will show that the linear shallow-water model of [Showman and Polvani \(2011\)](#) is not consistent with some aspects of the zonal flow produced in GCM simulations of tidally locked planets. The shallow-water model requires easterly flow at high latitudes if there is to be westerly equatorial superrotation, but some GCM simulations have westerly flow at all latitudes at the level of their jet.

I will introduce the Gierasch-Rossow-Williams (GRW) mechanism as a way to reconcile these differences. This mechanism combines the momentum transport of a meridional circulation with the equatorward momentum transport of the [Showman and Polvani \(2011\)](#) mechanism (it was originally used to explain the superrotation of the atmosphere of Venus). I will show that the zonal mean meridional circulation can be considered to only depend on the zonal mean of the forcing, avoiding the difficult question of its longitudinal variation.

The GRW mechanism then allows for westerly flow at all latitudes, as it pumps

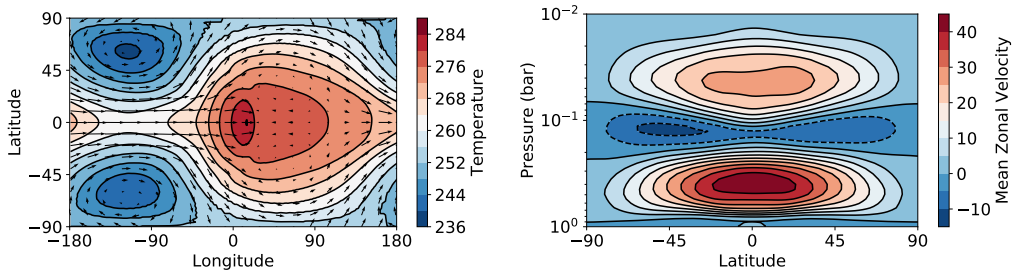
westerly momentum into the atmosphere from the surface and transports it to high latitudes. I will demonstrate this mechanism at work in a linear shallow-water model, a non-linear shallow-water model, and the GCM Exo-FMS. I will show that it requires subrotating (not superrotating) flow at high latitudes – but this subrotating flow can still be westerly.

1.2.1 Angular Momentum in the Shallow-Water Model

The linear shallow-water model from [Showman and Polvani \(2010\)](#), introduced in the previous section, is inconsistent with some aspects of GCM simulations of tidally locked planets. Firstly, it requires that there is easterly flow above a certain latitude, as the only way to accelerate westerly equatorial flow is to move the momentum from high latitudes to the equator. However, many GCM simulations have westerly zonal flow at all latitudes at the level of their jet ([Pierrehumbert and Hammond, 2018](#)).

Secondly, the linear model can only lose net angular momentum from the level of the jet, as the only exchange of momentum out of the layer is a net loss to the lower layer, via term III in Equation 1.11. Many GCM simulations of tidally locked planets have positive net angular momentum at the level of their jet (and in total in their atmosphere) so contradict the linear model ([Heng and Showman, 2015; Pierrehumbert and Hammond, 2018](#)). These differences indicate that the shallow-water model does not include a process that transports angular momentum from the lower layer to high latitudes at the level of the equatorial jet. In this section, I will use two simulations in the GCM Exo-FMS to show how a mean meridional circulation can supply this transport. Test 1 is a tidally locked planet with the parameters:

- Radius $R = R_E = 6.371 \times 10^6$ m
- Rotation rate $\Omega = \Omega_E/10 = 7.29 \times 10^{-6}$ s⁻¹



(a) Temperature and velocity fields at the half-surface pressure level.
(b) Zonal-mean zonal velocity, with the jet at the half-surface pressure level.

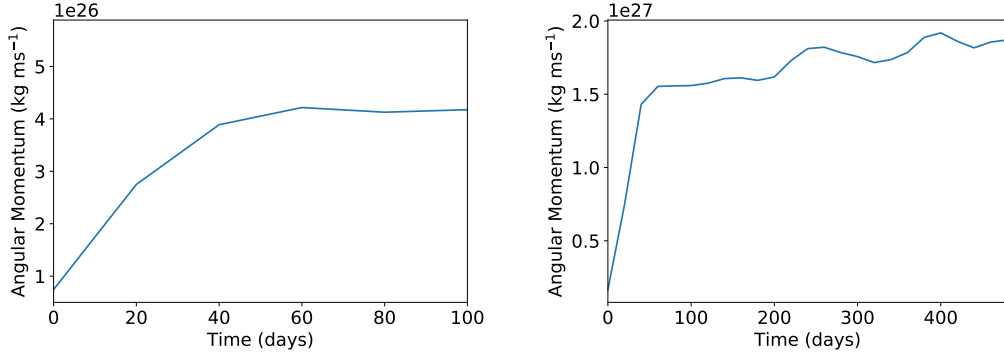
Figure 1.5: The global circulation of a typical tidally locked Earth-like planet, with prograde zonal flow at all latitudes at the level of maximum jet flow.

- Surface pressure $p_s = 1 \text{ bar}$
- Longwave optical thickness $\tau = 1$
- Instellation $F_* = 1000 \text{ W m}^{-2}$
- Pure N_2 atmosphere

Test 2 is a planet with axisymmetric forcing with exactly the same parameters. Its forcing has the same zonal mean as the tidally locked case, but is uniform in longitude rather than applied to the day-side only. [Norton \(2006\)](#) used two very similar tests to show the formation of superrotation by tropical heating on the Earth.

Figure 1.5a shows the time-mean temperature and wind fields at the half-surface pressure level of Test 1. I will show how the zonal flow produces this distinctive pattern with its “hot-spot shift” in Chapter 2. Figure 1.5b shows the zonal-mean zonal wind of Test 1. There is a superrotating equatorial jet as explained in [Showman and Polvani \(2011\)](#), but there is westerly flow at all latitudes at the pressure level of the core of this jet, which contradicts the shallow-water model.

Figure 1.6 shows the evolution of atmospheric angular momentum as the GCM spins up from rest. The left panel shows the angular momentum in the entire atmosphere, and the right panel shows the angular momentum at the pressure level of the jet. In both cases, the net angular momentum increases with time until it reaches a



(a) Evolution of global angular momentum. (b) Evolution of angular momentum in the jet layer.

Figure 1.6: The spin-up of angular momentum globally and at the pressure level of the jet, showing how both regions gain momentum over time then equilibrate.

positive equilibrium value, contradicting the linear shallow-water model which can only lose angular momentum from the jet layer. The linear shallow water model of [Showman and Polvani \(2011\)](#) can explain the formation of equatorial superrotation in this GCM simulation, but not the formation of the westerly flow at all latitudes.

1.2.2 The Gierasch Mechanism on a Tidally Locked Planet

In this section, I will introduce the GRW mechanism and show how it can be applied to a tidally locked planet. I will demonstrate that the zonal-mean meridional circulation – a vital part of the mechanism – can be approximated as only due to the zonal mean of the forcing, avoiding the complicated longitudinal variation of the meridional circulation.

Figure 1.7 shows the GRW mechanism ([Read and Lebonnois, 2018](#)) as applied to the atmosphere of a tidally locked planet. The solid lines show the mean meridional circulation, which transports air up from the equator and poleward in the jet layer. It accelerates in this upper branch to conserve angular momentum as it travels poleward, creating westerly subtropical jets. The equatorward lower branch accelerates westward for the same reason and is dragged by the surface. This produces a

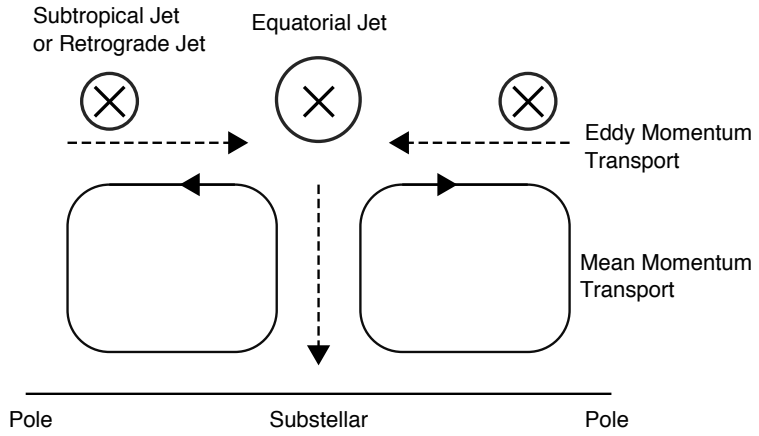


Figure 1.7: The Gierasch-Rossow-Williams (GRW) mechanism as applied to tidally locked planets. The solid line shows the mean momentum transport, which produces subtropical jets at high latitudes. The dashed lines show the horizontal and vertical eddy momentum transports, which accelerate and decelerate the equatorial superrotation respectively.

net eastward torque on the atmosphere, which is conveyed to the upper layer by the meridional circulation. This results in a net positive angular momentum in both the jet layer and in the whole atmosphere.

The dashed lines show the momentum transport terms due to the stationary wave response in a tidally locked planet ([Showman and Polvani, 2011](#)). These transport angular momentum equatorward in the jet layer, and downward at the equator. Later, I will show how they balance each other at the equator, and the transport from the mean meridional circulation at higher latitudes. This will explain how the number of zonal jets and their relative strength depends on the planetary parameters.

This provides an idealised picture of the momentum transports that produce the zonal flow on a tidally locked planet. However, it only applies to the zonal mean flow, and the zonal mean of the meridional circulation. In reality, the meridional circulation on a tidally locked planet will vary greatly with longitude. [Charnay et al. \(2015\)](#) suggests an “anti-Hadley” circulation of cells in the opposite direction to Hadley cells on the night-side of a tidally locked planet.

This may make it difficult to apply the GRW mechanism in this case, as it relies

on the zonal mean of the meridional circulation. However, I will show here that in the linear limit the meridional circulation on a tidally locked planet has a zonal mean that only depends on the zonal mean of the instellation – so, the details of its longitudinal variation do not matter to the mechanism.

First, I will show that the forcing on a tidally locked planet does in fact have a non-zero zonal mean. [Showman and Polvani \(2011\)](#) forced the linear shalllow-water model by relaxing to a height field that varies sinusoidally with longitude:

$$h_{eq}(\lambda, \phi) = H_o \sin \lambda \cos \phi, \quad (1.16)$$

to admit a simple analytic solution. This radiative-equilibrium height field has zero zonal mean, so does not produce a meridional circulation. It exactly represents the stellar heating on the day-side, but does not match the real cooling on the night-side. The night-side does not cool preferentially at the antistellar point, and should instead be relaxed to a uniform height field everywhere. So, a more realistic radiative-equilibrium field is:

$$h_{eq}(\lambda, \phi) = \begin{cases} H_o + \Delta H \sin \lambda \cos \phi & |\lambda| < \pi/2 \\ H_o & |\lambda| > \pi/2 \end{cases} \quad (1.17)$$

This radiative-equilibrium height field has a non-zero zonal mean, which will produce a meridional circulation. Later, I will relax a non-linear shallow-water model to exactly this field. In this section, I will instead consider its wave-0 and wave-1 components separately.

The black line in Figure 1.8 shows the longitudinal form of this radiative equilibrium field on the equator. The red dashed line shows an approximation by a fifth-order Fourier series. The blue dashed line shows the sum of the wave-0 and wave-1 Fourier components (the solid blue lines), which approximates the real field and cru-

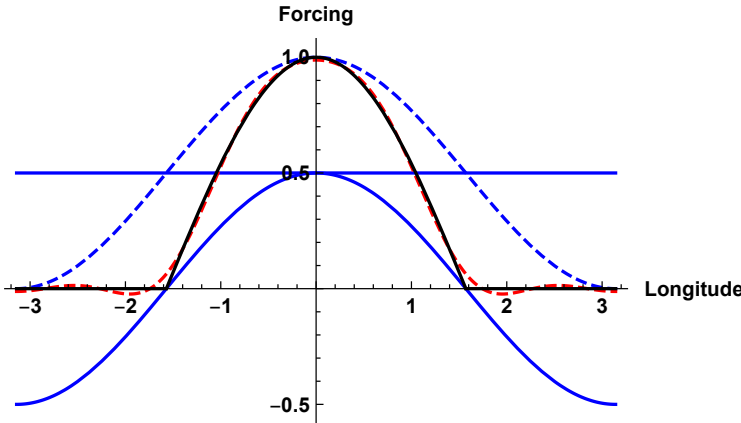


Figure 1.8: The Fourier series of the realistic forcing.

cially has a non-zero zonal mean. The first-order term corresponds to the radiative equilibrium field in [Showman and Polvani \(2011\)](#) – adding the zeroth-order term adds a non-zero zonal mean.

Now, I will show that in the linear limit the meridional circulation is only governed by the zonal mean of the forcing (the zeroth-order term in Figure 1.8). [Held and Hou \(1980\)](#) show that the properties of the meridional circulation – zonal and meridional velocities, meridional momentum flux etc. – are linear with respect to the forcing. This holds separately at every longitude. The linearity of any property X with respect to the forcing Q means that for axisymmetric forcing, the zonal mean of X has the property:

$$\overline{X} \sim \overline{Q} = Q(\phi) = Q_0 \cos \phi. \quad (1.18)$$

For the same forcing on a tidally locked planet, the forcing is $Q(\phi, \lambda) = Q_0 \cos \phi \sin \lambda$ on the day-side, plus a uniform relaxation on the night-side. So, the zonal mean is:

$$\overline{X} \sim \overline{Q} = Q(\phi, \lambda) = Q_0 \cos \phi \overline{\sin \lambda}, \quad (1.19)$$

where the mean of the $\sin \lambda$ is only taken over the day-side, giving:

$$\bar{X} \sim Q_o \cos \phi, \quad (1.20)$$

When the meridional circulation depends linearly on the local forcing, its zonal mean will therefore depend linearly on the zonal mean of the global forcing. So, it is possible to consider the zonal-mean effect of the meridional circulation on a tidally locked planet as entirely due to the wave-0 (zonal mean) component of the forcing.

Figure 1.9 shows this in practice in the two GCM simulations detailed earlier, Tests 1 and 2. It shows the time-mean results of the first day of spin-up of these simulations from rest, where the response to the applied forcing is still small and linear. The leftmost panels show the highly different zonal winds at the surface of the tidally locked Test 1, and the surface of the axisymmetric Test 2. However, the next panels are the zonal mean zonal-wind of each test, showing the identical subtropical jets beginning to be formed by the mean meridional circulation in each case. These are the same due to the linearity demonstrated above – the mean meridional circulation only depends on the zonal mean of the forcing, which is the same in Tests 1 and 2. The final panels show the same effect – each test has the same zonal-mean mass streamfunction, as the meridional circulation is the same.

This means that the effect of the mean meridional circulation on the zonal mean momentum equation (through term I in Equation 1.11) is the same in the tidally locked Test 1 as in the axisymmetric Test 2. In reality, as each test spins up the linear assumption will become less accurate and the zonal flow will affect the meridional circulation. But, the results shown in this section suggest that this circulation can be qualitatively understood in the same way on a tidally locked planet as on an axisymmetrically forced planet with the same zonal-mean forcing. The equatorward momentum transport on a tidally locked planet can then produce equatorial super-

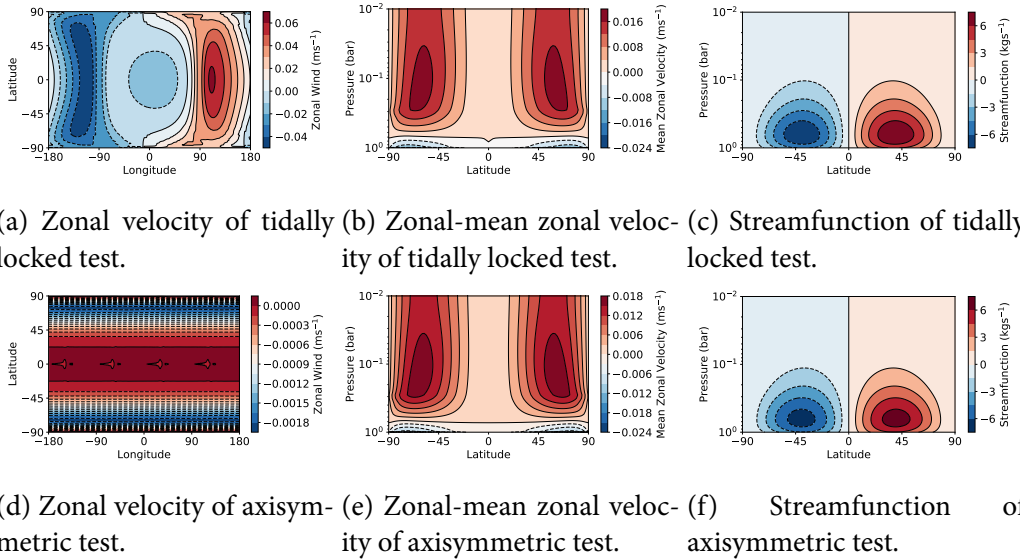


Figure 1.9: Time-mean results from the first day after spin-up from rest of two tests in Exo-FMS. The top row shows a tidally locked planet, and the bottom row shows a planet with axisymmetric forcing with the same zonal mean. The zonal mean zonal velocity and mean mass streamfunction are the same in both cases, despite the large differences in the longitudinal distribution of zonal velocity.

rotation, while preserving westerly flow at high latitudes if the meridional circulation and subtropical jets are strong enough.

1.2.3 Linear Model of GRW

Figure 1.4 showed how the linear shallow-water model in [Showman and Polvani \(2011\)](#) predicts equatorial superrotation, but requires easterly acceleration at high latitudes. In this chapter, I have introduced the idea that a meridional circulation can produce westerly acceleration at high latitudes, resulting in westerly flow at all latitudes. This can be demonstrated simply in a modified version of the linear shallow-water model.

Figure 1.10 shows the zonal-mean zonal acceleration in this linear model, when a zonally uniform background meridional velocity $\bar{V}(y) = V_0 \sin y / y_0 e^{-y^2/2}$ is imposed. The meridional scale is $y_0 = \sqrt{2}$ as before and in [Matsuno \(1966\)](#), and the

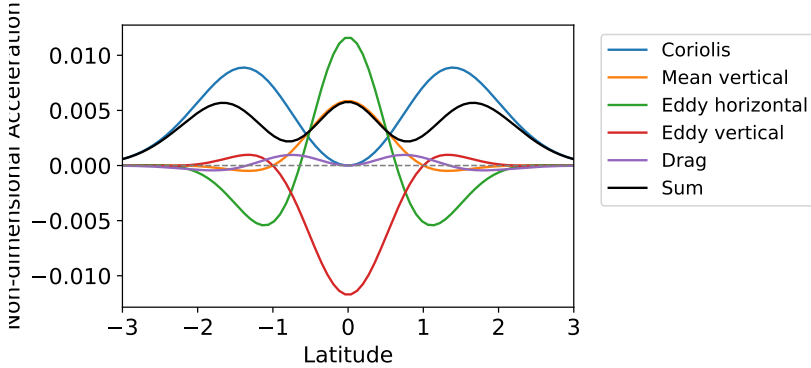


Figure 1.10: Acceleration terms in the zonal-mean zonal momentum equation (Equation 1.11), with an imposed uniform zonal-mean meridional velocity $\bar{V}(y) = V_0 \sin y / y_0 e^{-y^2/2}$, showing prograde westerly acceleration at all latitudes.

scale of the velocity is $V_0 = 0.02$. The approximations and additional parameters required to include a realistic meridional circulation such as that in [Held and Hou \(1980\)](#) motivated this simple representation.

The imposed meridional velocity affects Term I in Equation 1.11, producing a westerly acceleration at high latitudes around the peak of the imposed meridional flow $\bar{V}(y)$. This opposes the easterly acceleration due to horizontal momentum transport from stationary eddies in the previous linear model, producing westerly prograde acceleration at all latitudes if the meridional velocity is large enough. In the GRW mechanism, this reflects the fact that the equatorward momentum transport from stationary eddies is moving momentum from a region that is already accelerated eastward by the meridional circulation.

So, rather than requiring easterly flow above a certain latitude as in the linear model of [Showman and Polvani \(2011\)](#), this model requires sub-rotating flow above a certain latitude – but, the flow can still be eastward. Next, I will use a GCM and a non-linear shallow-water model to demonstrate the same mechanism with realistic forcing and meridional circulation.

1.2.4 Demonstration of GRW Mechanism

I have suggested how a GRW mechanism could operate on a tidally locked planet, and demonstrated its form in a linear shallow-water model. In this section, I will show the formation of zonal flow in the two earlier simulation Test 1 and Test 2, and the momentum balance reached in Test 1.

The first row of Figure 1.11 shows the development of the zonal-mean zonal wind as it spins up from rest in the axisymmetric case, Test 2. The forcing gradient between the equator and the pole results in a mean meridional circulation that rapidly produces subtropical jets, which strengthen with time until they reach equilibrium. Note that there is no eastward flow at the equator, and the superrotation index is negative everywhere as there is no process to transport momentum equatorward.

The second row of Figure 1.11 shows the development of the zonal-mean zonal wind as it spins up from rest in the tidally locked case, Test 1. The first panel shows that exactly the same subtropical jets form at the start of the spin-up as in the axisymmetric case, due to the linear response as explained previously. In the next panel, the stationary waves induced by the stationary forcing transport momentum towards the equator, producing eastward superrotating flow there. This weakens the subtropical jets, but they are still present at high latitudes. In the final panel, the equatorward transport has produced a strong single equatorial jet, with no distinct subtropical jets present. The balance between these the equatorward transport and the mean meridional circulation determines the relative strength of the equatorial and subtropical jets, which I will investigate in more detail later.

Figure 1.12 shows the time-mean zonal-mean zonal velocity and the resulting drag for Test 1 from 500 to 1500 days (the same as the final panel of 1.11). The second panel shows the effect of the linear Rayleigh drag applied in the boundary layer, which decays linearly with pressure away from the surface to zero at 70% of the sur-

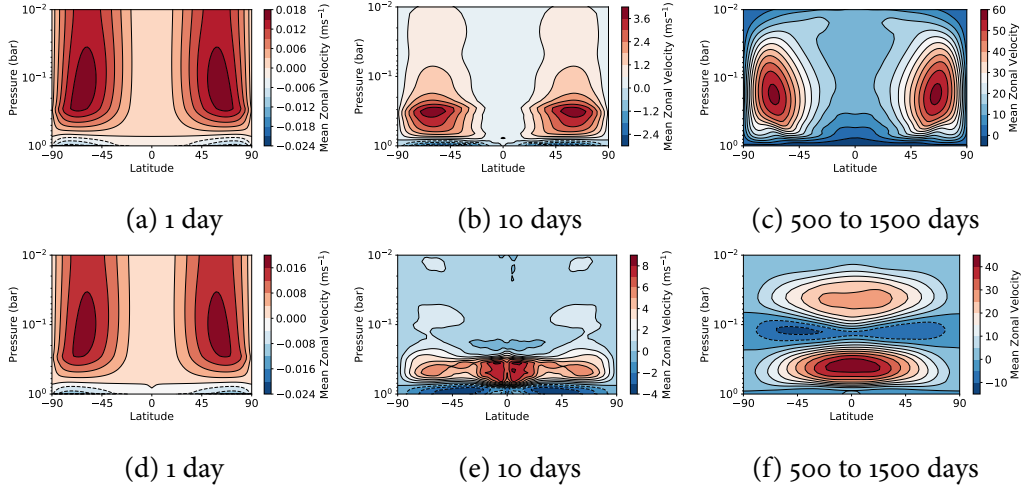


Figure 1.11: The zonal-mean zonal velocity of the tidally locked planet in Test 1, and the axisymmetrically forced planet in Test 2, as they spin up from rest.

face pressure. There is a positive westerly acceleration due to drag at the surface due to the surface easterlies formed by the mean meridional circulation. This drag pumps prograde momentum into the atmosphere, which is responsible for the increase in angular momentum during spin-up shown by Figure 1.6.

Now, I will diagnose the zonal momentum budget in Test 1 to show that the balance of momentum fluxes is consistent with the GRW mechanism. The steady-state zonal-mean momentum equation is (Lutsko, 2018):

$$\frac{\partial \bar{u}}{\partial t} = f[\bar{v}] - \underbrace{\frac{[\bar{v}]}{a \cos \phi} \frac{\partial}{\partial \phi}([\bar{u}] \cos \phi)}_{Ia} - \underbrace{[\bar{\omega}] \frac{\partial [\bar{u}]}{\partial p}}_{Ib} - \underbrace{\frac{1}{a \cos^2 \phi} \frac{\partial}{\partial \phi}([\bar{u}^* \bar{v}^*] \cos^2 \phi)}_{IIa} - \underbrace{\frac{\partial}{\partial p} [\bar{u}^* \bar{\omega}^*]}_{IIb} + \underbrace{[\bar{F}_x]}_{III} \quad (1.21)$$

Terms Ia and Ib are the mean horizontal and vertical momentum transport due to the mean meridional circulation. Term IIa is the eddy horizontal momentum transport due to the stationary eddy response to the stellar forcing, and Term IIb is the eddy vertical momentum transport due to vertical motion. This vertical motion

is mostly due to air rising at the substellar point and subsiding on the night-side. Term III is the zonal momentum forcing, which is the Rayleigh drag shown in Figure 1.12.

Figure 1.13 shows each of the momentum transport terms in Equation 1.21. Term Ia is plotted in Figure 1.13a, which shows how the mean meridional circulation produces an acceleration in the midlatitudes in its poleward branch and has no effect at the equator. Figure 1.13b shows Term Ib, and how the mean meridional circulation produces a deceleration at high latitudes in the jet layer as it moves prograde momentum down.

Figure 1.13c plots Term IIa, and shows how the stationary waves excited by the stellar forcing transport momentum horizontally towards the equator. This produces an acceleration there and a deceleration at higher latitudes. Term IIb in Figure 1.13d shows how the vertical eddy momentum transport decelerates the jet. It moves stationary air up on the day-side, reducing the specific westerly angular momentum of the jet. Term IIb also moves westerly angular momentum down on the night-side, decelerating the jet. This produces some westerly acceleration in the boundary layer below the jet, which is responsible for the easterly drag seen there in Figure 1.12.

Figure 1.14 shows each term in Figure 1.13 at the pressure level corresponding to the maximum zonal-mean zonal velocity (the centre of the equatorial jet). This shows that the Terms Ia and IIa balance at high latitudes, and that Term IIb balances Terms IIa and Ib at the equator, as shown in the linear model in Figure 1.10. In the next section, I will use a non-linear shallow-water model to reproduce this process, and show that the same balance of acceleration terms applies.

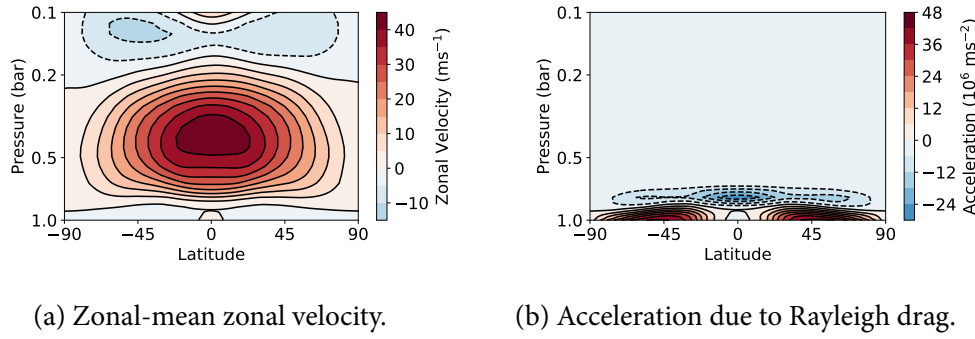


Figure 1.12: Zonal velocity and drag

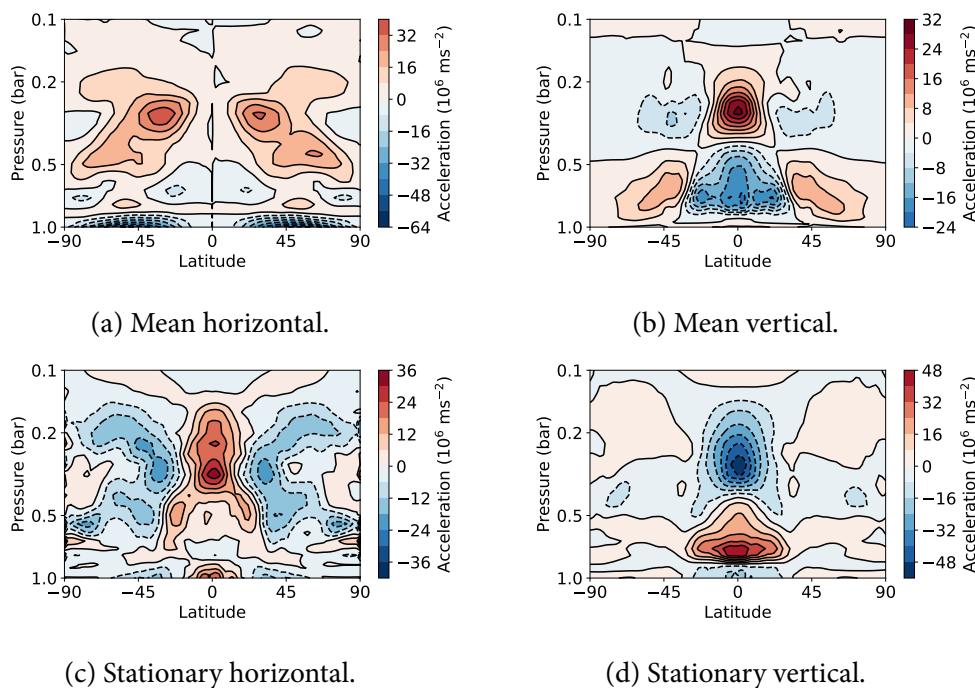


Figure 1.13: Mean and eddy acceleration.

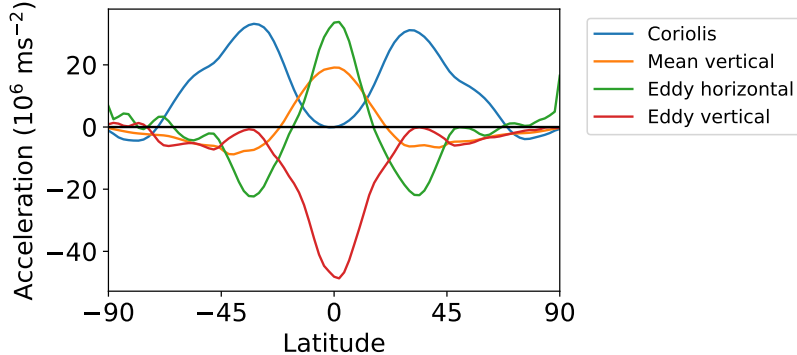


Figure 1.14: Acceleration terms in the zonal-mean zonal momentum equation for Test 1 in Exo-FMS, showing how Terms Ia and IIa in Equation 1.21 balance at high latitudes, and that Term IIb balances Terms IIa and Ib at the equator (as in Figures 1.10 and 1.18).

1.3 Non-Linear Model of the Meridional and Zonal Circulation on a Tidally Locked Planet

In this section, I show the GRW mechanism on a tidally locked planet in a non-linear shallow-water model. I will show the effect of the realistic radiative-equilibrium forcing field introduced earlier, and the effects of its wave-0 and wave-1 forcing components. The balance of momentum fluxes for steady-state zonal flow is the same in this non-linear model as in the GCM and in the linear shallow-water model, suggesting that the GRW mechanism is a robust description of the formation of this zonal flow.

1.3.1 Model

The GFDL Spectral Dynamical Core (GFDL-SDC) is a single-layer model that solves the non-linear shallow-water equations. The model is forced by relaxation to a radiative equilibrium height field h_{eq} . The only other forcing on the model is the correction to the zonal momentum R introduced by [Shell and Held \(2004\)](#) that was

discussed earlier.

The tests have zero dynamical damping applied to their velocity fields to be consistent with the GCM simulations, where dynamical damping is not a relevant factor at the level of the equatorial jet. This is not consistent with the earlier linear shallow-water model, where dynamical damping allows an analytic solution to the model. However, [Hammond and Pierrehumbert \(2018\)](#) showed that dynamical damping does not greatly affect the form of the global circulation once the zonal flow has formed.

1.3.2 Results

I ran three simulations in the model which were forced by being relaxed to different radiative equilibrium height fields h_{eq} . The models were run for 100 days, and the results taken over the last 10 days after a steady state had formed. All of the tests in this section have $h_o = 10$ km, $\Delta h = 1$ km, and a thermal damping time of 0.1 days. Figures 1.15, 1.17, and 1.17 show the height fields and zonal-mean zonal and meridional velocities of each test.

Test A is forced by relaxing to the equilibrium height field:

$$h_{eq} = h_o + \Delta h \sin \lambda \cos \phi. \quad (1.22)$$

This gives equal and opposite day-side and night-side forcings, which produce wave-1 stationary waves and equatorial superrotation. This is the same system as that shown in Figure 8 of [Showman and Polvani \(2011\)](#).

The height field in Figure ?? shows this stationary wave pattern, and Figure ?? shows the eastward equatorial flow and westward flow at high latitudes. With a forcing of this form (with zero zonal mean) there must always be westward flow at high latitudes as shown above, so this system cannot explain the formation of the eastward

flow at all latitudes seen in some GCM simulations.

Test B shows a test relaxed to an axisymmetric field:

$$h_{eq} = h_o + \Delta h \cos \phi / \pi. \quad (1.23)$$

This is equivalent to the wave-0 component of the “realistic” radiative-equilibrium field in Section 1.2.2. It produces the same type of meridional circulation as the non-linear model in [Shell and Held \(2004\)](#). This Hadley circulation adds momentum to the layer represented by the shallow-water model, producing westerly zonal flow at high latitudes to conserve angular momentum. In a real atmosphere, momentum would be conserved by the formation of easterly flow in the lower branch of the circulation (although as shown earlier, this is dragged by the surface, resulting in net positive westerly momentum after all).

Test C shows the effect of forcing by relaxation to the “realistic” radiative-equilibrium field in Section 1.2.2, with a sinusoidal forcing on the day-side and a uniform equilibrium height field on the night-side:

$$h_{eq} = \begin{cases} h_o + \Delta h \sin \lambda \cos \phi & (|\lambda| < \pi/2) \\ h_o & (|\lambda| > \pi/2) \end{cases} \quad (1.24)$$

This can be thought of as a combination of Test A and Test B (those tests had the same forcing as the zeroth- and first-order components of this realistic field). Figure ?? shows a similar height field to Test A. Figure ?? shows a meridional circulation and subtropical jets similar to Test B, produced by the non-zero zonal mean of the forcing field. It also has an equatorial jet similar to Test A, produced by the stationary waves due to the wave-1 component of the forcing. This demonstrates the Giersch mechanism discussed previously, and allows the shallow model to have westerly flow at all latitudes.

As discussed previously, Test C can support westerly flow at all latitudes as the superrotating flow at the equator only needs to be compensated by subrotating flow at higher latitudes, which can still be westerly. Test A, on the other hand, requires easterly flow at high latitudes to conserve angular momentum given a westerly equatorial jet. The strength of the equatorial and subtropical jets depend on the planetary parameters, which I will investigate in Section 1.4.1.

Now, I will diagnose the terms in the zonal-mean momentum equation to show that the balance of sources of momentum transport is the same as in the GCM and in the linear shallow-water model. In a spherical geometry, the zonal-mean momentum equation is:

$$\frac{\partial \bar{u}}{\partial t} = \underbrace{\bar{v}^* \left[f - \frac{1}{a \cos \phi} \frac{\partial (\bar{u} \cos \phi)}{\partial \phi} \right]}_{\text{I}} - \underbrace{\frac{1}{\bar{h} a \cos^2 \phi} \frac{\partial}{\partial \phi} \left[(\bar{h} v)' u' \cos^2 \phi \right]}_{\text{II}} + \underbrace{\left[\frac{1}{\bar{h}} \bar{u}' Q' + \bar{R}_u^* \right]}_{\text{III}} - \underbrace{\frac{\bar{u}^*}{\tau_{\text{drag}}} - \frac{1}{\bar{h}} \frac{\partial (\bar{h}' u')}{\partial t}}_{\text{IV}} \quad (1.25)$$

Figure 1.18 shows these terms for the steady-state flow in Test C. Comparing this to Figure 1.14 shows that the same balance applies in Test C in the non-linear shallow-water model as in Test 1 in the GCM. At the equator, the horizontal stationary momentum flux (Term II) balances the vertical stationary momentum flux (Term III). At high latitudes, the horizontal mean momentum flux (Term I) balances the horizontal stationary momentum flux (Term II).

I suggest that this agreement between the non-linear shallow-water model and the GCM shows that the shallow-water model captures the mechanism forming the zonal flow profile in the GCM. This shows that the important processes in the atmosphere can be split up into the wave-1 day-night forcing, and the wave-0 zonal-mean forcing due to the asymmetry between the day-side cooling and uniform night-side

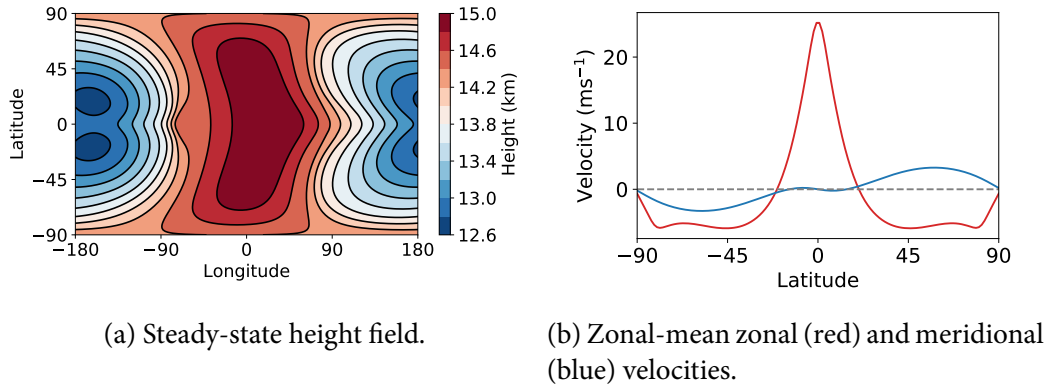


Figure 1.15: Test A, sinusoidal forcing

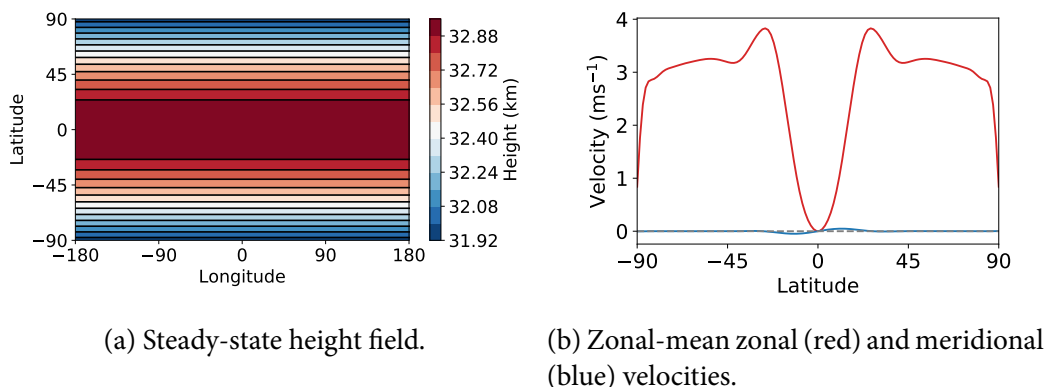


Figure 1.16: Test B, axisymmetric forcing

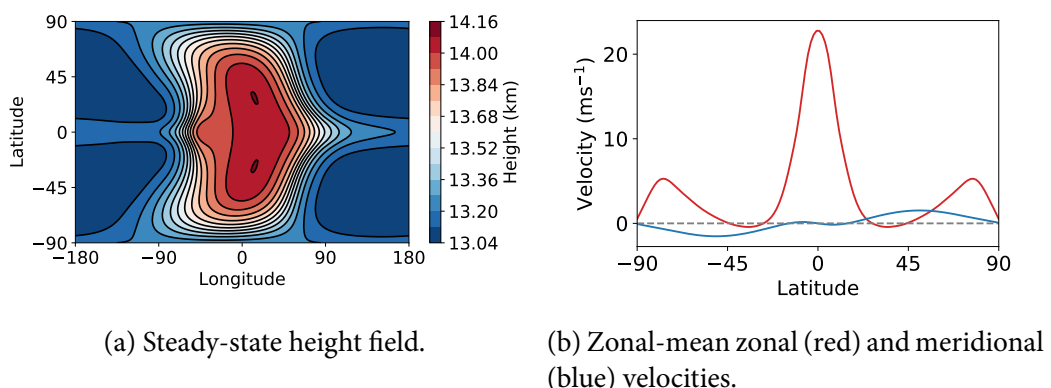


Figure 1.17: Test C, realistic forcing

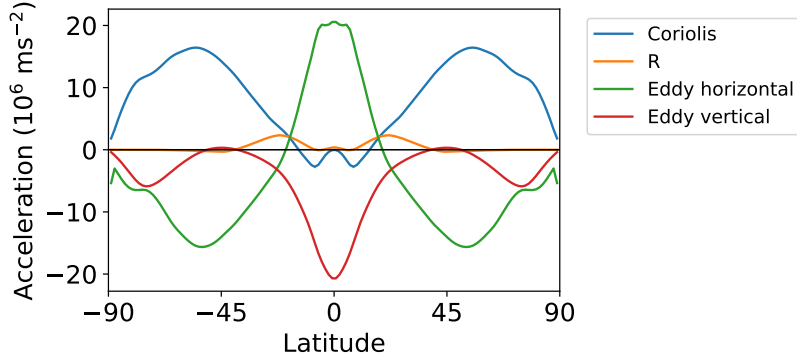


Figure 1.18: The terms in the zonal-mean zonal momentum equation (Equation 1.25) for Test 3 with realistic forcing in the non-linear shallow-water model, showing how balance is achieved differently at the equator and at high latitudes. Note the same balance of forces as in Figures 1.10 and 1.14.

cooling. In the next section, I will apply the GRW mechanism to predict scaling relations for the zonal flow in the non-linear shallow-water model and the GCM.

1.4 Scaling Regimes for Zonal Jets on Tidally Locked Planets

In this section, I will use the ideas developed so far to predict how the strengths and positions of the zonal jets in the atmospheres of tidally locked planets could scale with planetary parameters. I will test these predictions in the non-linear shallow-water model and in the GCM.

1.4.1 Non-Linear Model Scaling Relations

Equation 1.25 shows how each source of acceleration scales with the planetary parameters. Term II drives the equatorial jet, suggesting that the jet speed should scale like $\frac{1}{h} \frac{\partial}{\partial y} \left[\overline{(hv)'u'} \right] \sim u'v' \sim Q^2 \alpha^2$. Term I in Equation 1.25 drives the subtropical jets, suggesting that they should scale like $\bar{v}^* \left[f - \frac{\partial \bar{u}}{\partial y} \right] \sim v/f \sim Q\alpha f$.

Figure 1.19 shows the scaling of the zonal-mean equatorial and subtropical jet speeds with the forcing, via the magnitude of the perturbation to the radiative-equilibrium height field h_o . Each test has the same parameters as Test C in Section 1.3, except for the magnitude of the forcing. The figure shows that for low forcing values, the equatorial jet does scale quadratically with the forcing (as identified by [Showman and Polvani \(2011\)](#)), and the subtropical jets scale linearly. For forcing values higher than $\Delta h/h_o = 0.01$, the jets increase more slowly than linearity, as non-linear effects become more important. However, this test shows that the accelerations of the jets scale as expected in the linear limit, and that the magnitude of forcing required for an approximately linear response is still consistent with that in [Showman and Polvani \(2011\)](#).

This predicts that in general, increasing the forcing (instellation) on a tidally locked planet will increase both the equatorial and subtropical jet speeds, and will increase the equatorial jet speed relative to the subtropical jets. In addition, the equatorial acceleration comes at the expense of the subtropical jets due to the equatorward momentum transport, so for very strong forcing the subtropical jets may be replaced by easterly flow. This qualitative behaviour will be shown later in the GCM.

1.4.2 GCM Qualitative Scaling Relations

In this section, I will qualitatively apply the scaling relations from the non-linear shallow-water model to a suite of GCM simulations. Figure 1.20 shows the time-mean zonal-mean zonal velocity of nine GCM simulations with different rotation rates and instellation values, produced for [Pierrehumbert and Hammond \(2018\)](#). These tests have a wide range of zonal flow patterns, with one, two, or three jets of varying strengths and positions. These can be qualitatively explained with the scaling relations of the previous section.

First, the effect of the instellation. In the GCM, increasing the stellar forcing in-

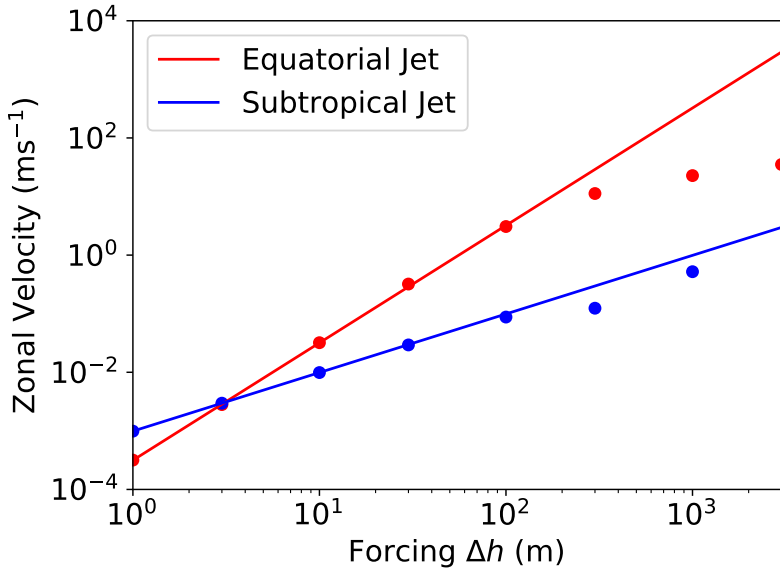


Figure 1.19: The scaling of the equatorial and subtropical jet speeds in the non-linear shallow-water model, for cases with realistic forcing with variable values of forcing magnitude Q .

creases the forcing Q , and raises the damping rate α (due to the higher temperature). I showed previously that increasing the forcing Q and damping α in the shallow-water model increases the strength of all the zonal jets, and increases the strength of the equatorial jet relative to the subtropical jets. This explains why the GCM tests with higher instellation have stronger equatorial jets, with all the “hot” tests having one single jet centred on the equator. The “hot, 2 day” test has easterly flow at high latitudes, as the high forcing increases the prograde momentum transport towards the equator.

The dominant effect of increasing the rotation rate in the non-linear model was to increase the strength of the subtropical jets, and to move them to lower latitudes. The effect on the equatorial jet is weaker and more complex. This is what happens in the GCM tests, as each test at faster rotation rate has relatively stronger subtropical jets, at lower latitudes. This effect is clearest in the “cold” cases, as in the warmer cases at

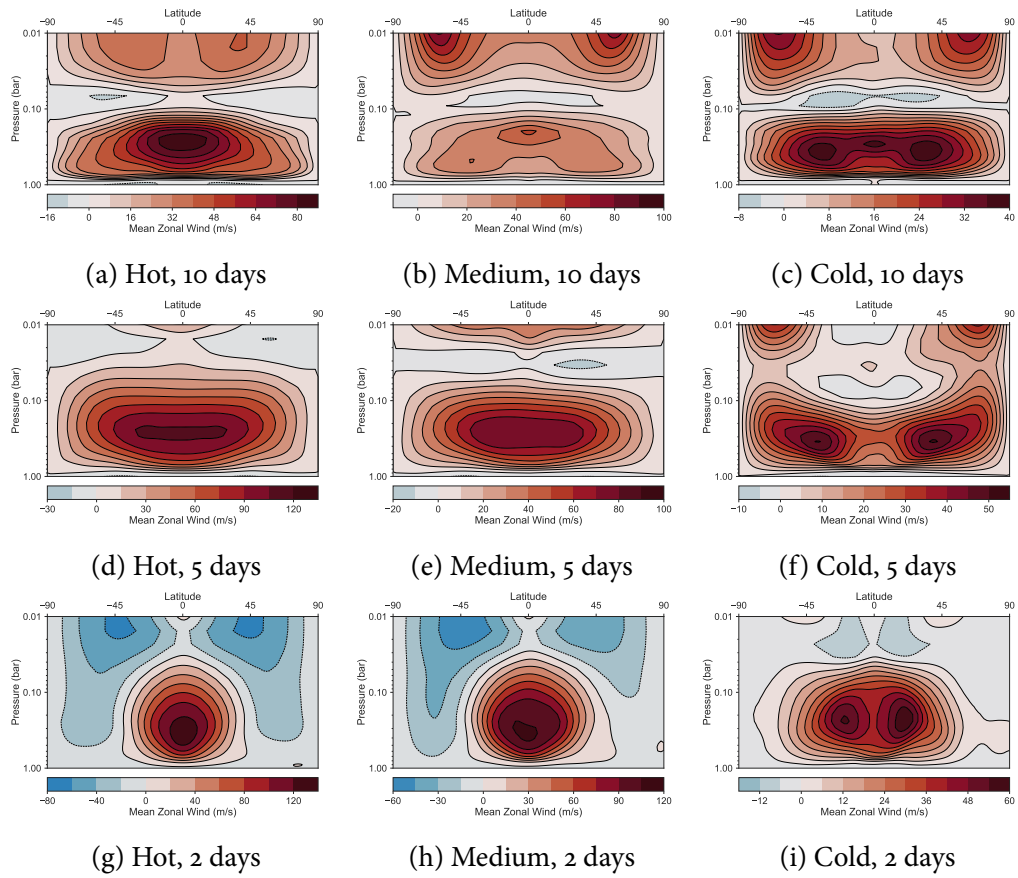


Figure 1.20: Zonal-mean zonal flow of a suite of tests in the GCM Exo-FMS, showing how the equatorial and subtropical jet speeds and positions depend on instellation and rotation rate ([Pierrehumbert and Hammond, 2018](#)).

high rotation rate, the subtropical jets merge with the equatorial jet and there appears to only be one jet.

The mechanism discussed in this section, and the scaling relations shown in the non-linear model, provide a way to understand why GCM simulations of tidally locked planets can have one, two, or three zonal jets, and to understand how their speeds depend on the planetary parameters.

1.5 Discussion

In this chapter, I have mostly considered idealised models and have made assumptions about the nature of the planets they represent. In this section, I will discuss some complicating aspects of applying the GRW mechanism to real tidally locked planets.

A large assumption of the mechanism in Figure 1.7 is that the meridional circulation is essentially global, transporting air from the equator to the pole. This is not the case for a planet with a sufficiently rapid rotation rate, like the Earth which supports multiple cells of meridional circulation. If a tidally locked planet was rotating rapidly enough to limit the meridional extent of these cells, the GRW mechanism might only operate below a certain latitude, where the meridional circulation reaches. This may be the case in the more rapidly rotating tests in Figure 1.4.2, where the subtropical jets are closer to the equator and there can be easterly flow at high latitudes.

However, these tests show that a global meridional circulation is not strictly necessary for the GRW mechanism to function, just that it cannot be thought of as acting on a single global layer. The limited meridional circulation still crucially receives westerly angular momentum from the surface and conveys it to the jet layer – it is just that the jets formed are closer to the equator, and the behaviour at high latitudes may be unaffected by this circulation.

The meridional circulation can also be more complicated on tidally locked gas giants like Hot Jupiters, which do not have a surface to bound the meridional circulation and apply drag to its lower branch. [Heng et al. \(2011\)](#) and [Mendonça et al. \(2018\)](#) showed that the meridional circulation of a Hot Jupiter has a direct Hadley-cell like circulation above a certain pressure level, with indirect cells directly below this. This is a more complex situation than in the terrestrial planets considered in this chapter, and is similar to some models of Venus which have direct cells above indirect

cells (Sugimoto et al., 2019). The equatorial superrotation in these Hot Jupiter simulations is still in the same region as the direct cells, so it may be possible to consider the same GRW mechanism at work in this region.

I suggest that the transition between the direct and indirect corresponds to the level of heating. The direct cells then behave as in the terrestrial case. In gas giants, they may act the same as the surface in the terrestrial case, linking the upper level flow to the deep atmosphere or an imposed surface. The drag from this surface can then act the same as the drag from a terrestrial surface, although it is applied via the indirect cells. The deep atmosphere may fulfil the same role as a surface if there is no explicit bottom drag, providing a reservoir for retrograde flow deep down.

Finally, this chapter has not considered an important mechanism discussed in detail for Hot Jupiters by Showman et al. (2015) – the formation of westerly midlatitude jets by baroclinic instability generated in that region. This can also transport enough westerly momentum away from the equator to reduce the strength of the equatorial jet, and even to reverse its direction. This could be added to the GRW picture as another source of horizontal transport of zonal momentum in the layer of the jet. Laraia and Schneider (2015) considered a similar situation on non-tidally locked planets, estimating the effect of both equatorward momentum transport due to equatorial waves, and transport away from the equator due to baroclinic instability.

This additional transport is important for more rapidly rotating planets, and so is not important for planets such as those simulated earlier with 10 day periods. However, in a full consideration of the formation of zonal flow on tidally locked planets it cannot be ignored, especially for Hot Jupiters or more rapidly rotating terrestrial planets. It may be possible to classify planets into different regimes, where either the meridional circulation, stationary wave forcing, or baroclinic instability dominates the formation of zonal jets (Showman et al., 2015).

1.6 Conclusions

In this chapter, I have shown how the GRW mechanism describes the formation of the zonal flow in GCM simulations of the atmospheres of terrestrial tidally locked planets. I demonstrated this mechanism in linear and non-linear shallow-water models, and showed how different terms in the zonal-mean zonal momentum equation balance at the equator, and at high latitudes.

This mechanism provides an understanding of the strength of the equatorial jet relative to jets at high latitudes. I used this to predict scaling relations for the jet speeds in the non-linear shallow-water model and the GCM.

In conclusion, applying this mechanism to tidally locked planets allows greater understanding of the zonal flow patterns that they form. In the next chapter, I will relate this zonal flow to the global circulation and temperature distribution of the atmosphere, and its observable effects.

CHAPTER 2

Wave-Mean Flow Interactions in a Linear Theory of Tidally Locked Atmospheres

Simulations and observations of tidally locked planets suggest that they form strong zonal eastward jets centred on the equator, which play an important role in distributing heat from the day-side to the night-side. This chapter shows how a shallow-water model linearised around a zonal flow $\bar{U}(y)$ can match GCM simulations and observations of tidally locked planetary atmospheres. The zonal flow is the key to explaining the hot-spot shift and global circulation of the planet, due to the Doppler-shift of the stationary waves discussed in Chapter 1 ([Tsai et al., 2014](#)).

In Section 2.1, I will discuss the response to forcing of the shallow-water model in [Showman and Polvani \(2011\)](#), and show how the zonal flow discussed in Chapter 1 can affect this response. Then, in Section 2.3 I will linearise the shallow-water model of [Showman and Polvani \(2011\)](#) around a shear zonal flow $\bar{U}(y)$ and its associated geostrophic height perturbation $\bar{H}(y)$. This differs from [Showman and Polvani \(2011\)](#) which used zero background flow $\bar{U}(y) = 0$ and uniform background height $\bar{H}(y) = H_0$. It also differs from [Tsai et al. \(2014\)](#) which used uniform background flow $\bar{U}(y) = U_0$ and uniform background height $\bar{H}(y) = H_0$ (which is inconsistent

- a geostrophically balanced uniform flow $\bar{U}(y) = U_0$ gives a non-uniform height field $\bar{H}(y)$.

In Section 2.4, I will construct the same linear model on a sphere rather than on a beta-plane, for direct comparison with GCM simulations and real planets. I will then use this model to predict how the observable features of the global circulation qualitatively scale with different planetary parameters.

Finally, I will discuss the specific mechanism behind the observable “hot-spot shift” on such planets. I will conclude that the success of the shallow-water model linearised about $\bar{U}(y)$ and $\bar{H}(y)$ show that this zonal flow is key to setting the global circulation pattern of tidally locked planetary atmospheres. In the following chapters, I will use this to interpret simulations and observations of real planets.

2.1 Linear Shallow-Water System in Zonal Flow

In Chapter 1, I introduced the linear shallow-water equations and showed the stationary wave response to the day-night forcing on a tidally locked planet. In this chapter, I will show how the zonal flow produced by this response affects the stationary waves themselves.

In this section, I will linearise the equations about a uniform eastward zonal flow $\bar{U}(y) = U_0$, and show how the flow Doppler-shifts the maximum of the forced response eastwards ([Tsai et al., 2014](#)). This will be the dominant effect of the more realistic shear flow $\bar{U}(y)$ later in this section. The uniform flow is easier to consider first, as it still has an analytic solution.

The linear shallow-water equations (as used in Section 1) are:

$$\begin{aligned}\frac{\partial u}{\partial t} - \beta y v + \frac{\partial h}{\partial x} &= 0, \\ \frac{\partial v}{\partial t} + \beta y u + \frac{\partial h}{\partial y} &= 0, \\ \frac{\partial h}{\partial t} + c^2 \left(\frac{\partial u}{\partial x} + \frac{\partial v}{\partial y} \right) &= Q(x, y).\end{aligned}\tag{2.1}$$

where h are the zonal and meridional velocities, h is the height, and $c = \sqrt{gH}$ is the gravity wave speed (Matsuno, 1966). As before, these are non-dimensionalized with time scale $\sqrt{1/c\beta}$ and length scale $\sqrt{c/\beta}$, and all quantities will be assumed to have the form $f(y)e^{i(kx-\omega t)}$.

Now, we want to see the effect of a uniform eastward flow on these solutions, to approximate the effect of a zonal jet. If we instead linearise about the background state $U(x, y) = U_0$ rather than $U(x, y) = 0$, we get the following equations (Tsai et al., 2014):

$$\begin{aligned}\frac{\partial u}{\partial t} + U_0 \frac{\partial u}{\partial x} - \beta y v + \frac{\partial h}{\partial x} &= 0, \\ \frac{\partial v}{\partial t} + U_0 \frac{\partial v}{\partial x} + \beta y u + \frac{\partial h}{\partial y} &= 0, \\ \frac{\partial h}{\partial t} + U_0 \frac{\partial h}{\partial x} + c^2 \left(\frac{\partial u}{\partial x} + \frac{\partial v}{\partial y} \right) &= Q(x, y).\end{aligned}\tag{2.2}$$

These can be considered as Equation 2.8 in a moving frame, with the time derivative $\partial/\partial t$ replaced by the material derivative $\partial/\partial t + U_0 \partial/\partial x$ (hence the Doppler shift analogy). With explicit damping $\partial/\partial t = \alpha$ and zonal derivatives $\partial/\partial x = ik_x$, these become:

$$\begin{aligned}(\alpha_{dyn} + ik_x U_0)u - \beta y v + ik_x h &= 0, \\ (\alpha_{dyn} + ik_x U_0)v + \beta y u + \frac{\partial h}{\partial y} &= 0, \\ (\alpha_{rad} + ik_x U_0)h + c^2 ik_x u + \frac{\partial v}{\partial y} &= Q(x, y),\end{aligned}\tag{2.3}$$

for a forcing $Q(x, y) = Q_0 \sin(x) e^{-y^2/2}$, and a uniform background flow $\bar{U}(y) =$

U_o . Chapter 1 showed how the forced response $\chi = (u, v, h)$ is a sum of the free modes $\xi_m = (u_m, v_m, h_m)$, weighted by coefficients a_m

$$\chi = \sum a_m \xi_m. \quad (2.4)$$

The solutions are now the same as before, except that the complex coefficient a_m (which determines the position of each mode in the forced response) is affected by the background flow:

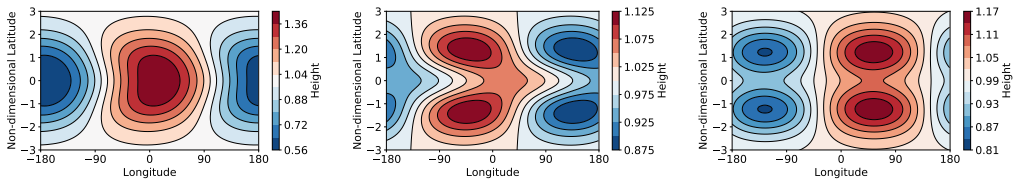
$$a_m = \frac{1}{\alpha - i(\omega_m - U_o k_x)} b_m. \quad (2.5)$$

When U_o is zero the solution is the same as before. As U_o increases, the imaginary part of the denominator becomes more positive and larger. The relative magnitude of the components of the denominator of a_m set the position of each mode m , as shown in Figure 2.1.

Figure 2.1b shows the standard forced solution of Matsuno (1966), with zero background flow and relatively weak damping. In this case, the eigenvalues of each mode sets its position – the lowest-order Rossby mode is close to -90° , and the Kelvin mode is slightly to the east of the substellar point.

Figure 2.1a shows how for a large damping α , a_m is mostly real and positive, and the mode has its maximum close to the maximum of the forcing – at the substellar point. Figure 2.1c shows that for a large background flow U_o , a_m is mostly imaginary and positive, so the maximum of the mode is close to 90° – this gives the hot-spot shift later on.

Equation 2.5 lets us estimate the parameters needed for a significant eastward hot-spot shift. The denominator of a_m must have a positive imaginary part for the forced response to appear east of the substellar point. This imaginary part must also have a greater magnitude than the real part α . So, for our system with $\alpha = 0.2$, and



(a) Zero background flow and strong damping $\alpha = 1.0$, gives the standard solution of $U_0 = 0.5$ shifts the modes forces the waves close to the [Matsuno \(1966\)](#).
(b) Zero background flow and standard damping $\alpha = 0.2$.
(c) A strong background flow and standard damping $\alpha = 0.2$, gives the standard solution of $U_0 = 0.5$ shifts the modes forces the waves close to the [Matsuno \(1966\)](#).
substellar point.

Figure 2.1: The linear responses to a forcing with magnitude $Q_0 = 1.0$ and $\alpha = 0.2$ unless specified. The positions of the various modes depends on the terms in the denominator of Equation 2.5.

the dominant lowest-order Rossby mode having $\omega_m \approx 0.254$, an eastward hot-spot shift requires $U_0 > 0.254$ and $U_0 - 0.254 > 0.2$. This means that a zonal flow of $U_0 \sim 1$ will be required for a significant hot-spot shift.

2.2 Free Modes in Shear Flow on the Beta-Plane

In this section, I will investigate the free modes of the shallow-water equations linearised about a shear background flow $\bar{U}(y)$, and the associated geostrophically balanced height perturbation $\bar{H}(y)$. I will show how the flow affects these free modes, which will be important later in understanding the response to forcing in a shear flow.

The background flow $\bar{U}(y)$ and height $\bar{H}(y)$ satisfy the second line of Equation ??, so are geostrophically balanced with $\bar{H}_y(y) = -y\bar{U}(y)$. For our Gaussian jet $\bar{U}(y) = U_0 e^{-y^2/2}$, the height perturbation is therefore $\bar{H}(y) = U_0 e^{-y^2/2}$ ([Hammond and Pierrehumbert, 2018](#)).

For the tests in this chapter, I use a forcing magnitude $Q_0 = 1$ and equal radiative and dynamical damping rates $\alpha_{rad} = \alpha_{dyn} = 0.2$ ([Matsuno, 1966](#)). I will show the effect of varying these damping rates in Section 2.3.2. The tests in this section will

show the effect of a zonal flow with a maximum non-dimensional speed between 0 and 1, as this is the speed required for a significant zonal shift of the forced response as discussed above. The value of $Q_0 = 1$ in the forcing $Q(y) = Q_0 \sin(x)e^{-y^2/2}$ was chosen to produce a comparable perturbation to that from the imposed equatorial jet, and to be consistent with [Matsuno \(1966\)](#) and [Showman and Polvani \(2011\)](#).

In Section 2.1, I showed how the response to a forcing can be written as a sum of the free modes of the system. It is not possible to write down an exact solution like this when the system is linearised about a background flow $\bar{U}(y)$ and $\bar{H}(y)$, but it is still useful to interpret the resulting solution in terms of the fundamental free modes.

I will write the free solutions to shallow-water equations as a complex function of latitude $A(y)$, and the forced solutions as functions of both latitude and longitude in the form $A(y)e^{i\delta(y)x}$. This phase $\delta(y)$ determines the longitudinal structure of the forced response, and is equivalent to the phase shift $(\omega_m - k_x \bar{U})$ derived earlier for a uniform flow.

We can still consider the response to forcing as a sum of the free modes of the system. Now the equations are linearised about a shear flow $\bar{U}(y)$ and $\bar{H}(y)$, the free modes have a different latitudinal structure $u(y), v(y), h(y)$ and have different eigenvalues ω_m (so will have different longitudinal position in the forced response).

Linearised around the background flow $\bar{U}(y)$ and height $\bar{H}(y)$, the shallow-water equations are:

$$\begin{aligned} \frac{\partial u}{\partial t} + \alpha_{dyn} u + \frac{\partial \bar{U}(y)u}{\partial x} + \left(\frac{\partial \bar{U}(y)}{\partial y} - y \right) v + \frac{\partial h}{\partial x} &= 0, \\ \frac{\partial v}{\partial t} + \alpha_{dyn} v + \frac{\partial \bar{U}(y)v}{\partial x} + yu + \frac{\partial h}{\partial y} &= 0, \\ \frac{\partial \bar{H}' u}{\partial x} + \bar{H}' \frac{\partial v}{\partial y} - y\bar{U}(y)v + \frac{\partial h}{\partial t} + \alpha_{rad} h + \frac{\partial \bar{U}(y)h}{\partial x} &= Q(y), \\ \bar{H}' &= 1 + \bar{H}(y). \end{aligned} \tag{2.6}$$

To consider the free modes of Equation 2.6, we set $Q(y) = 0$ and $\partial/\partial t = -i\omega$, and write u, v, h in the form $A(y)e^{i(k_x x - \omega t)}$:

$$\begin{pmatrix} \alpha_{dyn} + ik_x \bar{U}(y) & \frac{\partial \bar{U}(y)}{\partial y} - y & ik_x \\ y & \alpha_{dyn} + ik_x \bar{U}(y) & \frac{\partial}{\partial y} \\ ik_x \bar{H}' & -y \bar{U}(y) + \bar{H}' \frac{\partial}{\partial y} & \alpha_{rad} + k_x \bar{U}(y) \end{pmatrix} \begin{pmatrix} u \\ v \\ h \end{pmatrix} = i\omega \begin{pmatrix} u \\ v \\ h \end{pmatrix}, \quad (2.7)$$

$$\bar{H}' = 1 + \bar{H}(y).$$

The background state of $\bar{U}(y)$ and $\bar{H}(y)$ must satisfy Equation 2.6 by itself. On the beta-plane, this means that the shear flow $\bar{U}(y)$ is geostrophically balanced by the height perturbation $\bar{H}(y)$. The second line of Equation 2.6 requires that the background state is:

$$\begin{aligned} \bar{U}(y) &= U_0 e^{-y^2/2} \\ \bar{V}(y) &= 0 \\ \bar{H}(y) &= U_0 e^{-y^2/2} \end{aligned} \quad (2.8)$$

I have considered the perturbations in the forced system to apply to a single shallow-water layer of height H_0 , non-dimensionalised to unity. Technically, the vertically varying heating profile in a planetary atmosphere excites a continuum of vertical modes, each defining a shallow-water system of different H_0 . However, Tsai et al. (2014) showed that in this forced shallow-water system, almost all of the energy is confined to the lowest-order vertical mode, making the assumption that a real atmosphere is described well by a single shallow-water layer reasonable.

2.2.1 Free Mode Eigenvalues

I found the free modes of the shallow-water system defined by Equation 2.7 for a background flow $\bar{U}(y) = U_0 e^{-y^2/2}$ with a variable magnitude U_0 , using the method

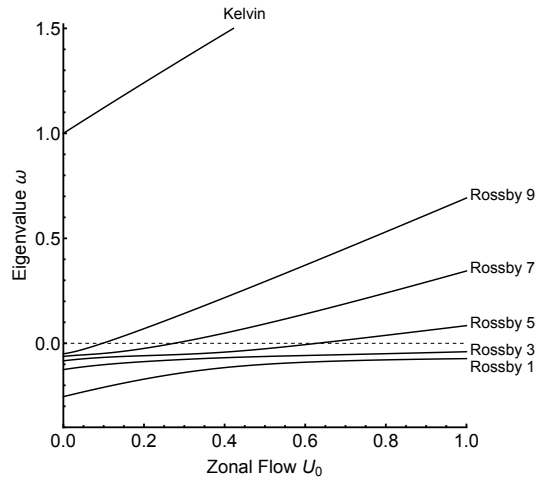


Figure 2.2: The eigenvalues of the free modes of Equation 2.7, showing how eastward flow makes the eigenvalues more positive. This corresponds to an eastward shift in the response to forcing.

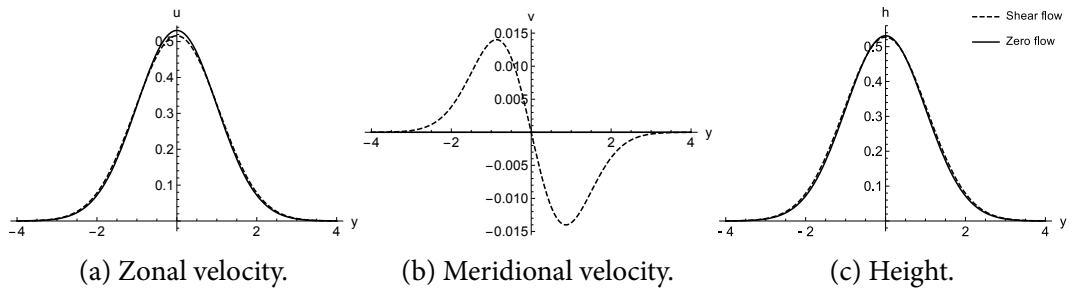


Figure 2.3: The meridional structure of the free Kelvin mode, with and without a background shear flow (Hammond and Pierrehumbert, 2018). The flow introduces a non-zero meridional velocity.

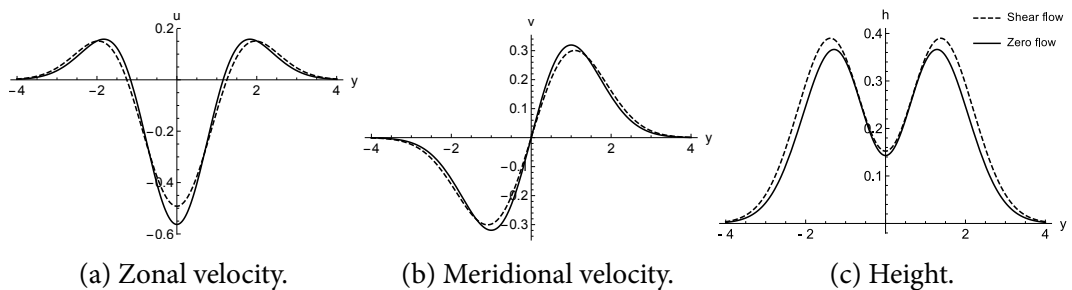


Figure 2.4: The meridional structure of the free Rossby mode, with and without a background shear flow. The shear affects the meridional structure, effectively changing the y coordinate (Hammond and Pierrehumbert, 2018)

in Appendix X (Hammond and Pierrehumbert, 2018). Figure 2.2 shows the real parts of the eigenvalues of the lowest-order (so largest magnitude) modes excited by the symmetric, stationary forcing. These are the free Kelvin mode and the symmetric free Rossby modes of Equation 2.7 (Matsuno, 1966).

The value and sign of these eigenvalues determine the position of the free mode in the forced response, as discussed in Section 2.1. Note that an exact forced solution in terms of a series of free modes is now not possible as the flow is not uniform, but it is still very useful to interpret the forced response in this way.

As the magnitude U_o of the equatorial jet $\bar{U}(y)$ increases, all of the eigenvalues of the free modes become more positive, corresponding to an eastward shift in their position in the forced response (as in Equation 2.5). The Kelvin mode already has a positive eigenvalue for $U_o = 0$ so is already east of the substellar point. This eigenvalue becomes larger as U_o increases, so the Kelvin mode moves further east in the forced response. The maximum shift of the modes is to 90° east, no matter how large the eigenvalue becomes.

The Rossby modes of different orders m shift by different amounts. Tsai et al. (2014) shows that in a uniform background flow, the $n = 1$ Rossby mode is shifted eastwards towards 90° , producing a hot-spot shift (reproduced in Figure ??). In fact, Figure 2.2 shows that in this non-uniform flow $\bar{U}(y)$, the $n = 1$ Rossby mode eigenvalue becomes less negative but does not become positive for $U_o = 1.0$. This means that in the forced response it is shifted eastwards, but not far enough to pass the substellar point.

The higher order Rossby modes are shifted past the substellar point by the flow $\bar{U}(y)$, as shown by their positive eigenvalues for high enough flow speed U_o . However, the higher the order of a mode, the weaker its contribution to the forced response (Matsuno, 1966). The $n = 3$ and $n = 5$ symmetric Rossby modes are still important to the forced response, but any modes beyond this are less important.

Each mode also has its structure changed by the background shear flow. Figure 2.4 and 2.3 shows the lowest-order free solutions of Equation 2.7. These Kelvin and Rossby modes are slightly different to the free modes in zero background flow (Matsuno, 1966). The shear flow changes these solutions by adding higher order meridional structure, as discussed in more detail in Boyd (1978). In summary, the free modes generally respond to zonal flow in the same way as in the simpler system in Section 2.1, but vary in their structure and exact Doppler-shifts depending on the mode m .

2.2.2 Unstable Modes

Without damping, the eigenvalues of the free modes of this system come in pairs, with positive and negative imaginary parts. The modes with positive imaginary parts will grow unstably, similar to those in Wang and Mitchell (2014) or Ribstein et al. (2014). For non-zero damping, the imaginary parts will become more negative, making some free modes stable for large enough damping.

Technically, these unstable modes mean that any linear initial value problem in this system is not well posed, as it will eventually be dominated by the most unstable modes rather than the stationary response discussed elsewhere. However, the nonlinear shallow-water and GCM simulations shown here and in other chapters show that the linear stationary response still appears to dominate. This may mean that the unstable modes are strongly damped in reality, or equilibrate due to nonlinear effects. They could manifest as travelling waves in GCM simulations (Pierrehumbert and Hammond, 2018), or even correspond to the time-variable behaviour observed in some tidally locked planets (Armstrong et al., 2017)

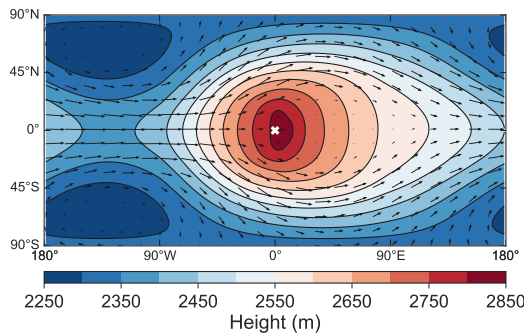


Figure 2.5: The time-mean height field from a simulation of a tidally locked planet in the model Exo-FMS, showing the typical eastward equatorial jet, shifted hot-spot, and night-side stationary Rossby waves.

2.3 Forced Response in Shear Flow on the Beta-Plane

In this section, I will discuss the effect of a background shear flow on the response to forcing in this linear model. Understanding this effect is the main aim of this chapter. I will show the forced solutions with and without a background shear flow, and compare them to GCM simulations. I will then discuss why the flow produces this circulation pattern, and why it reaches an equilibrium state.

Figure 2.5 shows a GCM simulation of a tidally locked planet, with the features typical to such atmospheres. This planet was chosen to be a general example of a terrestrial planet orbiting an M-dwarf, with radius R_E and orbital period 10 d. The semi-grey atmosphere is dry and composed of N_2 , with surface pressure 1 bar, and longwave optical thickness of 1. The general circulation pattern is not sensitive to these parameters, and its important large-scale features are present in most simulations of tidally locked planets, even very different ones like Hot Jupiters ([Heng and Showman, 2015](#)).

2.3.1 Response to Forcing

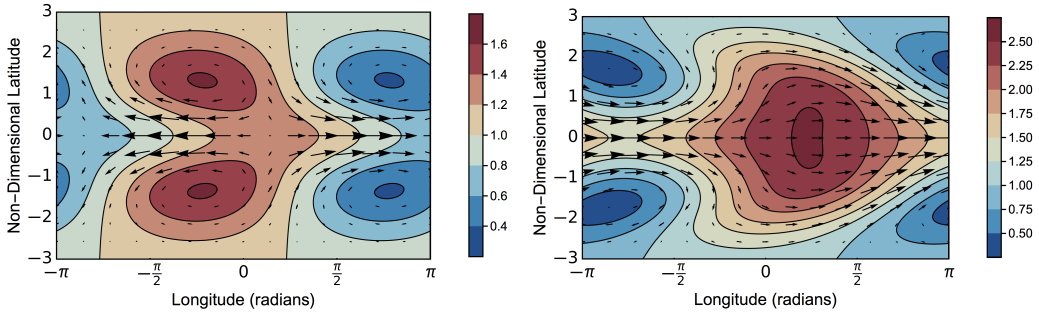
To find the stationary response to steady forcing of Equation 2.6, we set $Q(y) = Q_o e^{-y^2/2}$ ([Matsuno, 1966](#)) and $\partial/\partial t = 0$, giving the linear system of equations:

$$\begin{pmatrix} \alpha_{dyn} + ik_x \bar{U}(y) & \frac{\partial \bar{U}(y)}{\partial y} - y & ik_x \\ y & \alpha_{dyn} + ik_x \bar{U}(y) & \frac{\partial}{\partial y} \\ ik_x \bar{H}' & -y \bar{U}(y) + \bar{H}' \frac{\partial}{\partial y} & \alpha_{rad} + k_x \bar{U}(y) \end{pmatrix} \begin{pmatrix} u \\ v \\ h \end{pmatrix} = \begin{pmatrix} 0 \\ 0 \\ Q(y) \end{pmatrix}, \quad (2.9)$$

$$\bar{H}' = 1 + \bar{H}(y).$$

We approximate the eastward zonal flow as $\bar{U}(y) = U_0 e^{-y^2/2}$, and vary U_0 to show the effect of the strength of the flow. The equatorial Rossby radius of the planet sets the meridional scale of the beta-plane system. This means that this beta-plane solution is limited to planets where the equatorial Rossby radius is comparable to the planet size (which is not too inaccurate for many real tidally locked planets), and where it is also comparable to the jet width (which matches GCM simulations, and may be something of a requirement) ([Pierrehumbert and Hammond, 2018](#)). Despite this limitation, this system qualitatively matches the GCM simulations and predicts their scaling, while preserving the link to the intuitive, analytic forced solutions in [Matsuno \(1966\)](#).

I set the non-dimensional $\alpha = 0.2$, $Q_0 = 1.0$, and vary U_0 between 0 and 1. The background state $\bar{U}(y)$, $\bar{H}(y)$ is the same as in Section 2.3. Solving Equation 2.9 with the method described in Appendix B gives the u , v , and h fields that satisfy these equations. Figure 2.6 shows the effect of a background shear flow $\bar{U}(y)$ on the response to day-night forcing. This is the main result of this chapter, as it shows how the flow controls the global circulation pattern in GCM simulations like those in Figure 2.5. The first panel, Figure 2.6a, shows the response to forcing in zero background flow. This is exactly the same as the linear solutions in [Matsuno \(1966\)](#) and [Showman and Polvani \(2011\)](#), which were used in Chapter 1 to consider the initial acceleration of these atmospheres. This linear solution does not match the height field and velocities in Figure 2.5. In particular, the “hot-spot” and cold (low height)



(a) The forced solution with zero background flow. As the flow is zero, it is exactly the same $\bar{U}(y) = U_o e^{-y^2/2}$, $U_o = 1.0$.
(b) The forced solution with background flow. The eastward flow Doppler-shifts the maximum of the response eastwards, corresponding to the hot-spot shift seen in GCM simulations ([Tsai et al., 2014](#)).

Figure 2.6: The effect of a background shear flow $\bar{U}(y)$ on the forced solutions of Equation 2.9. The eastward flow Doppler-shifts the maximum of the response eastwards, corresponding to the hot-spot shift seen in GCM simulations ([Tsai et al., 2014](#)).

Rossby waves are in the wrong places.

Figure 2.6b shows the response to forcing in the shear background flow $\bar{U}(y)$ and background height $\bar{H}(y)$, which can be considered to be the “spun-up” state of the atmosphere. This qualitatively matches the GCM simulations in Figure 2.5, with the “hot-spot” shifted east and the cold Rossby waves in the right place.

I suggest that the solution in zero background flow in [Showman and Polvani \(2011\)](#) predicts the initial acceleration of the atmosphere, but after the jet forms the effect of the mean flow on the forced waves is vital to the equilibrium global circulation of the atmosphere. This is consistent with [Tsai et al. \(2014\)](#), which showed how a uniform background flow could Doppler-shift forced waves eastwards, producing a hot-spot shift.

2.3.2 Damping

The linear shallow-water model has several free parameters to choose. I discussed the choice of the forcing strength Q_o and jet speed U_o earlier. The strength of the radiative damping α_{rad} and the dynamical damping α_{dyn} are also free parameters,

which affect the magnitude and form of the response to forcing.

Previously, I showed that a very strong α_{rad} gives a response to forcing centred at the substellar point, but for reasonable radiative damping values the solution is similar to that in Figure 2.6. I assumed that α_{rad} and α_{dyn} were equal, which allows an analytic solution but is not physically justified.

The linear radiative damping has a realistic physical basis, but linear dynamical damping does not. It could be considered an approximation to effects like eddy viscosity, magnetohydrodynamic damping, or the effect of nonlinear terms (Heng and Workman, 2014). So, it is important to consider the situation with zero dynamical damping, to test if the explanation of this global circulation actually depends on an unphysical process.

Figure 2.7 shows the response to forcing of the same shallow-water system as that in Figure 2.6, but with zero dynamical damping α_{dyn} . The two panels show the same situations as in Figure 2.6. The first panel shows the solution in zero background flow, where the Kelvin response (the peak on the equator, in the previous plot) is now much weaker than the Rossby response (off the equator). This presents problems for the acceleration mechanism discussed in Chapter 1, but in the GCM and in the nonlinear shallow-water model in that chapter, there is always some Kelvin response – so the dynamical damping represents some process at work in these.

The second panel shows the response to forcing in the same shear background flow $\bar{U}(y) = U_0 e^{-y^2/2}$ as before. The solution has a similar form to that in Figure 2.6, and importantly has a similar maximum on the equator, showing that the lack of equatorial response in the first panel is not an issue when a jet has formed.

So the qualitative form of the forced solution and the argument that depends on it is not particularly dependent on the choice of the parameters α_{rad} and α_{dyn} . In particular, the dynamical damping α_{dyn} does not have a clear physical basis, but is not strictly necessary to include to match the GCM simulations – but, it is useful to

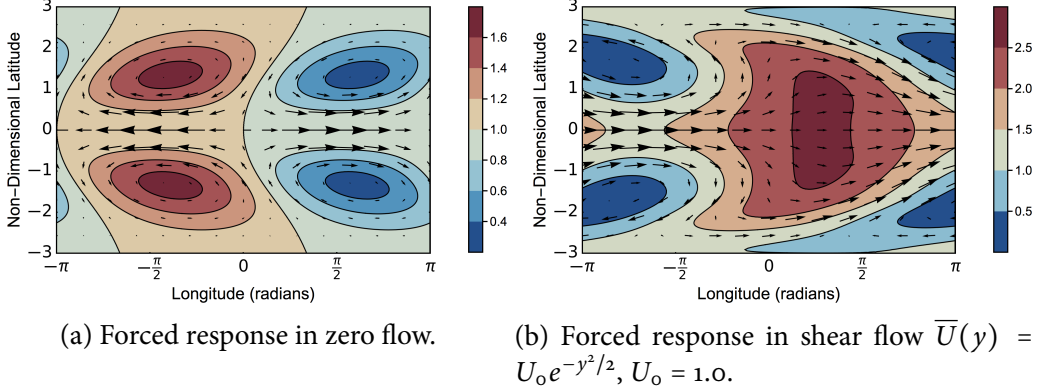


Figure 2.7: The forced response in zero background flow and a shear background flow, for dynamical damping $\alpha_{dyn} = 0$. These plots have the same form as those in Figure 2.6, showing that the dynamical damping is not critical.

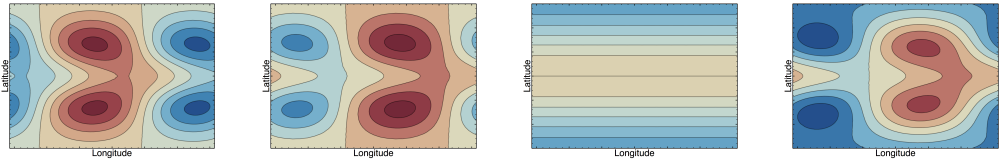
include for a simpler solution that is closer to the analytic result in [Matsuno \(1966\)](#).

2.3.3 Hot-Spot Shift

So far, I have shown that the response to forcing in a $\bar{U}(y)$ qualitatively matches a GCM simulation of a tidally locked planet. In this section, I will discuss why the flow has this effect on the response to forcing and the global circulation.

Figure 2.8 explains how the solution in a shear flow is built up from two main effects, using a simplified version of the solution in Figure 2.6. The first panel shows the response to forcing in zero flow, with the same solution as [Matsuno \(1966\)](#). The second panel shows the response to forcing in a uniform flow U_o (the same as the last panel of Figure 2.1). The Rossby and Kelvin modes have been shifted eastwards by the flow, as explained in Section 2.3 ([Tsai et al., 2014](#)). The third panel shows the zonally uniform height perturbation $\bar{H}(y)$ that geostrophically balances the zonal flow $\bar{U}(y)$. This is stronger at the equator, as it has the same form as the flow as explained in Section 2.3.1.

Then, the fourth panel shows the result of summing the second and third panels. East of the substellar point, the on-equator maximum and off-equator maxima



(a) Zero back- (b) Uniform back- (c) Height field $\bar{H}(y)$ (d) Sum of panels
ground flow, with no ground flow, with geostrophically bal- and (b), qualitatively
Doppler-shift. Doppler-shift. ancing the uniform matching the full so-
background flow \bar{U}_o . lution in Figure 2.6.

Figure 2.8: Height fields of various responses to forcing, showing how the sum of the Doppler-shifted height field and the height field due to the zonal jet produces the distinctive pattern in Figures 2.5 and 2.6.

combine to form a large, meridionally continuous “hot-spot”. West of the substellar point, the equatorial maximum and off-equator minima combine to increase the meridional height gradient, emphasising the off-equator cold Rossby lobes. Both of these features are in the same place as in the GCM simulations in Figure 2.5.

This combination of effects also explains the velocities in Figure 2.5. West of the substellar point, on the equator the Rossby wave velocities combine with the zonal flow to strengthen the jet there. East of the substellar point, the opposite Rossby wave velocities oppose the jet on the equator, leading to the region of small zonal flow west of the equator in Figure 2.5.

Understanding the cause of the hot-spot shift and day-night contrast in this way is vital to interpreting observations. Later in this chapter, I will use this simplified model to discuss how the observable features of the global circulation scale with planetary parameters such as rotation rate and temperature.

2.4 Wave Interactions with Shear Flow on a Sphere

The forced linear system on a beta-plane is useful for an intuitive understanding of the wave-mean flow interactions, as it is closely linked to the simple analytic

equatorial wave solutions of Matsuno (1966). The beta-plane is less useful for direct comparison with real planets or GCM simulations, as the assumption of a linear Coriolis parameter is inaccurate at high latitudes. It also does not directly represent the latitudinal direction or the effect of rotation rate, as the y-coordinate is non-dimensionalised to the equatorial Rossby radius. The system is therefore only appropriate for tidally locked planets where this radius is similar to the planetary radius.

In this section, I find the response to forcing for a shallow-water system in a spherical geometry. This represents the same physical system as the earlier beta-plane model, but can be directly compared to GCM simulations. The shallow-water equations on a sphere, linearised about a zonally uniform background flow $\bar{u}(\phi)$ and height $\bar{h}(\phi)$ are (Iga and Matsuda, 2005):

$$\begin{aligned}\frac{\partial u'}{\partial t} + \frac{\partial(\bar{u}u')}{a \cos \theta \partial \lambda} + v' \frac{\partial \bar{u}}{a \partial \theta} - \frac{\bar{u}v' \tan \theta}{a} &= 2\Omega v' \sin \theta - \frac{g \partial h'}{a \cos \theta \partial \lambda}, \\ \frac{\partial v'}{\partial t} + \frac{\partial(\bar{u}v')}{a \cos \theta \partial \lambda} + \frac{2\bar{u}u' \tan \theta}{a} &= -2\Omega u' \sin \theta - \frac{g \partial h'}{a \partial \theta}, \\ \frac{\partial h'}{\partial t} + v' \frac{\partial \bar{h}}{a \partial \theta} + \bar{u} \frac{\partial h'}{a \cos \theta \partial \lambda} + \bar{h} \nabla_H \cdot \mathbf{v}' &= F,\end{aligned}\quad (2.10)$$

where h is the height of the layer, $\mathbf{v} = (u, v)$ is the velocity, θ is latitude, λ is longitude, t is time, a is radius, g is gravity, and Ω is angular velocity. The forcing due to the day-night instellation is $F = F_0 \cos \theta \sin \lambda$. overlines denote zonal-mean quantities (the background flow and height \bar{u} and \bar{h}). Dashes denote perturbations to this background state.

The background state is stationary and in gradient wind balance, satisfying the meridional momentum equation in Equation 2.12:

$$\frac{1}{a} \frac{\partial}{\partial \theta} (\bar{h} + h_g) = - \left(2\Omega \bar{u} \sin \theta + \frac{\bar{u}^2}{a} \tan \theta \right). \quad (2.11)$$

The perturbed variables are wavelike in longitude and are uniformly damped, so

are proportional to $e^{im\lambda+\alpha t}$. All variables are made non-dimensional with velocity scale $2\Omega a$, height scale $(2\Omega a)^2/g$ and time scale $1/(2\Omega)$, and denoted as such by an asterisk. This gives the following non-dimensional shallow-water equations:

$$\begin{aligned}\alpha^* u_m^* + im \frac{\bar{u}^* u_m^*}{\cos \theta} + v_m^* \frac{\partial \bar{u}^*}{\partial \theta} - \bar{u}^* v_m^* \tan \theta &= v_m^* \sin \theta - \frac{im h_m^*}{\cos \theta}, \\ \alpha^* v_m^* + im \frac{\bar{u}^* v_m^*}{\cos \theta} + 2\bar{u}^* u_m^* \tan \theta &= -u_m^* \sin \theta - \frac{\partial h_m^*}{\partial \theta}, \\ \alpha^* h_m^* + im \bar{u}^* \frac{h_m^*}{\cos \theta} &= -\frac{\epsilon^*}{\cos \theta} \left[im u_m^* + \frac{\partial}{\partial \theta} (\cos \theta v_m^*) \right],\end{aligned}\quad (2.12)$$

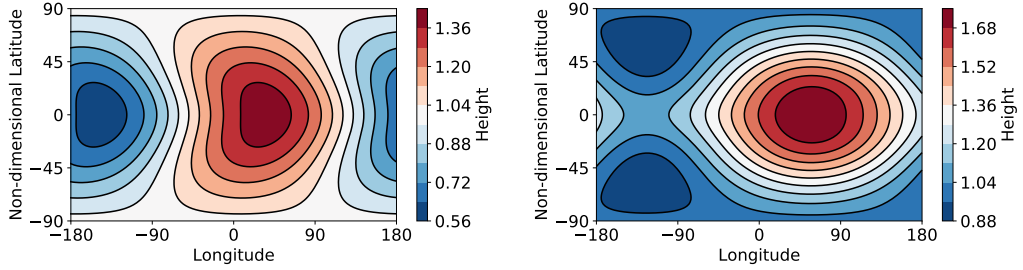
where $\epsilon \equiv (2\Omega a)^2/gH$ is Lamb's parameter, which in this system determines the relative effect of the rotation of the planet (Longuet-Higgins, 1968). This parameter was not present in the beta-plane system, where the effect of the rotation rate on the system was non-dimensionalised out by setting the meridional coordinate to the equatorial Rossby radius.

Appendix ?? shows how these coupled equations can be combined into the Laplace tidal equation, modified to include the effect of the background shear flow:

$$\frac{\partial^2 \phi_m^*}{\partial \mu^2} - B(\sigma^*, \mu) \frac{\partial \phi_m^*}{\partial \mu} - A(\sigma^*, \mu) \phi_m^* = \frac{F(\theta, x)}{i\sigma}, \quad (2.13)$$

where

$$\begin{aligned}A(\sigma^*, \mu) &\equiv \frac{1}{1 - \mu^2} \left[m(m+1) - m\mu \frac{1}{\Delta^*} \frac{\partial \Delta^*}{\partial \mu} + \epsilon \Delta^* \right. \\ &\quad \left. + \frac{m}{\Delta^* \hat{\sigma}^*} \left(f_1^* \frac{\partial \Delta^*}{\partial \mu} - \Delta^* \frac{\partial f_1^*}{\partial \mu} \right) \right], \\ B(\sigma^*, \mu) &\equiv \frac{1}{\Delta^*} \frac{\partial \Delta^*}{\partial \mu} + \frac{2\mu(m+1)}{(1 - \mu^2)}, \\ \Delta^* &\equiv f_1^* \bar{\zeta}^* - \hat{\sigma}^{*2}.\end{aligned}\quad (2.14)$$



(a) The forced solution with zero background flow, corresponding to a spherical version of $U_o \exp(-\mu^2/L_{jet}) \cos \theta$, $U_o = 0.75$, matching the solution in Matsuno (1966).
(b) The forced solution with background flow, corresponding to a spherical version of $U_o \exp(-\mu^2/L_{jet}) \cos \theta$, $U_o = 0.75$, matching the form of the GCM simulations in Figure 2.5.

Figure 2.9: The effect of a background shear flow $\bar{U}(\phi)$ on the forced solutions of Equation 2.12, matching the form of the beta-plane solutions in Figure 2.6.

2.4.1 Solution to the Forced Tidal Equations

Equation 2.13 is solved with the Chebyshev pseudo-spectral collocation method outlined in Wang et al. (2016) for the eigenfunctions of Laplace's tidal equation on a sphere (Longuet-Higgins, 1968) (see Appendix ?? for details).

The free parameters of the system are the forcing strength F_o , damping rate α , rotation rate Ω , radius a , gravity g , background height H_o . The background flow is set by the jet speed U_o and jet width L_{jet} , for a flow profile $U_o \exp(-\mu^2/L_{jet}) \cos \theta$. The default parameters of $F_o = 0.3$, $\alpha = 0.6$, $\Omega = 1.0$, $a = 1.0$, $g = 2.0$ and $H_o = 1.0$ were based on the GCM simulation in Figure 2.5, and rounded off for simplicity. The default jet parameters were $U_o = 0.75$, and $L_{jet} = \sqrt{3}$.

Figure 2.9 shows the effect of a background zonal flow \bar{u} on the response to day-night forcing in a spherical geometry. Just as in Figure 2.6 for the beta-plane, the background flow Doppler-shifts the maximum of the wave response eastwards and adds a zonally uniform height perturbation centred on the equator. The forced response is again qualitatively similar to the example GCM results in Figure 2.5.

2.5 Scaling Relations

The shallow-water models in this chapter have two main uses. First, to explain the mechanism producing the global circulation pattern seen in GCM simulations and observations. Second, to predict how this circulation will scale with various planetary parameters. [Komacek and Showman \(2016\)](#) and [Zhang and Showman \(2017\)](#) used simple 1D scaling relations based on a balance of advective and radiative timescales on the equator to predict how observables such as hot-spot shift and day-night contrast scale with planetary parameters. In this section, I will show more detailed scaling relations using the shallow-water model including important wave effects can explain the behaviour of GCM simulations and observations.

2.5.1 1D Scaling Relations

The 2D shallow-water system on a sphere has no analytic solution that gives a simple prediction of how the observables like the hot-spot shift and day-night contrast scale with planetary parameters. Reducing it to a 1D system on the equator gives an analytically solvable system, which behaves like the full 2D system to lowest order. Setting $\phi = 0$ and retaining only the damping and advection terms, the third line of Equation 2.6

$$\frac{\partial H' u}{\partial x} + H' \frac{\partial v}{\partial y} - y \bar{U}(y) v + \frac{\partial \bar{h}}{\partial t} + \alpha h + \frac{\partial \bar{U}(y) h}{\partial x} = Q_0 e^{-y^2/2}, \quad (2.15)$$

becomes

$$\frac{\partial \bar{h}}{\partial t} + \alpha h + \frac{\partial U_0 h}{\partial x} = Q_0. \quad (2.16)$$

Then to find the stationary wave-1 response, we set $\partial/\partial t = 0$ and $\partial/\partial x = ik_x$:

$$-\alpha h(y=0) + ik_x U_o h(y=0) = Q_o. \quad (2.17)$$

So the on-equator height perturbation $h(x, y=0) = h(y=0)e^{ik_x x}$ is:

$$h(x, y=0) = \frac{Q_o}{\alpha^2 + k_x^2 U_o^2} (-\alpha \cos(k_x x) + k_x U_o \sin k_x x). \quad (2.18)$$

This is a sinusoidal height perturbation on the equator, with magnitude

$$h_o = \frac{\alpha + k_x U_o}{\alpha^2 + k_x^2 U_o^2} Q_o. \quad (2.19)$$

The hot-spot shift x_o is at the maximum of this sinusoidal curve, where $\partial h / \partial x = 0$:

$$x_o = \frac{1}{k_x} \tan^{-1}(k_x \frac{U_o}{\alpha}) \quad (2.20)$$

This is the same as the simplest approximation of the hot-spot shift calculated by [Zhang and Showman \(2017\)](#), $\lambda_s = \tan^{-1}(\frac{\tau_{rad}}{\tau_{adv}})$, (where τ_{rad} corresponds to $1/\alpha$ and τ_{adv} corresponds to k_x/U_o).

Equation 2.20 predicts that the hot-spot shift varies between 0° and 90° east of the substellar point. There are two similar ways to interpret this physically. First, the size of the shift can be seen as a balance between the jet transporting heat eastwards according to the advective timescale τ_{adv} , and the heat radiating away according to the radiative timescale τ_{rad} ([Komacek and Showman, 2016; Zhang and Showman, 2017; Hammond and Pierrehumbert, 2017](#)). Or, as discussed above, they can instead be seen as a balance of the flow U_o shifting the stationary waves 90° out of phase with the forcing, versus the damping α_{rad} bringing them in phase with the forcing ([Tsai et al., 2014; Hammond and Pierrehumbert, 2018](#)). Section 2.6.1 discusses these two mechanisms in more detail.

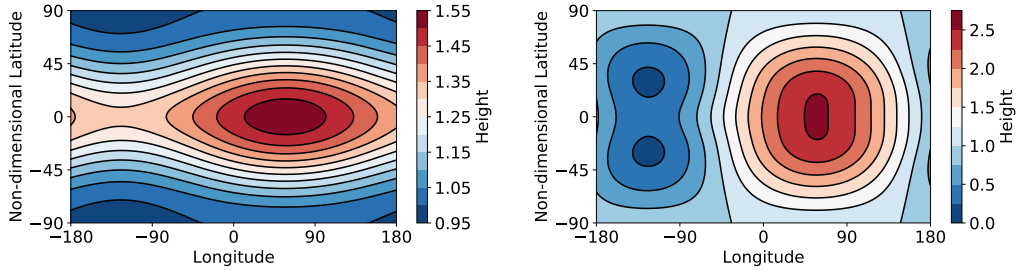
2.5.2 2D Scaling Relations

In this section, I will show how the forcing strength, damping rate, and rotation rate affect the global circulation in the linear shallow-water model on a sphere. In the next section, I will show how this qualitatively explains the global circulation of a suite of GCM tests.

Figure 2.10 shows the effect of varying the forcing magnitude F_o in a system with all other parameters the same as those in Figure 2.9b. The case with low F_o has a weaker wave-1 height field due to the day-night forcing than its zonally uniform height field due to the jet. So, the global height field is very zonally uniform. In contrast, the case with high F_o has a much stronger wave-1 height field so varies greatly with longitude. Note that the hot-spot shifts (the longitude of the maximum response) are the same in both cases, as the Doppler-shift is not affected. The thermally emitted phase curve of the second case would have a much larger magnitude than the first, and their phase shifts would be the same.

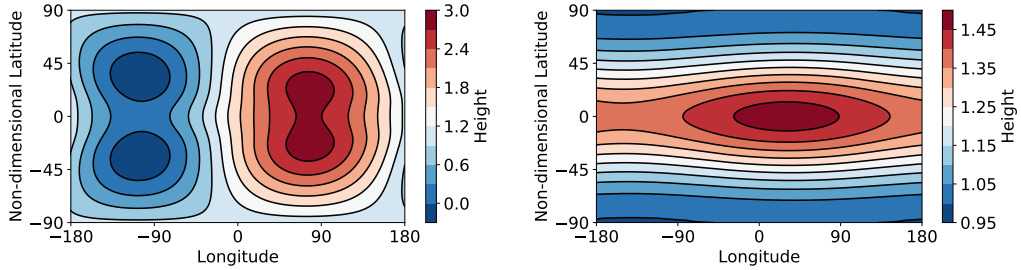
Figure 2.11 shows the effect of varying the damping rate α in a system with all other parameters the same as those in Figure 2.9b. The case with low damping is similar to the case with high forcing, as it also increases the strength of the wave-1 field relative to the zonally uniform field. The case with high damping has a weak wave-1 response, and also has a smaller hot-spot shift as the high damping rate brings the maximum more in phase with the forcing, as discussed previously. The weakly damped case would have a phase curve with a large amplitude and large phase shift, while the strongly damped case would have a small amplitude and a small phase shift.

Figure 2.12 shows the effect of the rotation rate Ω . The main effect of Ω is to scale the magnitude of the zonally uniform height perturbation due to the jet, due to the f dependence in Equation 2.11. This means that Ω has the same leading-order effect as F_o , scaling the magnitude of the zonally uniform height perturbation relative to the



- (a) Low forcing, $F_o = 0.1$, giving a weak wave-1 component and a more zonally uniform field.
(b) High $F_o = 1.0$, giving a strong wave-1 component and a less zonally uniform field.

Figure 2.10: Spherical solutions with low and high forcing F_o , showing how this affects the strength of the wave-1 component relative to the unchanged wave-0 jet component, affecting the longitudinal variation and day-night contrast.



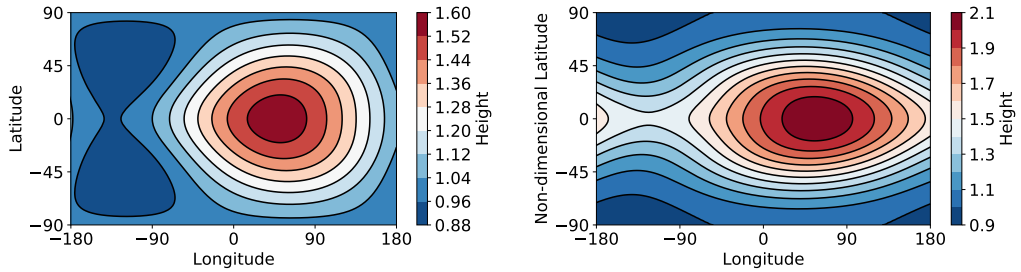
- (a) Low damping $\alpha = 0.2$, giving a strong wave-1 component and a large hot-spot shift.
(b) High damping $\alpha = 2.0$, giving a weak wave-1 component and a smaller hot-spot shift.

Figure 2.11: Spherical solutions with low and high damping α , showing how this affects the strength of the wave-1 component and also the magnitude of the Doppler-shift of the wave components.

wave-1 forced response. The case with low Ω would have a phase curve with a large amplitude and large phase shift, while the case with high Ω would have a smaller amplitude.

2.5.3 GCM Scaling Relations

These shallow-water solutions predict how the GCM should respond to changes in its input parameters. Figure 2.13 shows a suite of tests in Exo-FMS, of a tidally locked planet with the same parameters as that in Figure 2.5, but with variable instel-



(a) Low rotation rate Ω , giving a weak wave-o component and a large day-night contrast. (b) High rotation rate Ω , giving a strong wave-o component and a small day-night contrast.

Figure 2.12: Spherical solutions with low and high rotation rate Ω , showing how this affects the magnitude of the wave-o height perturbation $\bar{H}(\phi)$ balancing the imposed shear flow $\bar{U}(\phi)$.

lation and rotation rate. The instillation corresponds to the forcing strength in the shallow-water model. The instillation in the GCM also indirectly affects the radiative damping rate via the atmospheric equilibrium temperature.

The effect of forcing, damping, and rotation rate shown in Section 2.5 for the shallow-water model can also be seen in these tests. The hotter tests are more strongly forced, and have larger day-night temperature differences. The colder tests are more zonally uniform, as their jets dominate the global height field. The more rapidly rotating tests are also more zonally uniform, as this increases the height perturbation needed to balance the jet. This is especially clear in the “cold” tests, where the more rapidly rotating tests are very zonally uniform.

The effect of damping can also be seen in the tests. In the shallow-water model, an increased damping rate gave a smaller hot-spot shift as it brought the wave response into phase with the forcing. In the GCM, the colder tests have a low damping rate so all have hot-spots shifted further east. The hotter tests have faster damping rates so have less shifted hot-spots – this is especially clear in the 2 day cases, where the hottest test has almost no hot-spot shift. The effect of damping is shown directly in Chapter 3, where varying the mean molecular weight of the atmosphere affects the

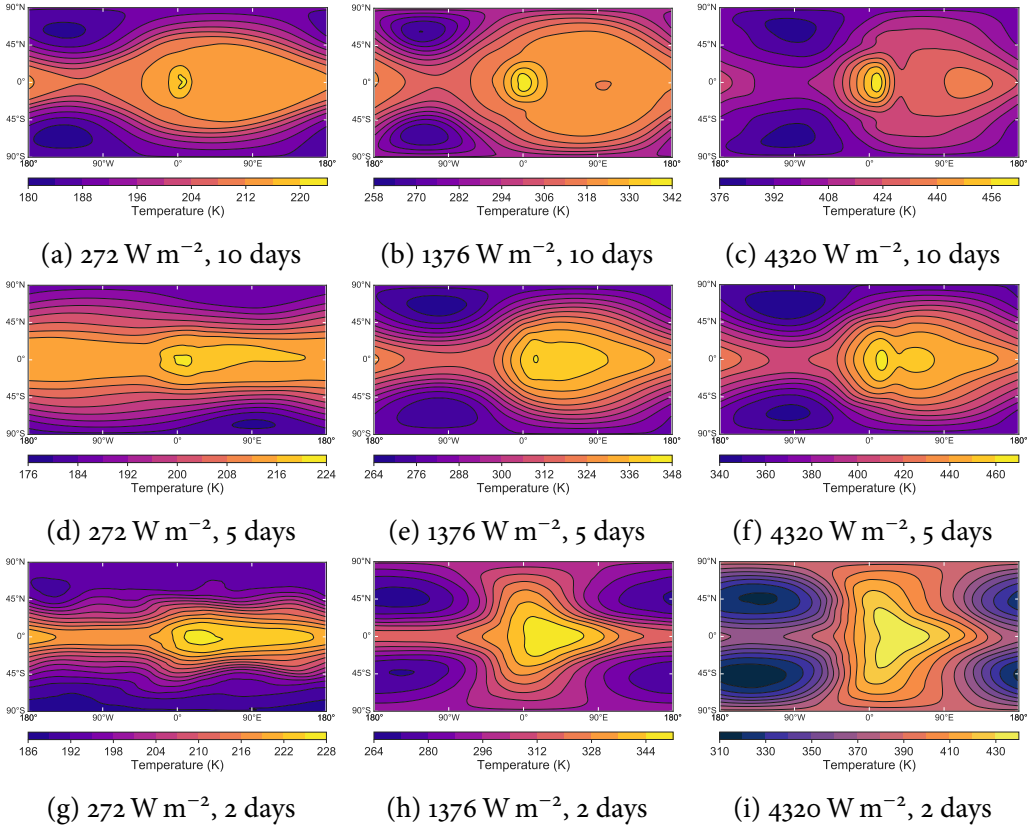


Figure 2.13: The temperature at the 500 mbar level from a suite of tests in the GCM Exo-FMS, with different rotation periods and instellations (Pierrehumbert and Hammond, 2018). All other parameters are the same as those in Figure 2.5.

damping rate without changing the forcing strength (instellation affects both, so its effect is more complicated).

2.6 Discussion

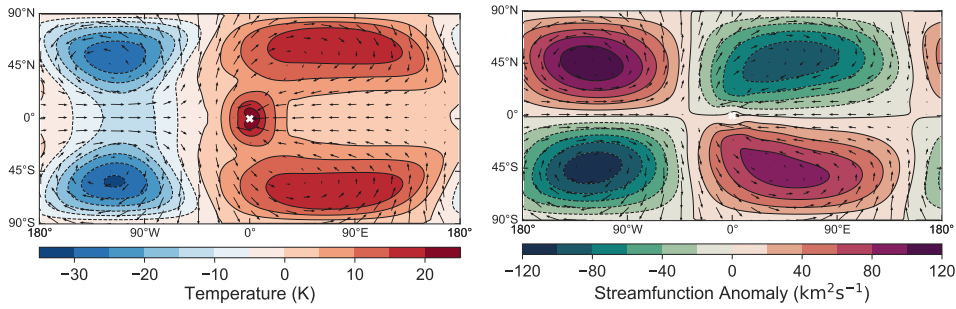
2.6.1 Hot-Spot Shift Mechanism

In Section 2.5.1, I showed how the hot-spot shift can be either seen as due to advection of heat by the equatorial jet, or as a Doppler-shift of the stationary waves excited by the day-night forcing. These mechanisms are similar at some level, giving the same basic scaling behaviour on the equator as shown previously. However, they

are physically different ideas and should have different effects. For example, if advection by the jet produces the shift then the temperature and tracer fields in GCM simulations should be closely coupled. But, if the temperature field is instead set by the stationary wave pattern, it could be very different to the distribution of tracers advected by the flow. Chapter 4 discusses this difference in the context of cloud simulations.

This chapter suggests that the Doppler-shift of the waves is the mechanism in most GCM simulations, as it explains the global temperature and velocity distribution so well. Figure 2.14 shows eddy fields (with their zonal means subtracted) from a GCM simulation of a tidally locked planet. This leaves behind the dominant wave-1 component forced by the day-night heating. Comparing Figure 2.14 with Figure 2.8 or Figure 2.9 shows how the wave solutions exactly match the GCM results. The cold, anticlockwise Rossby waves are shifted to -90° in the GCM, matching the shifted pattern in Figure 2.8b rather than the non-shifted pattern in Figure 2.8a. The wave-based mechanism also explains the weak zonal flow east of the substellar point in the GCM simulation in Figure 2.5 – the mean eastward zonal jet cancels with the local westward flow due to the waves shown in Figure 2.14

This Doppler-shift mechanism was first put forward by [Tsai et al. \(2014\)](#) for tidally locked planets, and its combination with the shear flow and height perturbation in this chapter appears to match the circulation seen in GCM simulations. Advection of heat by the jet will still have some effect on the circulation, but the wave-based picture matches the circulation well enough that any advection effects appear to be minor. I have compared the shallow model to a small number of GCM simulations, but very similar flow and wave patterns are seen in other studies of a variety of planets ([Charnay et al., 2015](#); [Heng and Showman, 2015](#); [Kataria et al., 2014](#); [?](#); [Boutle et al., 2017](#)).



(a) Eddy temperature and velocities.

(b) Eddy streamfunction and velocities.

Figure 2.14: The time-mean eddy temperature, velocity, and streamfunction fields on the half-surface pressure level of the GCM simulation shown in Figure 2.5.

2.6.2 Comparing Predictions to Observations

A compelling result of studying GFD on exoplanets is the possibility of plotting trends in atmospheric behaviour for classes of planet, in a way that is not possible with the individual data points of disparate Solar System planets. This makes it possible to test scaling relations such as those in this chapter, or in studies such as [Komacek et al. \(2017\)](#) and [Zhang and Showman \(2017\)](#). In this section, I compare the scaling relations from the linear shallow-water model in Section 2.5 to observed trends in day-night contrast and hot-spot shift for Hot Jupiters with different equilibrium temperatures.

Figure 2.15a shows that the fractional day-night contrast $A = (T_{day} - T_{night})/T_{day}$ increases with planetary equilibrium temperature. This is consistent with the discussion in Section 2.5.2, which shows in Figure 2.10 how increased forcing gives a stronger wave-1 response than the wave-0 jet height field, giving a larger day-night contrast. The damping rate will also increase at higher temperatures, which is predicted by Figure 2.11 to decrease the day-night contrast, but this effect appears to be weaker than the effect of the forcing. The observations are also consistent with the scaling behaviour of the GCM simulations in Figure 2.13, where increased forcing gives an increased day-night contrast. [Komacek et al. \(2017\)](#) explained this trend

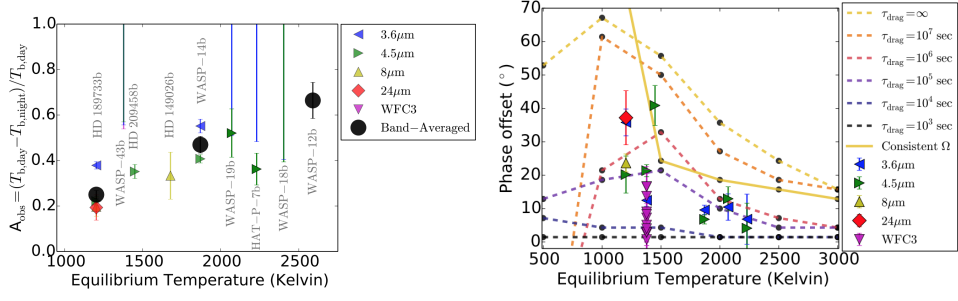
with a balance of radiative versus advective timescales, using a different mechanism to the wave-based approach in this chapter, as discussed in the previous section.

Figure 2.15b shows an observed decrease in hot-spot shift with increasing equilibrium temperature. This is consistent with Section 2.5.2, which predicts no effect on hot-spot shift from increased forcing, but a decreased hot-spot shift at higher temperatures due to increased radiative damping. It is also consistent with the GCM simulations in Figure 2.13, where the tests with higher temperature had smaller hot-spot shifts. Komacek et al. (2017) explained this trend as an increased damping rate giving a smaller shift as it dominates the heat transport via advection. This chapter instead explains the trend as due to the increased damping moving the stationary wave response into phase with the forcing, due to Equation 2.5.

As the number and quality of these observations increase, it will become possible to test theories of global circulation in more detail. The richness of possible behaviour due to variations in the atmospheric dynamics alone makes them vital to understand. Many mechanisms such as cloud formation, recombination of molecules, and magnetic effects have been invoked to explain observations of these planets. While this will be important in many cases, I suggest that much of the scaling behaviour will be explained by the variable dynamical behaviour of the atmospheres.

2.7 Conclusion

In this chapter, I have shown how the zonal jets discussed in Chapter 1 produce the hot-spot shift and global circulation pattern in the atmospheres of tidally locked planets. Using a shallow-water model linearised about a meridionally varying equatorial jet $\bar{U}(y)$, I showed how the flow Doppler-shifts the stationary waves excited by the day-night forcing. These combine with the zonally uniform velocity and height field of the jet, to give the distinctive pattern seen in GCM simulations.



(a) Observed day-night contrast versus planetary equilibrium temperature. (b) Observed hot-spot shift versus planetary equilibrium temperature.

Figure 2.15: Observed day-night contrast and hot-spot shift versus planetary equilibrium temperature showing an increased contrast and decreased shift at higher temperatures, from [Komacek et al. \(2017\)](#).

Varying the parameters of this model shows how the global circulation and temperature distribution scales with planetary parameters. This predicts scaling relations for observables, such as day-night temperature contrast increasing with temperature, and hot-spot shift decreasing with temperature. I showed how these predictions match GCM simulations and observations. These predictions are similar to the advection-based scaling. [Komacek et al. \(2017\)](#) and [Zhang and Showman \(2017\)](#), but have a different physical mechanism. I suggest that the wave-based mechanism is a more accurate description of the global circulation and hot-spot shift.

Further work could refine the linear model to predict the equilibrium circulation states of tidally locked planets, by using the ideas about zonal flow and acceleration in Chapter 1 to find equilibrium states. It would also be useful to consider the free modes of the linear system, and to relate these to the time-varying behaviour seen in GCM simulations ([Pierrehumbert and Hammond, 2018](#)) and observations ([Armstrong et al., 2017](#)) of tidally locked planets. We calculated the free modes of the beta-plane model in a shear flow, and found some unstable modes when the shear was strong enough, which could correspond to this variability.

In this chapter, I showed how on a tidally locked planet, the interaction between

the equatorial jet and the stationary waves excited by the instellation forms the global circulation pattern. The rest of this thesis will discuss models of the tidally locked planet 55 Cancri e, using the ideas about global circulation developed in the chapters so far.

CHAPTER 3

Linking the Climate and Thermal Phase Curve of 55 Cancri e

The first phase curve of a terrestrial planet was measured by [Demory et al. \(2016\)](#) using Spitzer observations of the “lava planet” 55 Cancri e, following the measurement of transits in the visible ([Winn et al., 2011a](#)) and infrared ([Demory et al., 2011](#)). This presented the first observation directly linked to the global circulation of a terrestrial planet outside our solar system. It provides an opportunity to test the theories and simulations of the atmospheric circulation of a tidally locked planet that have been shown previously in this thesis.

In particular, this chapter addresses the question of whether the features of the observed phase curve can be explained by the presence of an atmosphere. I will use the GCM Exo-FMS to model a range of possible atmospheres, testing analytic predictions of the global circulation in order to interpret the phase curve. The main aim is to test whether an idealised atmosphere with the correct bulk properties is consistent with the phase curve. This chapter builds on the results of studies such as [Cowan and Agol \(2011\)](#), [Menou \(2012\)](#), [Komacek and Showman \(2016\)](#), and [Zhang and Showman \(2017\)](#), which explored the effect of atmospheric parameters like temperature and surface pressure, on the observable global circulation of tidally locked

planets.

Section 3.1 discusses observations of 55 Cancri e to date, particularly the thermal phase curve that this chapter is based on (Demory et al., 2016). Section 3.2 discusses the general circulation of tidally locked planets, and scaling relations from Zhang and Showman (2017) that will be used to interpret the phase curve and GCM simulations.

In Section 3.3, I discuss the GCM Exo-FMS that I will use to simulate 55 Cancri e and produce phase curves. Section 3.4 shows the results of these simulations, focusing on their global temperature distributions and vertical structure. Section 3.5 shows simulated observations of 55 Cancri e produced from the GCM simulations, and compares their phase curves to the real phase curve measured by Demory et al. (2016) to draw conclusions about the planet and its atmosphere. Section 3.6 discusses the constraints that this modelling can place on the likely atmospheric composition of this planet.

The model atmosphere that fitted the observations best has a surface pressure of 5 bar and a mean molecular weight of 4.6 g mol^{-1} . The simulations constrained the atmospheric properties, showing clearly how it could not match the phase curve outside a certain parameter space. The simulations and scaling relations suggested that an N_2 atmosphere, or one with a low surface pressure, would not have as large a hot-spot shift as the observed phase curve. They also suggested that an H_2 atmosphere, or one with a high surface pressure, would not have as large a day-night contrast as the observed phase curve. Both of these results suggest the intermediate molecular weight and surface pressure of the best-fit atmosphere.

The thermal phase curve estimated from the best-fit atmosphere still did not match the observed phase curve exactly. In particular, this atmosphere matched the observed 41° hot-spot shift, but under-predicted the observed 1300 K day-night contrast. Diagnostic estimates of cloud formation suggested that the night-side could be cold enough for SiO clouds to form high on the night-side, reducing the bright-

ness temperature there and better matching the observations. This was a very rough estimate, which I will follow up with more detailed modelling in Chapter 4.

This chapter shows that an atmosphere could explain the observed phase curve of 55 Cancri e, if some process lowers the brightness temperature of the night-side compared to the simulations. The conclusion about the likely range of properties for an atmosphere on 55 Cancri e depends on the accuracy of the observations, highlighting the need for accurate measurements of a variety of planets to test these ideas in the future.

3.1 Observations of 55 Cancri e

In this section I will discuss observations of the planet 55 Cancri e, and its possible atmospheric states and composition. I will focus on the thermal phase curve observed by [Demory et al. \(2016\)](#), and introduce theoretical scaling relations used to explain exoplanet phase curves in general.

55 Cancri e

55 Cancri e is a “lava planet”, a rocky super-Earth with radius $1.875 R_E$ orbiting close to its host star 55 Cancri A. It is expected to be tidally locked due to its proximity to its star ([Pierrehumbert and Hammond, 2018](#)), which is supported by the large day-night contrast shown by its thermal phase curve ([Demory et al., 2016](#)).

Transits of 55 Cancri e in the visible ([Winn et al., 2011a](#)) and infrared ([Demory et al., 2011](#)) presented the possibility of characterising the planet. 55 Cancri e is particularly amenable to observations for a terrestrial planet, given its high equilibrium temperature of about 2500 K and large radius which give a particularly high signal to noise ratio ([Tinetti et al., 2016](#)).

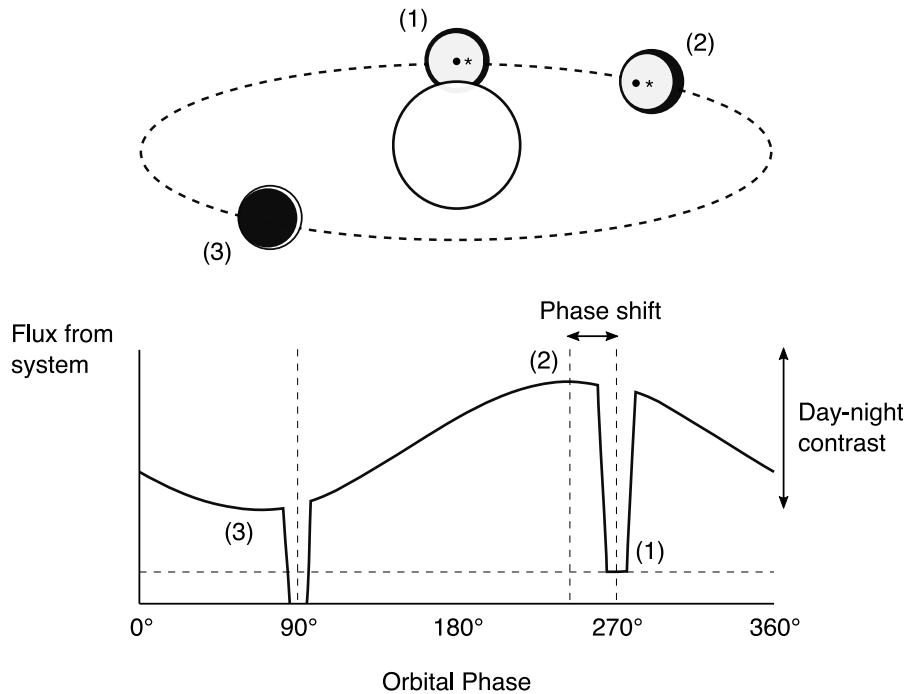


Figure 3.1: A schematic of the phase curve observed of the flux from a planet as it orbits its star. Position (1) is the secondary eclipse, (2) is the phase of the maximum thermal emission, and (3) is the primary eclipse.

Thermal phase curve

This chapter is concerned with interpreting the thermal phase curve of 55 Cancri e measured by [Demory et al. \(2016\)](#). A phase curve is a measurement of the flux from a planet and the star it orbits, over one orbital period (or averaged over many orbital periods). The magnitude of the thermal flux corresponds to the brightness temperature, which depends on the atmospheric temperature structure and its longwave optical properties.

Figure 3.1 shows an idealised thermal phase curve measured from a tidally locked planet, and highlights the key features. At 90° , the planet passes in front of the star for its transit, or “primary eclipse”, causing a large dip in flux from the system. At 270° , the planet passes behind the star for its “secondary eclipse”, causing a small dip in flux. The flux above $F/F_S = 1$ is due to the planet, and is approximately sinusoidal

because the temperature of the planet varies in this way with longitude, as the day-side is heated and the night-side is not. The difference in thermal emission between the maximum and minimum of the planet's flux gives the difference in brightness temperature between the day-side and the night-side – marked on Figure 3.1 as the “day-night contrast”.

The final key feature is the offset between the peak of the thermal emission, and the position of the secondary eclipse. This occurs when the hottest hemisphere of the planet is not centered on the substellar point. Position (1) in Figure 3.1 is the secondary eclipse, when the observer looks directly at the substellar point (or would, if the star was not in the way). On a bare rock planet, the substellar point (marked by a dot) and the centre of the hottest hemisphere (marked by an asterisk) would be the same, and there would be no phase offset.

If a process redistributes heat around the planet, the hottest hemisphere does not have to coincide with the substellar point. Chapter 2 shows how an atmosphere on a tidally locked planet has a hot-spot shifted east of the substellar point. Figure 3.1 shows how the observer looks directly at this eastward shifted hot-spot (at position (2)) before the secondary eclipse (position (1)). So, the maximum flux is measured before the secondary eclipse, and the difference in orbital phase between these two points gives the longitudinal offset between the substellar point and the hottest part of the planet (or just the “hot-spot”).

Phase curves at optical wavelengths give similar information about the albedo of the planet, showing how features such as clouds affect the reflection of stellar light from the planet at different locations ([Parmentier et al., 2016](#)). [Dragomir et al. \(2012\)](#) measured an optical phase curve for 55 Cancri with a similar form to the thermal phase curve in [Demory et al. \(2016\)](#). This raised the possibility that the reflectance and emission are coupled in some way, such as by temperature-dependent clouds.

Figure 3.2 shows the thermal phase curve measured by [Demory et al. \(2016\)](#) in the

$4.5\text{ }\mu\text{m}$ channel of the Spitzer Space Telescope Infrared Array Camera (IRAC). The phase curve has a hot-spot shift of 41° , a day-side temperature of (2700 ± 270) K, and a night-side temperature of (1380 ± 400) K. Figure 3.3 shows maps of brightness temperature reconstructed from the phase curve.

The combination of this large hot-spot shift and large day-night temperature contrast presents a puzzle. In 1D analytic models of circulation on tidally locked planets like those in [Zhang and Showman \(2017\)](#), a large hot-spot shift implies a high efficiency of heat redistribution. But, a large day-night contrast implies a low efficiency of heat redistribution. So, the solutions of [Zhang and Showman \(2017\)](#) cannot fit both of these results at the same time, and the GCM simulations below will not be able to fit both results either.

[Angelo and Hu \(2017\)](#) reanalysed the phase curve and suggested a hot-spot shift of 34° , a day-side temperature of (2700 ± 160) K, and a night-side temperature of (1600 ± 140) K. These estimates are both smaller than those of [Demory et al. \(2016\)](#), although are still within error of each other. They are also more consistent with the GCM simulations in this chapter and the predictions of [Zhang and Showman \(2017\)](#), as the smaller hot-spot shift and day-night contrast require a less extreme atmospheric circulation. This chapter focuses on the analysis of [Demory et al. \(2016\)](#) as the work of [Angelo and Hu \(2017\)](#) was only available after this work was done.

Atmosphere

It is not clear what sort of atmosphere, if any, to expect on a planet like 55 Cancri e. A low molecular weight atmosphere like a Hot Jupiter seems unlikely, given the planet's proximity to its star and correspondingly high temperatures and high-energy radiation, which would cause atmospheric escape of lighter components ([Demory et al., 2016](#)). [Gillon et al. \(2012\)](#) used the observational mass and radius to suggest that there is an atmosphere composed of high molecular weight volatiles.

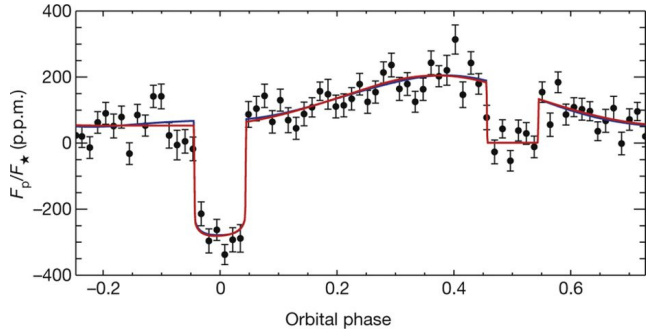


Figure 3.2: The thermal phase curve observed at $4.5 \mu\text{m}$ by Demory et al. (2016), showing an offset of the maximum flux from the secondary eclipse, corresponding to a hot-spot shift.

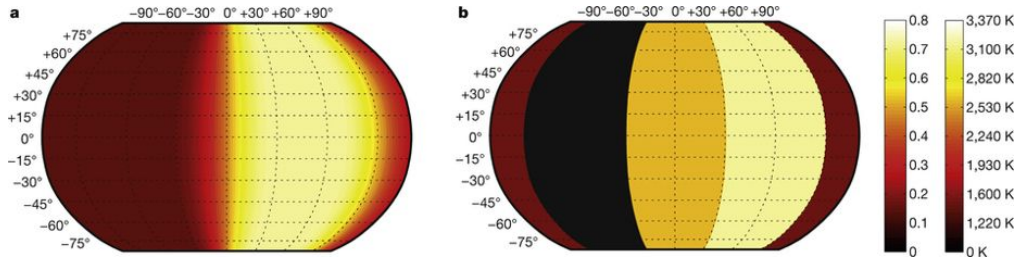


Figure 3.3: The temperature map reconstructed by Demory et al. (2016) from the phase curve in Figure 3.2, showing a hot-spot shift of 41° , a day-side temperature of $(2700 \pm 270) \text{ K}$, and a night-side temperature of $(1380 \pm 400) \text{ K}$.

Tsiaras et al. (2016) reported the detection of an atmosphere due to spectroscopic deviations from a bare-rock planet, using observations in the near-infrared with the WFC3 camera of the Hubble Space Telescope (HST). In this chapter, I avoid direct questions of atmospheric composition or origin, focusing on what bulk properties – surface pressure, mean molecular weight, and longwave optical thickness – could be consistent with the observed thermal phase curve.

Atmospheric Circulation

This chapter aims to simulate possible atmospheres on 55 Cancri e to test if the thermal phase curve observations – particularly the hot-spot shift and day-night contrast – are consistent with an atmosphere circulating heat around the planet. Other studies have simulated Hot Jupiters in this way, to analyse similar thermal

phase curves with hot-spot shifts and day-night contrasts (Showman et al., 2015) (Mayne et al., 2017). Hot Jupiters have radii and atmospheres comparable to Jupiter, but temperatures of about 1000 to 3000 K. These simulations have proved very useful in understanding their global circulation and behaviour at different temperatures, so it is a natural next step to apply them to observations of a terrestrial planet.

Zhang and Showman (2017) suggested scaling relations to predict how the observable hot-spot shift and day-night contrast depend on the planetary parameters. I will use these to predict a likely parameter space that could fit the observations, and to analyse the GCM simulations. In Chapter 2, I show how some of the scaling relations are identical to the shallow-water scaling relations derived in that chapter for the equator of a tidally locked planet. Komacek and Showman (2016) tested similar scaling relations against a suite of simulations of Hot Jupiters, and found the relatively simple predictions to be consistent with the behaviour of the GCM. This is encouraging for the use of similar simple theory in this chapter, alongside simulations of a different sort of tidally locked planet.

3.2 Simplified Scaling Theory

To understand the relation between the atmospheric properties and the observed phase curve, we used scaling relations from the idealised 1D atmospheric models of Zhang and Showman (2017). These predict the effect of the bulk properties of the atmosphere on the main features of the phase curve – the hot-spot shift and day-night contrast. In this section, I will describe these scaling relations and show how we used them to select a parameter space that could be consistent with the observed phase curve. They will be used in Section 3.3 to choose a suite of GCM tests to compare to the phase curve.

3.2.1 1D Model

Zhang and Showman (2017) reduce the primitive equations to a 1D differential equation on the equator where heat transport is determined by a balance of the radiative timescale and advective timescale (Komacek and Showman, 2016). The resulting scaling relations are the same as those derived differently from the shallow-water system in Chapter 2.

The important timescales in the relations used in this chapter are the radiative timescale τ_{rad} , the wave timescale τ_{wave} , and the advective timescale τ_{adv} . The radiative timescale is the typical timescale of changes due to radiative forcing:

$$\tau_{\text{rad}} \sim \frac{p_{\tau=1}}{\mu g} \frac{c_p}{4\sigma T^3}, \quad (3.1)$$

where $p_{\tau=1}$ pressure at which the optical thickness is unity, μ is the mean molecular weight, T is the equilibrium temperature of the planet, c_p is the atmospheric molar heat capacity.

The wave timescale is the timescale for the planetary-scale equatorial waves to propagate horizontally:

$$\tau_{\text{wave}} = L/NH, \quad (3.2)$$

where L is the radius of the planet, N is the buoyancy frequency of the atmosphere, and H is the atmospheric scale height. The advective timescale is the time for mean zonal flow (the equatorial jet) to advect air around the planet:

$$\tau_{\text{adv}} = L/U_{\text{eq}}. \quad (3.3)$$

Here, U_{eq} is the “wind speed that would result from acceleration of the wind from day to night due to the day–night pressure gradient if the day–night temperature

difference were in radiative equilibrium and if the Rossby number exceeds unity” ([Zhang and Showman, 2017](#)):

$$U_{\text{eq}} = \left(R \Delta T_{\text{eq}} \Delta \ln p / 2\mu \right)^{1/2}, \quad (3.4)$$

where ΔT_{eq} is the day-night temperature difference, and “ $\Delta \ln p$ is the difference in log pressure between some deep pressure where the day–night temperature difference is small (10 bars in the theory and simulations from ([Komacek and Showman, 2016](#)) and some smaller pressure of interest in the observable atmosphere” ([Zhang and Showman, 2017](#)). The usefulness of this simple model led to the work in Chapters 1 and 2, to predict the jet speed and global temperature distribution using a linear shallow-water model.

3.2.2 Hot-Spot Shift

[Zhang and Showman \(2017\)](#) predicts the longitude of maximum temperature λ_m (i.e. the hot-spot shift) to be given by:

$$\sin(\lambda_s - \lambda_m) e^{\lambda_m/\xi} = \frac{\eta}{\xi \cos \lambda_s} \quad (3.5)$$

where $\xi = \tau_{\text{rad}}/\tau_{\text{adv}}$ and $\lambda_s = \tan^{-1} \xi$. When λ_m , this reduces to the same expression as in Chapter 2, $\lambda_m = \tan^{-1}(\tau_{\text{rad}}/\tau_{\text{adv}})$. This expression is based on the hot-spot shift being governed by a balance of eastward heat transport versus radiation to space. It does not properly represent the effect of the stationary waves that are so important to the global temperature distribution, so does not apply in regimes where these dominate or in regions away from the equator.

3.2.3 Day-Night Contrast

Using this 1D model, [Zhang and Showman \(2017\)](#) predict the day-night contrast of the planet to be:

$$A = \frac{\Delta T}{\Delta T_{\text{eq}}} \sim 1 - \frac{2}{\alpha + \sqrt{\alpha^2 + 4\gamma^2}} \quad (3.6)$$

where the non-dimensional parameters α and γ are

$$\begin{aligned} \alpha &= 1 + \frac{\left(\Omega + \frac{1}{\tau_{\text{drag}}}\right) \tau_{\text{wave}}^2}{\tau_{\text{rad}} \Delta \ln p} \\ \gamma &= \frac{\tau_{\text{wave}}^2}{\tau_{\text{rad}} \tau_{\text{adv, eq}} \Delta \ln p} \end{aligned} \quad (3.7)$$

For a short radiative timescale τ_{rad} , A is large so there is a strong day-night contrast. From the point of view of a balance of the radiative and advective timescales this is because the heated air on the day-side radiates away its energy faster than it can be transported to the night-side by jet advection or wave transport ([Zhang and Showman, 2017](#); [Hammond and Pierrehumbert, 2017](#)). From the alternative point of view of an atmosphere dominated by stationary waves, this is because the high radiative damping rate brings the forced wave response into phase with the forcing and strengthens it, as discussed in Chapter 2 ([Hammond and Pierrehumbert, 2018](#)).

It is not clear whether these are two different views of the same process, or really two different processes. It may be that the first description does not properly capture the effect of wave dynamics and the second picture does not represent the effect of advection. It may be the case that different planets are better explained by different descriptions. See Section 3.6 for a more detailed discussion of the role of waves versus advection in the creation of a hot-spot shift.

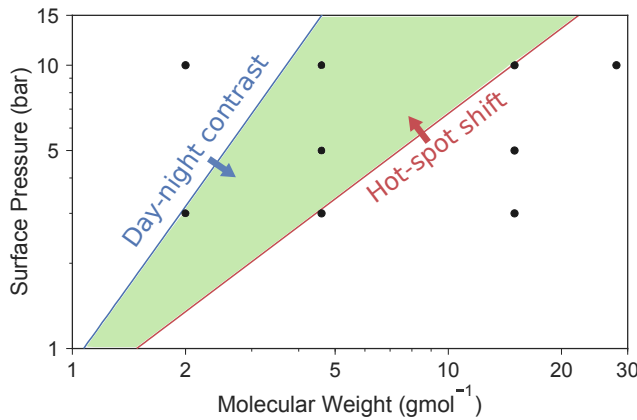


Figure 3.4: The atmospheric parameter space, where the green region is predicted by the relations of [Zhang and Showman \(2017\)](#) to support both a significant hot-spot shift and day-night contrast. The black points show the GCM tests. The hot-spot shift and day-night contrast were calculated with advection speed 1000 m s^{-1} and mean temperature 2000 K . The two lines correspond to a hot-spot shift of 20° and a day-night contrast of 80%.

3.2.4 Parameter Space

Figure 3.4 shows a parameter space defined by atmospheric surface pressure and mean molecular weight, that the 1D scaling relations predict to be potentially consistent with the observed thermal phase curve. The hot-spot shift was calculated at every point using Equation 3.5, and a line plotted to show the region where it should be greater than 20° . The day-night contrast was calculated at every point using Equation 3.6, and a similar line plotted to show the region where it should be greater than 80%.

The region shaded in green between these lines shows the possible parameter space that could support both a significant hot-spot shift and day-night contrast, and be consistent with the phase curve. The regions outside these lines may have one of these features, but not both. In the next section, I will use this parameter space to select a suite of GCM simulations to compare to the observed phase curve.

3.3 Simulating a Lava Planet

In this section, I will describe how I set up our GCM Exo-FMS to simulate an idealised atmosphere on 55 Cancri e. I will also describe the suite of tests performed on the basis of the scaling relations in Section 3.2

3.3.1 Exo-FMS Setup

We used the GCM Exo-FMS to simulate idealised atmospheres with different bulk properties on 55 Cancri e. Appendix A describes the structure and components of Exo-FMS in detail. It is based on the Flexible Modelling System structure and associated latitude-longitude dynamical core, from the Geophysical Fluid Dynamics Laboratory (GFDL). Similar models based on the same system have been used to investigate other terrestrial and tidally locked planets (Merlis and Schneider, 2010; Heng et al., 2011; Koll and Abbot, 2015, 2016). The general results of simulations of these tidally locked planets are not sensitive to the choice of model, as shown by the results of different models (Carone et al., 2014; Kataria et al., 2014; Charnay et al., 2015).

In all of the GCM simulations in this chapter, the planet has radius $r_p = 1.91 R_{Earth}$, orbital period $P = 0.737$ days, surface gravity $g = 21.7 \text{ ms}^{-2}$ (Demory et al., 2016), incoming stellar flux $3.55 \times 10^6 \text{ Wm}^{-2}$ (Von Braun et al., 2011), and zero surface and atmospheric albedo. In Chapter 4 I will discuss the effect of planetary albedo in more detail.

The simulations in Exo-FMS used a 144x96x40 grid, a 1D grey-gas radiative solver, and a 1D dry-convective adjustment routine, with top pressure level $10^{-5} p_s$, for surface pressure p_s . We chose to set the shortwave optical depth to zero and only vary the longwave optical depth, for simplicity – later, I will discuss the possible effects of shortwave absorption. We chose a default longwave optical depth of 10 for the tests,

and varied this in some of them. This was chosen to achieve a global mean temperature that was consistent with the thermal phase curve, as the maximum brightness temperature was several hundred Kelvin hotter than a bare-rock planet would be.

This optical depth was also consistent with the surface temperature achieved by a 10 bar H₂ atmosphere, using a one-dimensional radiative-convective model with two-stream radiative transfer calculated using the H₂ collisional opacity ([Pierrehumbert and Gaidos, 2011](#)). This corresponds to an opacity κ of 22.4 cm² kg⁻¹, which we used in all the tests apart from those where the opacity was explicitly varied. In reality, κ could be different, and would not scale linearly with pressure – a more realistic representation such as that in Chapter X would be needed to interpret future observations. For the purposes of this dynamical investigation, this simplified radiative scheme was chosen to preserve the focus on the effect of bulk properties on global circulation.

The simulations were initialised with zero winds. Each column of the model was initialised from a dry adiabat from a specified surface temperature, which was set to an isotherm when it reached a certain minimum temperature. The initial surface and isotherm temperatures were chosen to be close to the equilibrium state of each model, for smooth spin-up – the choice was not important to the final results, as the radiative adjustment timescale was less than one day for most of the atmosphere.

We considered the atmosphere to have reached equilibrium when both the OLR and top-of-atmosphere temperatures stopped evolving, and when the global mean temperatures and zonal winds stabilised ([Boutle et al., 2017](#)). Our simulations reached equilibrium before 10 Earth days, owing to the short radiative time scale. All results presented are for averages over the final 10 days of 50 day runs.

Test	Composition	p_s	μ	τ_∞	Hot-Spot Shift	Day-Night Contrast
1	H ₂	10	2.0	8	0°	100
2	N ₂	10	28.0	8	0°	200
3	H ₂ + N ₂	10	4.6	8	0°	100
4	H ₂ + N ₂	5	4.6	8	0°	100
5	H ₂ + N ₂	3	4.6	8	0°	100
6	H ₂ + N ₂	10	15.0	8	0°	100
7	H ₂ + N ₂	5	15.0	8	0°	100
8	H ₂ + N ₂	3	15.0	8	0°	100
9	H ₂ + N ₂	5	14.6	2	0°	100
10	H ₂ + N ₂	5	4.6	4	0°	100
11	H ₂ + N ₂	5	4.6	8	0°	100

Table 3.1: Suite of GCM simulations, testing the effect of varying the atmospheric mean molecular weight μ , surface pressure p_s , and optical thickness τ_∞ . Test 4 is the “best-fit” test discussed in Section 3.6.

3.3.2 Suite of Tests

I chose a suite of tests for the GCM based on the scaling relations in Section 3.2, listed in Table 3.1 and plotted in Figure 3.4. The tests span the parameter space predicted by the expressions of [Zhang and Showman \(2017\)](#) to be potentially consistent with the observed thermal phase curve. Some simulations test the effect of a particular parameter in more detail, such as Tests 3, 4, and 5, which test the effect of changing the surface pressure p_s . In the next section, I will discuss the tests in turn and show the effect of each parameter on the global circulation and thermal phase curve.

3.4 Results

In this section, I will discuss the results of the simulations in Exo-FMS. I will show the effect of varying the mean molecular weight, surface pressure, and optical thickness of the atmosphere, and compare the results to the theory in Section 3.2.

The simulations qualitatively behave as expected, with the predicted relations

between the phase curve and the planetary parameters. However, none of the tests will exactly fit the phase curve, showing that this simplified model can indicate what sort of atmosphere is consistent with the observations but cannot exactly recreate them.

3.4.1 Effect of Mean Molecular Weight

The first set of tests investigate the effect of mean molecular weight μ on the global circulation and thermal phase curve. We selected a range of molecular weights from 2.0 g mol^{-1} to 28.0 g mol^{-1} , corresponding with H_2 to N_2 , from the parameter space in Section 3.2.4.

Test 1 is a pure H_2 atmosphere with $\mu = 2.0 \text{ g mol}^{-1}$, surface pressure $p_s = 10 \text{ bar}$ and optical thickness $\tau_\infty = 8.0$. Section 3.2 predicts that this atmosphere will have a large hot-spot shift but a small day-night contrast, due to its high specific heat capacity, giving a long radiative timescale.

Figure 3.5 confirms this prediction, showing that it has a large hot-spot shift in the mid-atmosphere, with the hottest hemisphere centred at about 45° . The difference in temperature between the day-side and night-side at this pressure level is not as large as in Test 2, as predicted. The surface air temperature does not show such a large hot-spot shift, as it is closely coupled to the incoming stellar flux as explained earlier. The brightness temperature corresponds to a very low pressure due to the high longwave optical depth of the atmosphere, where the radiative timescale is much longer than the advective timescale so the global temperature is almost uniform.

Test 2 is a pure N_2 atmosphere with $\mu = 28.0 \text{ g mol}^{-1}$, surface pressure $p_s = 10 \text{ bar}$ and optical thickness $\tau_\infty = 8.0$. Section 3.2 predicts that this atmosphere will have a large day-night contrast but a small hot-spot shift, due to its low specific heat capacity, giving a short radiative timescale.

Figures 3.5 and 3.8 confirm this prediction, showing a large difference in day-side

and night-side temperature at all pressure levels, and in the brightness temperature. The hot-spot is centred on the substellar point, also confirming the prediction of a small or zero hot-spot shift. The effect of an increased phase shift at lower μ is consistent with [Kataria et al. \(2014\)](#).

These two extremes of μ behave as predicted by Section 3.2. Figure 3.4 therefore suggests than an intermediate value of μ may fit the observations better. Test 3 is a mixture of H₂ and N₂, with $\mu = 4.6 \text{ gmol}^{-1}$, surface pressure $p_s = 10 \text{ bar}$ and optical thickness $\tau_\infty = 8.0$. Figure 3.5 shows that at the half-surface-pressure level, and in the brightness temperature, there is a significant hot-spot shift and day-night contrast (although not as large as that observed by [Demory et al. \(2016\)](#)).

In the rest of this chapter, I will show the effect of the surface pressure and long-wave optical thickness on the global circulation and simulated phase curve. Of these first three tests, Tests 1 and 2 reproduce the observed hot-spot shift or day-night contrast respectively – but not both. Test 3 has a significant hot-spot shift and day-night contrast, but neither is as large as the observations. All of these tests qualitatively match the predictions of Section 3.2.

3.4.2 Effect of Surface Pressure

This section will show the effect of varying the surface pressure p_s . Section 3.2 predicts that the surface pressure has a similar effect to the mean molecular weight (via the heat capacity). At low surface pressures, the radiative timescale is short so should be a large day-night contrast and small hot-spot shift, and vice versa. The surface pressure and the specific heat capacity could be combined into a single “atmospheric heat capacity”, given that their effect in Section 3.2 is the same.

Figure 3.6 shows the temperature at the half-surface-pressure level for these tests. The first row shows Tests 4, 5, and 6, with $\mu = 4.6 \text{ gmol}^{-1}$ and $p_s = 10, 5, \text{ and } 3 \text{ bar}$. As expected, the tests with higher p_s have a larger hot-spot shift and smaller day-night

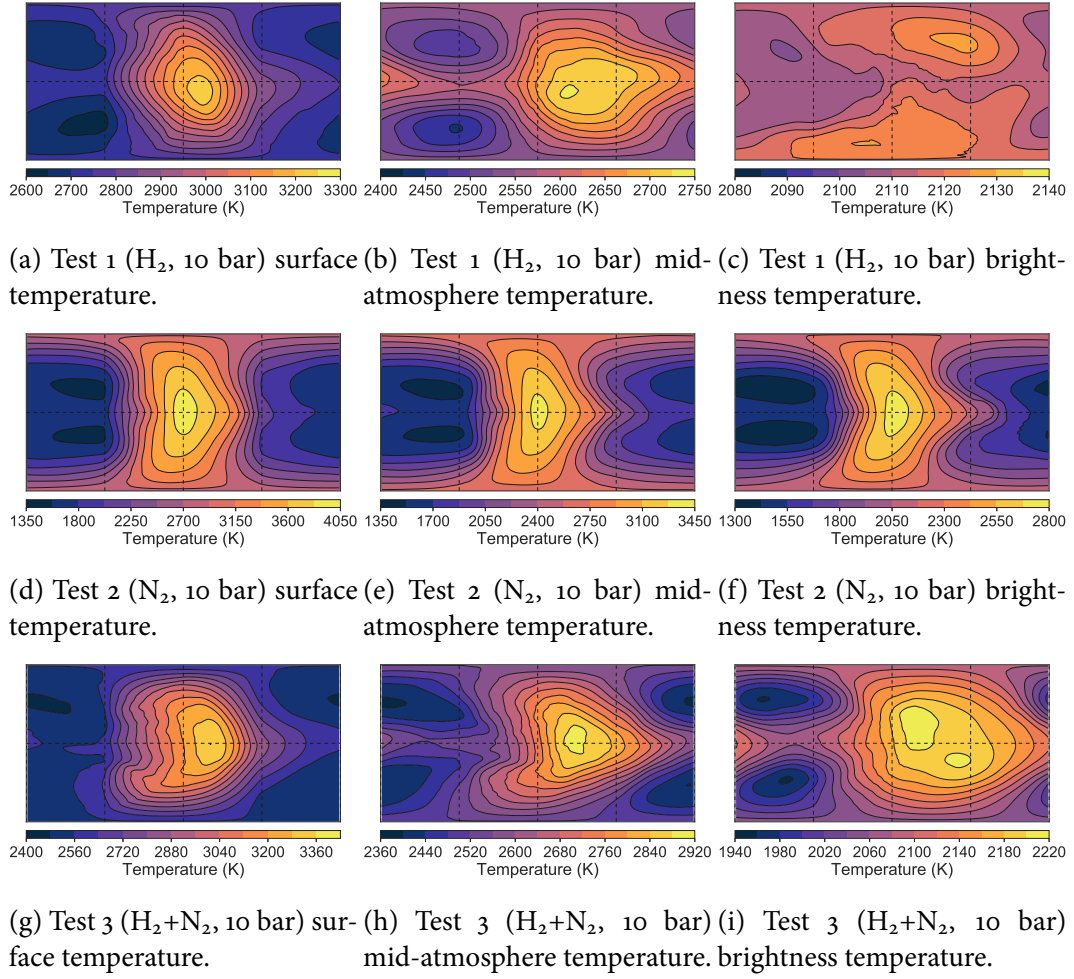


Figure 3.5: 10-day time-averaged maps of different temperature fields for Tests 1, 2, and 3. Each row is a different test. The first column shows the surface air temperature, which has the strongest day-night contrast as it is closely coupled to the surface temperature and stellar forcing. The second column is the temperature at the half-surface-pressure level, which can support both a large hot-spot shift and day-night contrast. The third column is the grey brightness temperature, which generally corresponds to a low atmospheric pressure, due to the high optical thickness.

contrast. The second row shows Tests 7, 8, and 9 with $\mu = 15.0 \text{ gmol}^{-1}$ and $p_s = 10, 5$, and 3 bar. Again, the tests with higher p_s have a larger hot-spot shift and smaller day-night contrast. In comparison with the corresponding tests in the first row, all these tests have a larger day-night contrast and smaller hot-spot shift due to their higher mean molecular weight (as explained in Section 3.4.1).

Test 3, with $\mu = 4.6 \text{ gmol}^{-1}$ and $p_s = 10 \text{ bar}$, is consistent with the phase shift and amplitude of the maximum of the observed phase curve, but has a hotter night-side than the observations. Test 5 with $\mu = 4.6 \text{ gmol}^{-1}$ and $p_s = 5 \text{ bar}$ is a better fit as it matches the day-side of the observations, and comes closer to matching the night-side. So, I will consider Test 4 with $p_s = 5 \text{ bar}$ to be the “best-fit” test (although none of the simulations exactly matched the observations).

The simulations show that a low mean molecular weight of $\mu = 2.0 \text{ gmol}^{-1}$ or below cannot be consistent with the observations as the day-night contrast would be too small, as predicted by the scaling relations of [Zhang and Showman \(2017\)](#). They also show that a high mean molecular weight of $\mu = 28.0 \text{ gmol}^{-1}$ or above cannot be consistent as the contrast would be too large. In addition, a very high or very low surface pressure cannot match the observations. So, they suggest an atmosphere which is heavier than $\mu = 2.0 \text{ gmol}^{-1}$ (but not too heavy), and with a surface pressure in the range 1 to 10 bar. These conclusions are similar to other studies using different observations and models ([Winn et al., 2011a; Angelo and Hu, 2017](#)).

In the rest of this chapter, I will discuss the effect of the longwave optical thickness of the atmosphere, and the effect of other bulk parameters on its vertical structure and observable properties. I will suggest that night-side cloud formation could be responsible for the observed low temperatures on the night-side, which are the only part of the observations that cannot be reproduced by the GCM.

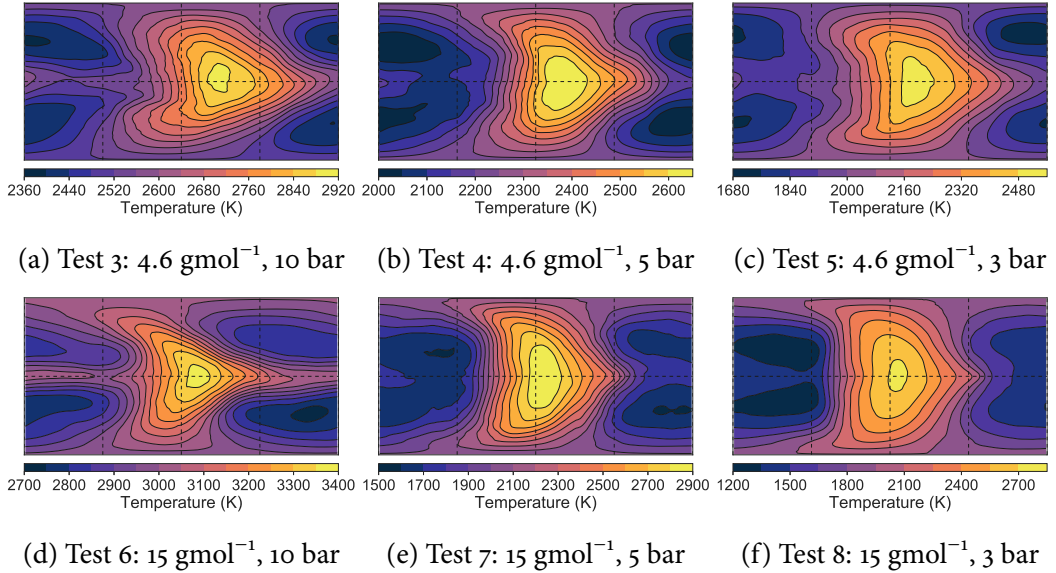
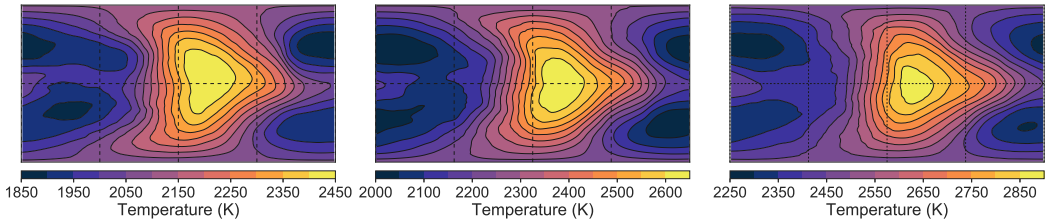


Figure 3.6: 10-day time-averaged temperatures at half-surface-pressure, for atmospheres with $\mu = 4.6 \text{ gmol}^{-1}$ and 15 gmol^{-1} $\text{H}_2 + \text{N}_2$ atmospheres with surface pressures of 3, 5, and 10 bar.

3.4.3 Effect of Optical Thickness

This section shows the effect of changing the longwave optical thickness τ_∞ . Its main effect is to change the global mean temperature, without strongly affecting the global circulation, temperature distribution, and phase curve. The longwave optical thickness is approximately constrained by the maximum observed flux in the thermal phase curve.

Figure 3.7 shows three atmospheres based on the “best-fit” Test 4. Tests 7, 8, and 9 have $p_s = 10 \text{ bar}$ and $\mu = 4.6 \text{ gmol}^{-1}$, with $\tau_\infty = 8.0, 4.0$, and 2.0 . Section 3.2 predicts that τ_∞ will not have a large effect on the hot-spot shift and fractional day-night contrast, apart from by scaling the global mean temperature. In Figure 3.7, the tests do indeed have similar global temperature distributions, only differing greatly in their mean temperatures. Later, Figure 3.11 will show that varying τ_∞ just scales the magnitude of the thermal phase curves, with no significant differences in hot-spot shift or fractional day-night contrast.



(a) Test 9: 4.6 gmol^{-1} , H_2+N_2 , (b) Test 10: 4.6 gmol^{-1} , H_2+N_2 , $\tau_\infty = 2.0$: half-surface-pressure air temperature (c) Test 11: 4.6 gmol^{-1} , H_2+N_2 , $\tau_\infty = 4.0$: half-surface-pressure air temperature. $\tau_\infty = 8.0$: half-surface-pressure air temperature.

Figure 3.7: The temperature at the half-surface-pressure level for Tests 10, 11, and 12, with $\mu = 4.6 \text{ gmol}^{-1}$, surface pressure 5 bar and optical thicknesses of 2.0, 4.0, and 8.0.

Returning to the question of which simulation fits the observations best, Figure 3.11 shows that Test 11 with $\tau_\infty = 8.0$ matches the position and magnitude of the observed phase curve best. However, Test 10 with $\tau_\infty = 4.0$ is closer to the observed night-side temperature, while still consistent with the day-side temperature. As before with the surface pressure and mean molecular weight, we cannot fit the observations to a specific optical thickness, but can define a range of possible values from $\tau_\infty = 8.0$ to 2.0.

3.4.4 Vertical Structure

The thermal phase curve that would result from any of these simulations depends on the radiative properties of the atmosphere at the wavelength (or in the wavelength range) of the observations. Normally this is approximated as a single radiating level, although it is possible that the emitted thermal radiation depends on more than one level of the atmosphere.

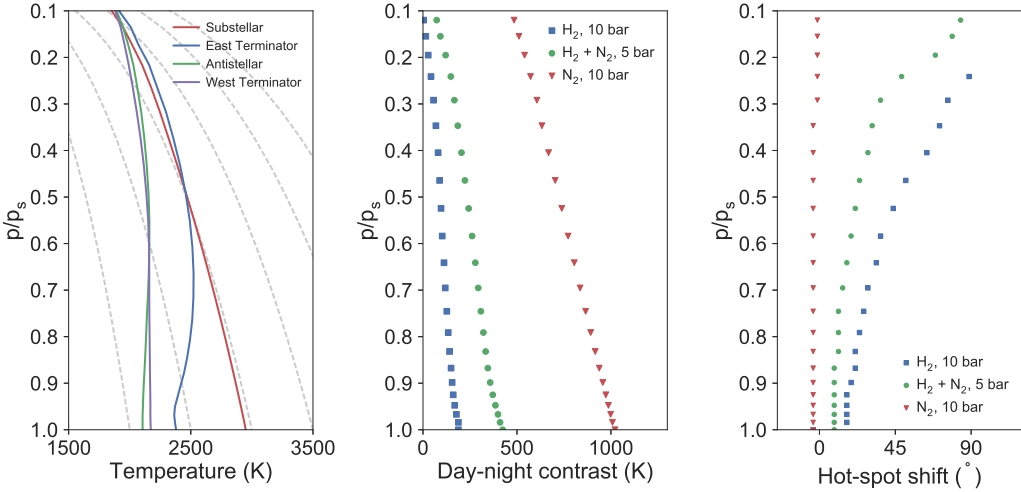
Approximating the thermal phase curve as corresponding to a single pressure level, it depends very strongly on which level this is. If the outgoing radiation is from the surface, it will have almost no hot-spot shift and a large day-night contrast,

as in these simulations the surface temperature is mostly set by the incoming stellar radiation. If the outgoing radiation is from very high in the atmosphere, it could be almost uniform with orbital phase due to efficient circulation (such as in Test 1), or it could still have a large day-night contrast, such as in Test 2. In this section, I will examine the vertical structure of the test atmospheres, and discuss how the observable quantities vary with pressure level.

Figure 3.8a shows temperature-pressure profiles of vertical columns spaced around the equator of the planet for Test 4. The red line at the substellar point is convective at high pressures, driven by the stellar heating at the surface. The blue line at the east terminator has a temperature inversion above the lower atmosphere, as the eastward jet heats it at about $0.5 p_s$, but the surface is not heated by stellar radiation. The green line at the antistellar point is almost isothermal, balanced by heating from the jet – weaker than at the east terminator – and longwave cooling. These profiles show how the observable day-night contrast varies with pressure level and depends on thermal structure, as at the surface the profiles are well separated but at low pressure they are almost uniform.

Figure 3.8b shows this in more detail, plotting the day-night contrast at each pressure level in the atmosphere for Tests 1, 2, and 4. This suggests that the large observed day-night contrast corresponds to low in the atmosphere. However, the high longwave optical thickness means that the outgoing radiation in the model comes from high in the atmosphere, as shown in Figure 3.5. This suggests that in reality, the opacity at $4.5 \mu\text{m}$ could be lower than the mean longwave opacity – so the mean opacity is high enough to match the observed brightness temperature, but the $4.5 \mu\text{m}$ opacity is low enough so that a sufficiently high atmospheric pressure is observed.

Figure 3.8c shows how the hot-spot shift varies with atmospheric pressure. It is always small low close to the surface, where the temperature is closely coupled to the incoming stellar radiation due to the lack of shortwave absorption in these simula-



(a) Temperature-pressure profiles for columns spaced pressure level, showing how it sure level (up to where the evenly around the equator is larger towards the surface. temperature gradient is too of Test 4. Dry adiabats are plotted in grey.

(b) Day-night contrast at each pressure level (up to where the temperature gradient is too small for a distinct hot-spot shift).

Figure 3.8: The vertical structure of Test 4, and the hot-spot shift and day-night contrast of Tests 1, 2, and 4. The temperature profiles tend to follow the dry adiabat at high pressures on the day-side, but can become isothermal or inverted on the night-side. The lower atmospheres have a larger day-night contrast, and the upper atmospheres have a larger hot-spot shift – hence the focus on the middle atmosphere to match the observed phase curve, with both of these features.

tions. The shift generally increases with height, as the eastward jet becomes stronger and produces a shift in the wave pattern (or just advects warm air). Higher in the atmosphere, the transport can become so effective that the temperature becomes homogenous so there is no distinct hot-spot shift to measure.

3.4.5 Phase Curves

Figure 3.9 shows how the radiating level determines the features of the observed phase curve. The different phase curves correspond to the outgoing radiation at $4.5 \mu\text{m}$ calculated from the temperatures of various pressure levels in Test 4. The figure shows this instead of the OLR from the model, as in reality the atmosphere

will not be grey, and the $4.5\text{ }\mu\text{m}$ radiation could correspond to any level.

As shown above, the phase curve at a pressure level close to the surface has a large amplitude and small phase shift. High in the atmosphere, the phase curve has a smaller amplitude and large phase shift. This can be explained with the models in Chapter 2, or the models of [Zhang and Showman \(2017\)](#), as due to the the shorter radiative timescale nearer the surface.

There is a strong degeneracy in interpreting the observations, as the radiating level and mean molecular weight have a very similar effect. Figures 3.9 and 3.12 both show phase curves varying from a large amplitude, low phase shift curve to one with low amplitude and large phase shift. In the simple picture of [Zhang and Showman \(2017\)](#), these have the same effect on the circulation as they affect the radiative timescale in the same way. This degeneracy is not too great a problem in this chapter, as the observed phase curve is so extreme that both the radiating level and mean molecular weight must be tightly constrained to come close to matching it.

Observations at multiple wavelengths corresponding to multiple radiating levels could break this degeneracy, for phase curves that could otherwise fit different sets of parameters. As discussed earlier, it is possible to explain the high observed brightness temperature and large hot-spot shift if the atmospheric opacity $4.5\text{ }\mu\text{m}$ is lower than average in the longwave region – i.e., it is observed in a window. Observations at different wavelengths could answer this question, and show whether phase curves at different pressure levels vary as predicted by these models. Broadband observations could constrain the mean longwave opacity, and provide a comparison to phase curves measured at specific radiating levels. Chapter 4 discusses these possibilities in more detail.

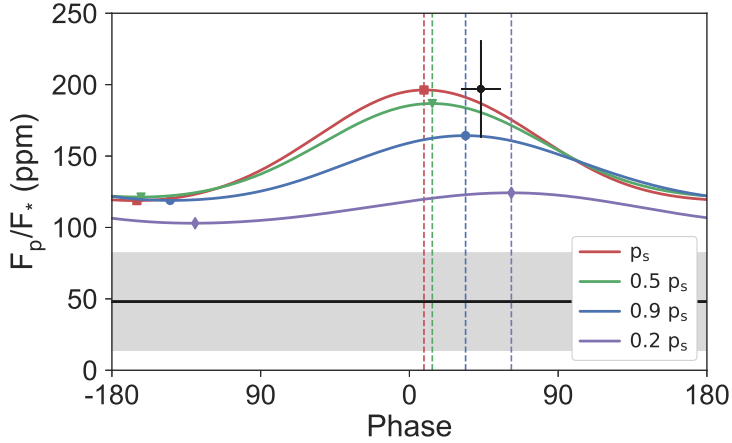


Figure 3.9: Thermal phase curves calculated at different radiating levels in Test 4. Moving the radiating level to lower pressures has a similar effect to decreasing the mean molecular weight, as shown in Figures 3.12 and 3.13, producing a degeneracy in interpreting the observed phase curve. The black point shows the maximum (day-side) observed flux, and the black line shows the minimum (night-side) observed flux.

3.5 Simulated Observations

In this section, I will discuss phase curves calculated from the GCM simulations shown previously. These can be directly compared to the observations, although lose the latitudinal resolution of the earlier temperature maps. This can make different global states appear the same, which is useful to be aware of when interpreting observations.

The 4.5 μm phase curves were calculated using either the outgoing longwave radiation from the grey-gas model, or for a specific radiating level using the temperature of that level. This flux was integrated over the hemisphere centred on each grid cell around the equator, to produce the phase curve (Cowan and Agol, 2008):

$$I_p(\xi) = \frac{\int_{-\pi/2}^{\pi/2} \int_{-\xi-\pi/2}^{-\xi+\pi/2} I_{4.5}^\uparrow|_{p=0} \cos(\lambda + \xi) \cos^2(\theta) d\lambda d\theta}{\int_{-\pi/2}^{\pi/2} \int_{-\xi-\pi/2}^{-\xi+\pi/2} \cos(\lambda + \xi) \cos^2(\theta) d\lambda d\theta} \quad (3.8)$$

where the phase angle is ξ , the outgoing 4.5 μm flux is $I_{4.5}^\uparrow|_{p=0}$, longitude is λ , and

latitude is θ . The ratio of planetary flux to stellar flux is:

$$\frac{F_p}{F_\oplus} = \frac{I_p}{I_\oplus} \left(\frac{r_p}{r_\oplus} \right)^2 \quad (3.9)$$

where the ratio of planetary radius to stellar radius is $\frac{r_p}{r_\oplus} = 0.0187$ and the effective temperature of the star is 5196 K ([Von Braun et al., 2011](#)).

Figure 3.12 shows the phase curves of atmospheres with different values of mean molecular weight, calculated using the outgoing longwave radiation from each test. The black points show the maximum and minimum of the observed phase curve. The tests with extreme values of molecular weight do not fit the observations well, as discussed previously. The phase curve of Test 1 (pure H₂) has a large phase shift, but a very small amplitude due to its efficient heat transport from day-side to night-side. The wave-based theory in Chapter 2 would explain this as the low molecular weight giving a low radiative damping rate, producing a weak wave response and a more zonally uniform response like that in Figure 2.11a.

Test 2 has the opposite problem, where the amplitude is sufficiently large but the phase shift is too small to fit the observations due to its high radiative damping rate. The phase curve of Test 4 fits the observations better (as did its temperature distribution in Section 3.4.2) – it has a large amplitude and offset, although neither is quite as large as those in the observations. The relatively low amplitude of all of the tests in Figure 3.12 may be due to the use of the model OLR in the phase curve. As discussed above, it may be that the observations at 4.5 μm correspond to an atmospheric window, so actually reflect a lower level in the atmosphere which would give a larger amplitude phase curve.

To test this idea, Figure 3.13 shows the phase curves corresponding to the brightness temperature of a radiating level at half the surface pressure for the same tests. Test 4 (H₂-N₂) fits the observations better in this figure than in Figure 3.12 where the

model OLR was used. Here, it has a larger amplitude and a large phase shift due to the lower radiating level. The night-side flux is still higher than the observations as in most of the tests – later, I will discuss the possibility of night-side cloud formation producing a difference between the model and the observations.

Figure 3.10 shows the phase curves of the tests in Section 3.4.2, where the surface pressure of the “best-fit” Test 4 was varied to compare to observations. These curves show how increasing the surface pressure increases the phase offset and magnitude, due to the longer radiative timescale and increased temperature (with a constant opacity, increasing surface pressure increases optical thickness and temperature). However, the tests with higher pressure also have a higher night-side flux due to the long radiative timescale, so the overall fractional amplitude of the curve decreases. The case with $p_s = 10$ bar matches the position and magnitude of the observed maximum best, but does not match the observed minimum flux well. The 5 bar case is close to both the observed maximum and minimum, so I will treat it as the best-fit case.

Finally, Figure 3.11 shows the phase curves of the tests in Section 3.4.3, where the optical thickness of Test 4 was varied. As expected from Section 3.2, the optical thickness only affects the magnitude of the phase curve, and the curves are approximately the same when normalised. In particular, the hot-spot shifts are very similar. The optical thickness is something of a free parameter in this study, which does not affect the global circulation as strongly as the other parameters, and can be tuned to match the observed maximum day-side flux.

Generally, the phase curves of the flux from the half-surface-pressure level match the observations better than those corresponding to the model OLR. This points towards an absorption window at $4.5\text{ }\mu\text{m}$, as it seems unphysical that the atmosphere could be hot enough to match the observed maximum flux, but also that the upper part of an optically thick atmosphere could match the large hot-spot shift and day-

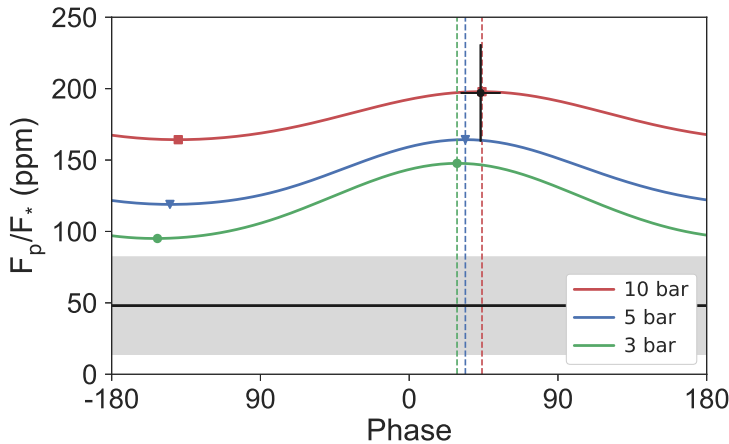


Figure 3.10: Phase curves calculated using the emission from the half-surface-pressure level of the $4.6 \text{ gmol}^{-1} \text{ H}_2 + \text{N}_2$ atmospheres with surface pressures of 3, 5, and 10 bar, corresponding to the temperature maps in Figure 3.6.

night contrast.

In summary, the thermal emission from the half-surface-pressure level of Test 4 matched the observations best. In Figure 3.13, it matches the observed phase curve peak offset and magnitude, but did not match the observed minimum (although came closer than other similar tests). In general, the phase curves from the half-surface-pressure level matched the observations much better than the OLR phase curves, suggesting an absorption window at $4.5 \mu\text{m}$. I will discuss the possible effects of clouds and condensable species in the next section, particularly how they could resolve the difference in night-side flux between the models and the observations.

3.5.1 Condensables and Clouds

All the tests above that have approximately matched the day-side emitted flux and day-side hot-spot shift, have all had too much night-side flux to match the observations there (such as Test 4 in Figure 3.13). If the observations are accurate, it seems likely that some other physical process is at work. In this section, I will dicuss the possibility that clouds form on the night-side only, raising the radiating level and

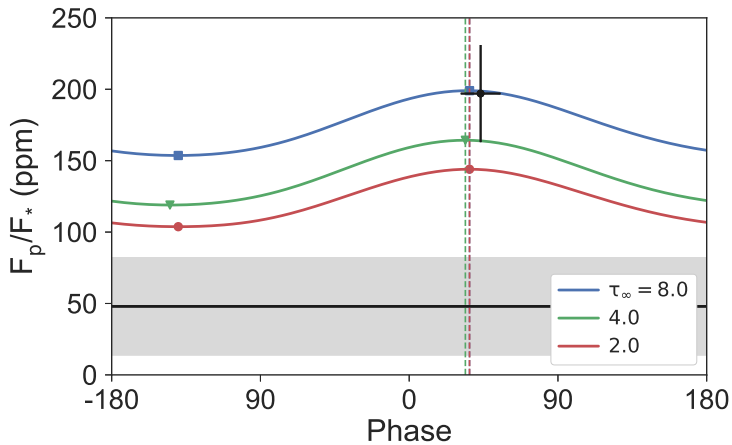


Figure 3.11: Phase curves calculated using the emission from the half-surface-pressure level of the 5 bar 4.6 gmol⁻¹ H₂ + N₂ atmospheres with optical thicknesses of 2.0, 4.0, and 8.0, corresponding to the temperature maps in Figure 3.7.

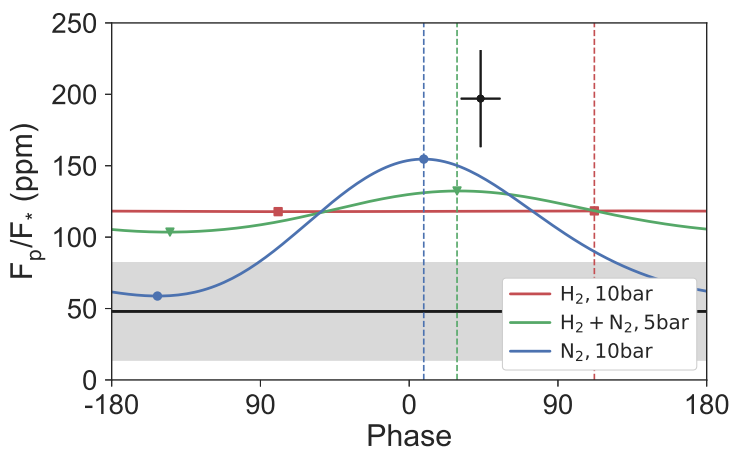


Figure 3.12: Simulated 4.5 μm phase curves calculated from the brightness temperature of the grey-gas OLR. The red curve is the 10 bar H₂ atmosphere, which has such efficient heat transport that it has a large peak offset and very small amplitude. The blue curve is the 10 bar N₂ atmosphere, with very weak heat transport so a large amplitude and peak offset. The green curve is the 5 bar H₂+N₂ atmosphere, with a significant offset and amplitude. The offset and amplitude are not as large as the Demory et al. (2016) measurements, shown by the black point and line (with their errors shown by the bars and the shaded area).

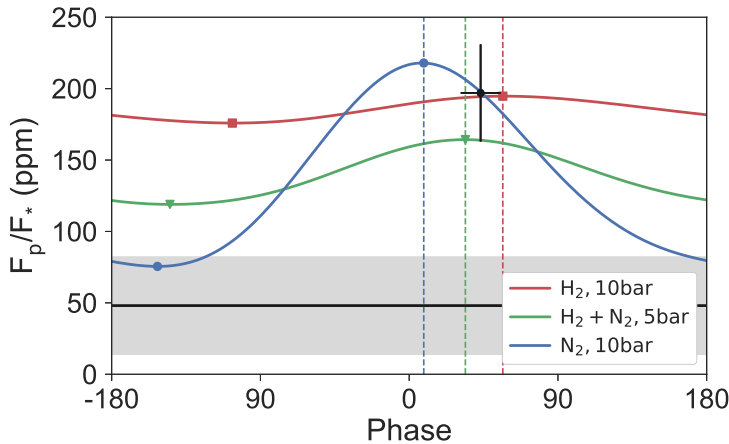


Figure 3.13: Simulated phase curves for the emission from a radiating level at half-surface-pressure. The amplitude and offset are larger than the phase curves of the OLR. The offset and amplitude are not as large as the [Demory et al. \(2016\)](#) measurements, but Figure 3.14 shows that the H_2+N_2 atmosphere (green curve) could match the observations with the night-side cloud formation discussed in Section 3.5.1.

lowering the brightness temperature and night-side flux. I will use a post-hoc calculation to estimate where clouds could form, and estimate their effect on the phase curve of the “best-fit” case, Test 4.

These clouds could be formed by condensables such as SiO or Na outgassed from a day-side magma ocean. [Miguel et al. \(2011\)](#) calculated the partial pressures of different species outgassed by a silicate magma in a vacuum at different temperatures. A magma ocean at 2700 K would support significant partial pressures of various species, dominated by SiO and Na with partial pressures of about 10 mbar. For the higher surface temperatures of over 3000 K in some tests, SiO becomes more abundant with partial pressures of hundreds of millibar.

I used [Miguel et al. \(2011\)](#) to calculate the partial pressures of SiO and Na based on a range of possible surface temperatures, then assumed that these were mixed uniformly with the rest of the atmosphere. Then I calculated the saturation vapour pressure of each species at the top of each column ([Wetzel et al., 2013](#)). Testing the effect of clouds at the top of the atmosphere shows the maximum effect they could

have on lowering the radiating temperature ([Parmentier et al., 2016](#)) (which in many cases is the same as if they formed lower down, as the stratosphere is quite isothermal in our tests). If this saturation vapour pressure was less than the local partial pressure, I assume that clouds have formed and set the radiating level to the top of the atmosphere.

I found that SiO could condense on the night-side of some tests, but that Na would not condense in any tests. Figure 3.14 shows that at high enough partial pressures of SiO, the clouds it forms could significantly increase the day-night contrast and phase curve amplitude. For a partial pressure of 300 mbar, the new post-processed phase curve matches the observations of [Demory et al. \(2016\)](#) within error. In addition, Figure 3.14 shows that for high enough partial pressures of SiO, cloud formation around the cool west terminator can increase the hot-spot shift. This is similar to the heterogenous day-side cloud formation shown to affect phase curves by [Parmentier et al. \(2016\)](#). This effect is small in the tests in this chapter, but could be more important for different species or for optical phase curves, where clouds can strongly affect reflected light.

These post-processed cloud models are basic, but show how silicate clouds could form, and would have a large effect on the observed phase curve. Further observations at different wavelengths could test for the presence of clouds – in particular, phase curves at optical wavelengths should be strongly affected by reflective clouds. A better understanding of the condensables that would be outgassed by the magma ocean, and what clouds they could form, would also be valuable. In the next chapter, I will discuss a study that coupled a dynamic cloud formation and transport model to this idealised model of 55 Cancri e, to investigate the effect of clouds in more detail.

In summary, SiO outgassed from a magma ocean is a plausible candidate for a cloud species that would form on 55 Cancri e and affect the observed phase cuve. It could form high on the cooler night-side, raising the radiating level and reducing the

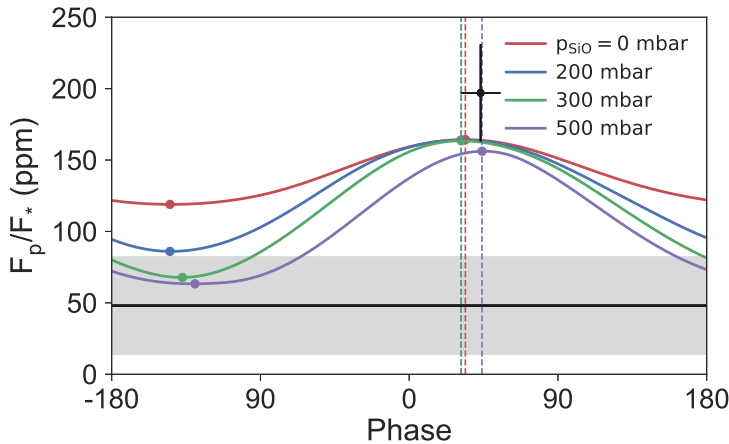


Figure 3.14: Simulated phase curves for different possible equilibrium surface partial pressures of SiO in the 4.6 g mol^{-1} , 5 bar $\text{H}_2 + \text{N}_2$ atmosphere, based on the range of temperatures on the day-side surface. The 300 mbar curve shows that clouds could form on the day-side at high enough surface partial pressures. The offset and amplitude of the 100 mbar case almost agrees with the ? measurements within error.

thermal flux observed from the night-side. This could explain the difference between the modelled and observed night-side flux in our simulations.

3.6 Discussion

The model results presented above suggest constraints on the atmospheric composition and parameters of 55 Cancri e. We started with the assumptions that the atmosphere has negligible shortwave opacity and is composed of diatomic molecules. Further modelling work should represent more realistic gaseous absorption and a variety of atmospheric compositions.

The test that fitted the observations best was Test 4, which was a 90%-10% mixture of H_2 and N_2 with $\mu = 4.6 \text{ g mol}^{-1}$, specific heat capacity $7443 \text{ J kg}^{-1} \text{ K}^{-1}$, optical thickness 4.0, and surface pressure 5 bar. This is similar to the predicted best-fit parameters in Figure 3.4, using the scaling theory of [Zhang and Showman \(2017\)](#). This test did not fit the observations of [Demory et al. \(2016\)](#), but confirmed that the scal-

ing relations are broadly accurate.

This means that while we cannot exactly fit the phase curve with our idealised model, we can constrain the atmospheric compositions. The results suggest that the atmosphere must have a mean molecular weight between 2 g mol^{-1} and 28 g mol^{-1} , as anything outside this range would have far too small a day-night contrast, or too small a hot-spot shift. The atmosphere must also be between 1 and 10 bar, for the same reasons.

We could not reproduce the observed phase curve with our GCM, as has been done by tuning the parameters of Hot Jupiter simulations (?). The best-fit test matched the observations day-side flux and hot-spot shift, but not the night-side flux. This could be due to night-side cloud formation as discussed in Section 3.5.1, or due to more fundamental differences with the model such as different composition or atmospheric absorption.

3.7 Conclusions

The thermal phase curve of 55 Cancri e is not easy to explain. It implies a large hot-spot shift and a large day-night temperature contrast, which can be mutually exclusive. In this chapter, I used scaling relations for the global circulation of tidally locked planets to predict what bulk atmospheric properties might produce a circulation that fitted this phase curve. I then modelled atmospheres in this parameter space to test the predictions of the scaling relations, and to compare to observations.

Test 4, the “best-fit” atmospheric simulation had a surface pressure of 5 bar and a mean molecular weight of 4.6 g mol^{-1} . It matched the observed hot-spot shift, in both the phase shift and maximum amplitude of the thermal phase curve. However, in a problem common to all of the test simulations, it did not match the observed night-side flux as it was too warm on the night-side. It is possible that night-side

cloud formation could raise the radiating level and lower the brightness temperature on the night-side, which I confirmed with a simple estimate of SiO cloud formation and will test further in Chapter 4.

It also appeared likely that if an atmosphere can explain the phase curve, the observations at 4.5 μm correspond to an absorption window, as they require a high temperature but a low radiating level – so, an optically thick atmosphere which is observed through a window. Further observations could resolve the questions and degeneracies raised in this chapter. For example, a broadband phase curve could constrain the mean brightness temperature and be compared to the 4.5 μm observations which may correspond to a window. Optical observations could reveal the distribution and properties of clouds.

In summary, this chapter has shown that the observed thermal phase curve of 55 Cancri e can be explained by an atmosphere with a surface pressure of 5 bar and a mean molecular weight of 4.6 g mol⁻¹, with some mechanism such as cloud formation to lower the night-side brightness temperature. The suite of GCM tests were consistent with the theories discussed so far in this thesis, although appear to not be sophisticated enough to match the observations exactly. In Chapter 4, I will use a more detailed radiative transfer model and a cloud formation model to investigate this problem further.

CHAPTER 4

Realistic Modelling of Lava Planets

The simulations in Chapter 3 used a highly idealised model of an atmosphere on 55 Cancri e to investigate the scaling properties of its dynamics. However, properly interpreting observations such as the thermal phase curve measured by Demory et al. (2016) requires a more realistic radiative transfer model. In this chapter, I will use the radiative transfer model Socrates (Edwards and Slingo, 1996) to simulate the atmosphere in more detail, and to produce realistic emission spectra and phase curves. This work follows studies like Miguel (2018) who simulated emission and transmission spectra for a variety of nitrogen-dominated atmosphere on 55 Cancri e with different absorbing species, and Ito et al. (2015) who did the same for outgassed rock vapour atmospheres.

In Section 4.1, I will describe the improvements made to Exo-FMS prompted by the simulations run in Chapter 3. I modified Exo-FMS to use a new dynamical core on a cubed-sphere grid, and coupled it to the Socrates radiative transfer scheme. I will outline the process of generating usable absorption data for modelling, and discuss the differences with the semi-grey model.

Section 4.2 discusses two control simulations with the same bulk parameters as two equivalent tests in Chapter 3, but using the Socrates radiative transfer scheme at

a low, fast resolution. I will show how the global circulation of each test is similar to the corresponding previous test, and suggest that this shows that the two radiative transfer schemes produce similar results. I will then simulate the outgoing longwave radiation at a higher resolution, and discuss how the global circulation affects this and the emission spectra at different orbital phases. Finally, I will simulate thermal phase curve at different wavelengths and in the Spitzer 4.5 μm bandpass, for comparison with the observations of [Demory et al. \(2016\)](#).

Neither of these control simulations fully match the observations, so in Section 4.3 I will discuss the results of a “best-fit” simulation similar to Tests 3 and 4 in Chapter 3. I will show that there is a hot-spot shift in the temperature field similar to the equivalent test in the previous chapter, but that this shift does not appear in the phase curves calculated from the outgoing longwave radiation. I will suggest that this is because the atmosphere is too thin, and test this hypothesis with a new test with 100 bar surface pressure in Section 4.4. The phase curve of this test will show a clear phase offset at some wavelengths, supporting the idea that the large observed hot-spot shift implies a thick atmosphere on 55 Cancri e.

Section 4.5 discusses the results of all the tests, and their implications for 55 Cancri e. I will use a simple two-layer model to explain why a sufficiently thick atmosphere is required for a hot-spot shift in the thermal phase curve, and use this to explain the results of the simulations in this chapter and the previous chapter. I will compare all of the results so far, and conclude that the scaling relations of Chapter 3 still usefully constrain the mean molecular weight using the phase curve, but that the new simulations add the additional condition that the atmosphere must be sufficiently thick.

I will conclude that the simulations in this chapter are evidence for a thicker than 10 bar atmosphere on 55 Cancri e, with mean molecular weight heavier than H₂. More observations are required, to improve the precision of the phase curve and

to better constrain the composition.

4.1 An Improved Lava Planet GCM

In this section, I will discuss the changes I made to Exo-FMS to improve its stability and to model radiative transfer in more detail. I will explain the benefits of the new cubed-sphere dynamical core, and outline the interface to the Socrates radiative transfer code.

4.1.1 Cubed-Sphere Dynamical Core

The simulations in Chapter 3 were affected by instabilities that appeared to be caused by high winds at the poles of the planet. The cell size of a latitude-longitude grid is very small in these regions, so the CFL condition requires a smaller timestep ([Courant et al., 1928](#)). This meant that the tests could be very slow to run, and were prone to crashing when the winds became too strong at the poles.

To avoid these problems, I updated the model to use a newer dynamical core on a cubed-sphere grid. Appendix A shows the geometry of the grid, and how its “poles” are less extreme than the latitude-longitude grid. The new dynamical core also uses a more modern code structure for the main routines and has less redundant code than the previous version of Exo-FMS, allowing for easier development. I also produced a new unified interface between the physical modules and the dynamical core, which simplifies swapping between modules used in the simulations. Simulations of 55 Cancri e ran much faster and more stably in the new model, allowing the more computationally expensive radiative transfer model Socrates to be more practically used.

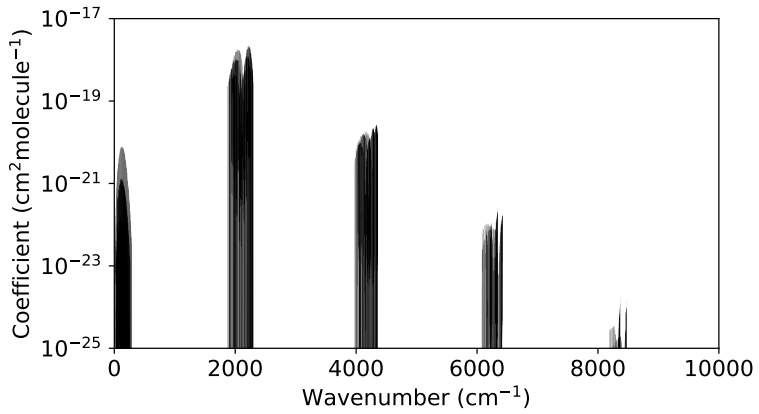


Figure 4.1: Absorption coefficient versus wavenumber for CO at 2500 K and 1 bar from the HITEMP database ([Rothman et al., 2010](#)). For the simulations in this chapter, the longwave radiation from the surface peaks at about 5000 cm^{-1} and the incoming stellar radiation peaks at about $10\,000\text{ cm}^{-1}$, so the longwave optical depth of the atmosphere is higher than the shortwave optical depth.

4.1.2 Socrates Radiative Transfer

In Chapter 3, I used a semi-grey radiative transfer scheme to model the atmosphere of 55 Cancri e. This reduced the complexity and number of parameters of the model, but had two main limitations. First, the scheme is a very simple representation of the radiative transfer inside the atmosphere, so might not have captured the details of the real radiative transfer and global circulation that would occur in such an atmosphere. Second, the outgoing longwave radiation that would be detected from the atmosphere had no wavelength dependence in the model, so the $4.5\text{ }\mu\text{m}$ radiation had to be post-processed from an implied radiating temperature – later in this chapter, I will show how this could produce unrealistic phase offsets in the thermal phase curve.

To follow up the work in Chapter 3, I therefore coupled the correlated-k radiative transfer scheme Socrates ([Edwards and Slingo, 1996](#)) to Exo-FMS. This scheme represents the wavelength-dependent radiative effects of real gases, unlike the previous wavelength-independent semi-grey model. I ran the GCM simulations using 30

spectral bands, and post-processed the output using the same model with 621 spectral bands. The simulated outgoing longwave radiation is a more accurate model than the post-processed radiating temperature approach used in the previous chapter.

The Socrates radiative transfer scheme requires a “spectral file” of gaseous absorption data including correlated-k coefficients to be generated from line lists. The simulations in this chapter use line lists from the HITEMPdatabase (Rothman et al., 2010). The simulations in this chapter used correlated-k coefficients calculated from line lists in the HITEMP2010 database (Rothman et al., 2010) using the utilities provided with the Socrates code (Edwards and Slingo, 1996). Figure 4.1 shows the absorption spectrum of CO, which I converted into Socrates spectral files of varying numbers of bands for the simulations.

4.2 Control Simulations

In this section, I will discuss two control simulations in the new model, based on two tests from Chapter 3. In this chapter, the control tests are Test 1 and Test 2. Test 1 has a 10 bar H₂ atmosphere with a 1% molar concentration of CO. Test 2 has a 10 bar N₂ atmosphere with a 1% molar concentration of CO.

It is not clear what gases are appropriate absorbers for the atmosphere of a lava planet, given the lack of observational characterisation. Hot Jupiter atmospheres are normally modelled with a variable metallicity (Amundsen et al., 2016), but the different formation pathways expected for the atmosphere of a terrestrial planet makes its composition less well constrained (Madhusudhan et al., 2016). Miguel (2018) modelled N₂-dominated atmospheres with absorbers such as CO, CO₂, and H₂O. Ito et al. (2015) modelled atmospheres of rock vapour such as SiO outgassed by a hypothetical magma ocean. In this chapter, I investigate the effect of an atmospheric opacity dominated by CO, as a physically plausible strong longwave absorber.

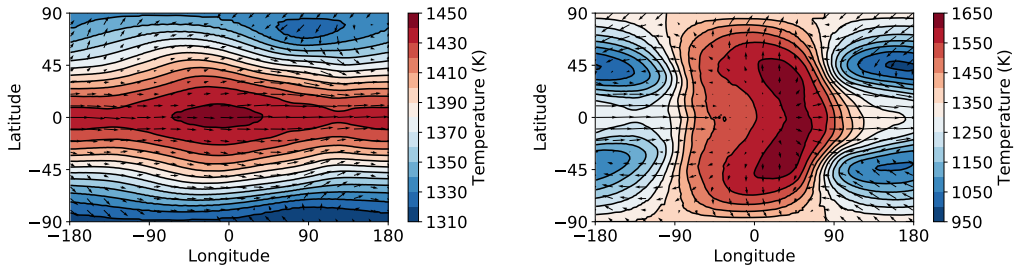
55 Cancri e is terrestrial and has been suggested to be carbon-rich ([Madhusudhan et al., 2012](#)), so CO or CO₂ are reasonable candidates for atmospheric absorbers. CO₂ would tend to disproportionate in to CO at these high temperatures ([Moses, 2014](#)), so in this chapter I will only consider the effect of CO. It is important to note that the aim is not to exactly test the hypothesis that CO is the only absorber on the planet, but instead to investigate the effect of more realistic radiative transfer in general, particularly the effect of different atmospheric opacities on the observed phase curve. I therefore suggest that the conclusions apply generally to any atmosphere without an extreme longwave or shortwave opacity, and should be useful in interpreting the thermal phase curve whatever the real composition.

The simulations were spun up for 100 days, and then data was time-averaged for either 100 or 200 days after then. I will show the global circulation and temperature distribution of each control test, and compare them to the relevant test in Chapter 3 to determine if the non-grey radiative transfer makes a significant difference. I will then plot the thermal emission and phase curves of each test at a higher spectral resolution than the calculations in the GCM. These plots will show how the global circulation affects the thermal emission, and how the phase curve depends strongly on the atmospheric opacity at which it is observed.

I will conclude that the realistic radiative transfer does not greatly affect the global circulation in each test, but does strongly affect the observed thermal phase curve. I will follow these control tests with a “best-fit” test based on similar tests in Chapter 3.

4.2.1 Global Circulation

All of the results in this section are time-averaged from 100 to 200 days. Figure 4.2 shows the temperature fields at the pressure level corresponding to the maximum zonal-mean zonal flow for Tests 1 and 2. Comparing to Figure 3.5 shows that these



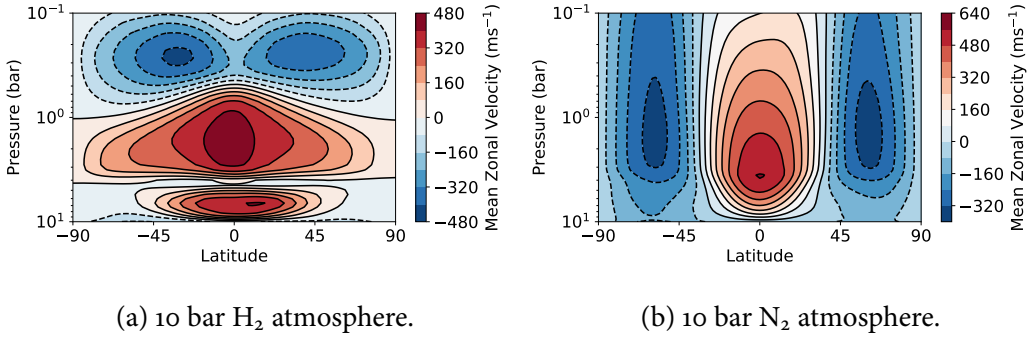
(a) Test 1: 10 bar H₂ atmosphere at the 3.57 bar pressure level.
(b) Test 2: 10 bar N₂ atmosphere at the 3.57 bar pressure level.

Figure 4.2: Global temperature maps of the simulations with 1% CO, at the pressure level corresponding to the maximum zonal-mean zonal velocity.

have a similar form to the equivalent tests with semi-grey radiation in Chapter 3 (Tests 1 and 2 in that chapter). As before, Test 2 has a large day-night contrast due to its high mean molecular weight and short radiative timescale. In contrast, Test 1 has a more zonally uniform temperature field due to its low mean molecular weight and long radiative timescale, which is also in agreement with the semi-grey tests. Chapter 2 explains why the radiative timescale affects the global temperature distribution in this way.

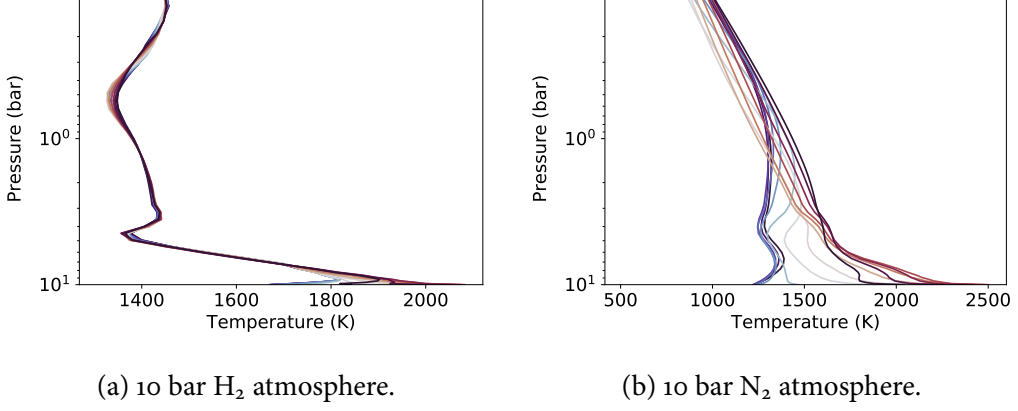
Figure 4.3 shows the zonal-mean zonal wind for Tests 1 and 2. Chapter 1 predicts that the more strongly damped Test 2 should have a strong pattern of eastward flow at the equator and westward flow at high latitudes, which matches the results here. It also predicts that the more weakly damped Test 1 should have weaker westward flow at high latitudes, which is correct. It is not clear why there are two eastward jets at the equator, which merits further investigation and comparison to the theory in Chapter 1.

Figure 4.4 shows temperature profiles of atmospheric columns in the model spaced evenly around the equators of Tests 1 and 2. Test 1 has almost uniform temperature around the equator apart from near the surface – this is due to the long radiative timescale compared to the timescale to redistribute heat around the planet. Test 2 has



(a) 10 bar H₂ atmosphere. (b) 10 bar N₂ atmosphere.

Figure 4.3: Zonal-mean zonal wind of the simulations with 1% CO.



(a) 10 bar H₂ atmosphere.

(b) 10 bar N₂ atmosphere.

Figure 4.4: Temperature profiles of the simulations with 1% CO.

a much shorter radiative timescale due to its higher mean molecular weight, so the profiles are very different depending on their position. These features of the profiles are consistent with the equivalent tests in Chapter 3.

The similarity of the global circulation and temperature structure of these tests to the corresponding tests in the previous chapter suggest that the more realistic radiative transfer does not strongly affect the atmospheric dynamics. The semi-grey model approximates the effect of CO absorption well – if a different gas with more extreme behaviour was used, the semi-grey model might not work so well. In summary, these control tests suggest that the scaling relations and conclusions of Chapter 3 still apply in this new model with more realistic radiative transfer.

4.2.2 Thermal Emission

The new radiative transfer scheme did not affect the global circulation greatly, but does affect the simulated observations due to the strong wavelength dependence. The plots in this section were produced by post-processing the final state of each test with a higher-resolution spectral file with 621 bands, and calculating hemisphere-averaged spectra and phase curves using the STARRY software ([Luger et al., 2019](#)).

Figure 4.5 shows the spectral radiance of the outgoing longwave radiation from columns evenly spaced around the equator at the substellar point, east terminator, antistar point, and west terminator, for Tests 1 and 2. Each spectrum show the three main CO absorption features in this range, at 2000, 4000, and 6000 cm^{-1} .

The differences between the OLR of both tests is due to their global circulation and heat distribution, as they both have the same surface pressure and concentration of 1% CO. There is less difference between the substellar and antistar OLR in Test 1 than in Test 2, due to their different day-night contrasts caused by the different radiative timescale discussed above. Test 1 has a substellar surface temperature of about 2300 K and an anti-stellar temperature of about 1800 K, while Test 2 has a substellar temperature of about 2500 K and an antistar temperature of about 1700 K.

The two tests also differ in the relative flux of their east and west terminators. Test 1 has more flux from its east terminator than its west, due to the eastward heat transport from the substellar point. Test 2, on the other hand, has more flux at its west terminator than its east, due to the weaker eastward heat transport in this case.

Figure 4.6 shows the emission spectra that would be observed for Tests 1 and 2, from the day-side and the night-side. The vertical dashed lines show the wavelengths of the phase curves plotted later in Figure 4.7, and the shaded region shows the extent of the 4.5 μm Spitzer bandpass used by [Demory et al. \(2016\)](#).

These are similar to the outgoing longwave radiation from individual columns

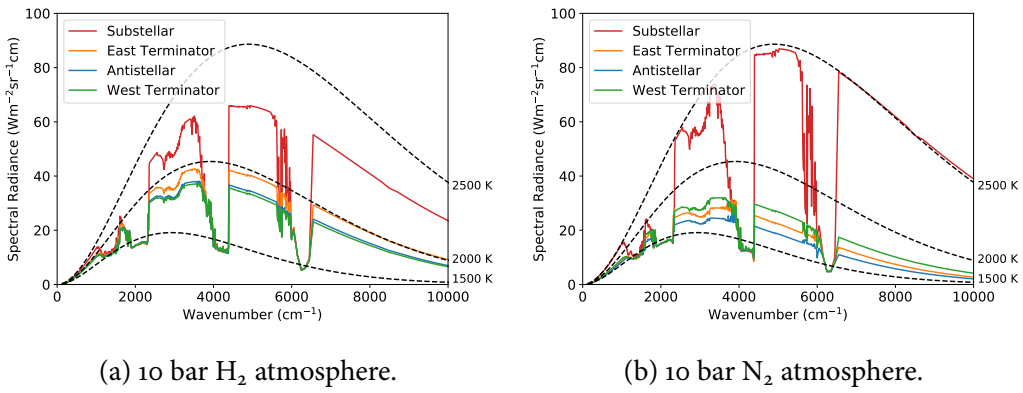


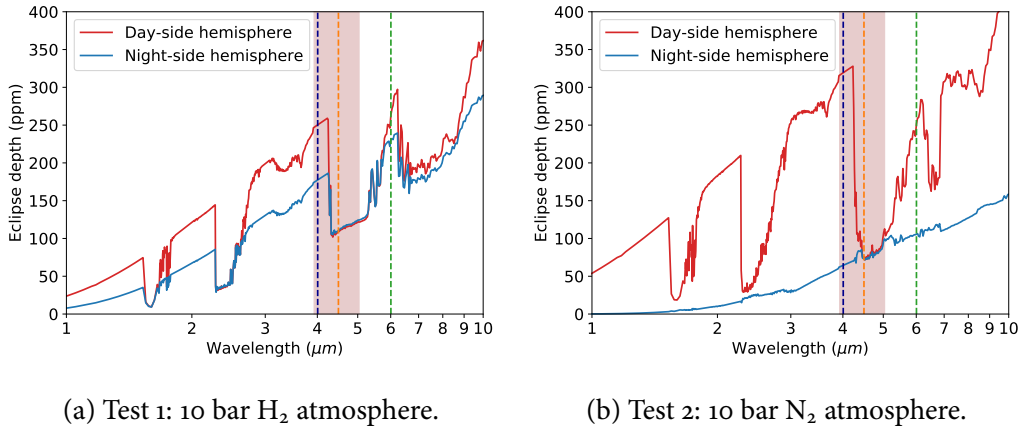
Figure 4.5: Spectral radiance of the outgoing longwave radiation (OLR) of Tests 1 and 2.

plotted in Figure 4.5, but are hemispherically averaged and converted into units of planetary flux divided by stellar flux. They show the same absorption features as Figure 4.5, with a clear day-night contrast that varies with wavelength in each test. Strong shortwave absorbers could produce an inversion that would give observable emission features. As before, Test 2 has a larger day-night contrast due to its short radiative timescale. The day-night contrast disappears in regions of high atmospheric opacity, as the upper atmosphere has almost homogeneous temperature in both cases.

These emission spectra at different phases contain a great deal of information about the three-dimensional thermal structure of the atmosphere. Stevenson et al. (2014) showed how emission spectroscopy at different phases can be used to reconstruct this structure, which may be possible for lava planets like 55 Cancri e using upcoming telescopes such as ARIEL (Tinetti et al., 2016).

4.2.3 Thermal Phase Curves

Figure 4.7 shows thermal phase curves at different wavelengths calculated from the output of Tests 1 and 2. Figure 3.1 showed how the phase curve is the hemisphere-integrated emission from the planet as a function of orbital phase. The thick black



(a) Test 1: 10 bar H_2 atmosphere.

(b) Test 2: 10 bar N_2 atmosphere.

Figure 4.6: Emission spectra of the day-side and night-side of Tests 1 and 2. The green, orange, and blue dashed lines show the wavelengths corresponding to the phase curves of the same colours in Figure 4.7.

line in Figure 4.7 is the phase curve measured by Demory et al. (2016), with a hot-spot shift of 41° east of the substellar point, and a day-night contrast of 1300 K (note that the observed phase curve contains dips due to the primary and secondary eclipses, unlike those calculated from the GCM results).

The coloured lines correspond to the phase curves that would be observed at the wavelengths shown by the dashed lines of the same colour in Figure 4.6. Their differences show that the phase curve depends strongly on the opacity of the atmosphere at the wavelengths observed. This effect is similar to the variation in the phase curves calculated at different radiating levels in Chapter 3. In both cases, a phase curve calculated at a low atmospheric opacity or low radiating level will have a large day-night contrast, and vice versa. There could be exceptions given a different thermal structure, such as an atmosphere dominated by shortwave heating where the maximum day-night contrast might be at a low pressure.

The thick red phase curve is weighted by the response function of the Spitzer 4.5 μm bandpass (from irsa.ipac.caltech.edu/data/SPITZER/docs/irac/calibrationfiles/spectralresponse/, and shaded in Figure 4.6). It simulates what would be observed in the channel used by Demory et al. (2016).

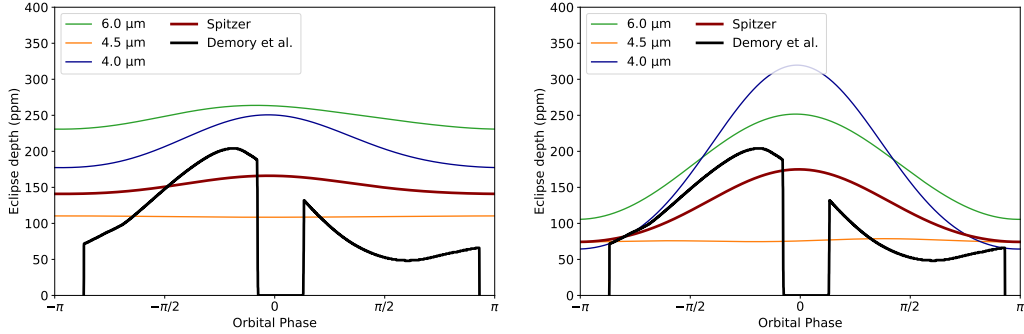
None of the phase curves have any significant phase offset, which would be interpreted observationally as showing no hot-spot shift away from the substellar point. This means that Test 2 is consistent with the equivalent 10 bar N₂ test in Chapter 3, which had no hot-spot shift or phase offset. However, it means that Test 1 is not consistent with the equivalent 10 bar H₂ test in Chapter 3, which had a large hot-spot shift in the temperature field. This is due first of all to the fact that the temperature field in Figure 4.2 is more zonally homogeneous than in the previous chapter. It also appears that the level of the jet, where there is some longitudinal variation of temperature), does not contribute greatly to the thermal emission, so this variation does not show up clearly. I will discuss this effect in more detail in the next section.

In both tests, the orange phase curve at 4.5 μm has very small amplitudes, due to the high atmospheric opacity at this wavelength. This means that the radiating level is at a very low pressure, which has almost homogenous temperature due to the strong atmospheric circulation. Both tests also have phase curves with very large amplitude in the blue 4.0 μm case. This is caused by the very low atmospheric opacity at this wavelength, so the phase curve corresponds to a high pressure, near the surface where the day-night contrast is large. The thick red phase curve of Test 2 matches the magnitude and amplitude of the observed phase curve, but not the hot-spot offset – just as in the previous chapter.

4.2.4 Summary of Control Tests

In conclusion, the control tests qualitatively matched both the global circulation and simulated observations of the corresponding tests in Chapter 3. This suggests that the exact form of the radiative transfer modelling is not vital to the large-scale circulation and associated observables such as broadband phase curves.

The phase curves were very sensitive to wavelength as expected from the investigation of the effect of the radiating level in Chapter 3. This produced some dif-



(a) Test 1: 10 bar H_2 atmosphere.

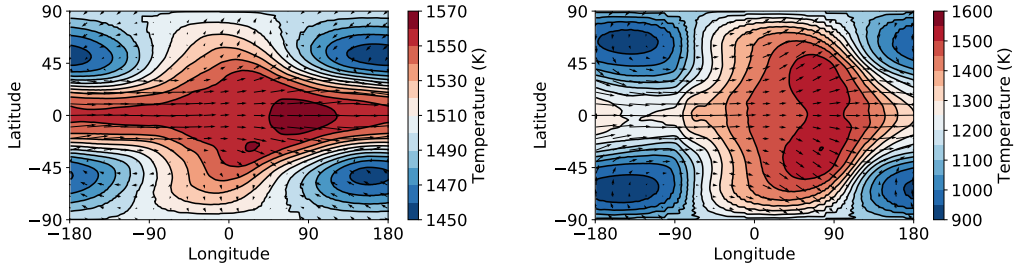
(b) Test 2: 10 bar N_2 atmosphere.

Figure 4.7: Thermal phase curves of the simulations with 1% CO. The thick black line shows the phase curve observed by Demory et al. (2016) in the Spitzer 4.5 μm channel. The thick red line is the phase curve simulated from each test using the same 4.5 μm bandpass. The other coloured lines show phase curves calculated at the representative wavelengths plotted in the same colours in Figure 4.6.

ferences between the phase curves in this chapter and those in the previous, as the strong wavelength dependence in this chapter produced a variety of phase curve amplitudes and magnitudes. Neither test exactly matched the phase curve measured by Demory et al. (2016), although the phase curve calculated in the Spitzer 4.5 μm bandpass of Test 2 did closely match the magnitude and amplitude of the observations – just not the hot-spot shift.

4.3 Best-Fit Simulation

As in the previous semi-grey tests, the 10 bar pure H_2 and N_2 tests did not match the observed thermal phase curve, having too little day-night contrast and too little hot-spot shift respectively. I therefore followed Chapter 3 and ran Test 3 with similar parameters to the previous “best-fit” test. Test 3 has a mixing ratio of 0.1 N_2 and 0.9 H_2 . Its other parameters are the same as the two control tests, with a mixing ratio of 0.01 CO and a 10 bar surface pressure. The results of Test 3 are plotted as a time-average from 200 to 400 days.



(a) Test 3: 10 bar mixed H₂-N₂ test at the 6.04 bar pressure level.
(b) Test 4: 100 bar N₂ test at the 28.3 bar pressure level.

Figure 4.8: Global temperature maps of tests 3 and 4 at the pressure level with the maximum zonal-mean zonal wind.

In this section, I will plot and discuss the global circulation of this test, and show how the scaling relations used previously still apply to this new model, and can predict an atmosphere with an intermediate amount of heat redistribution. However, I will show that any hot-spot shift in the temperature field does not show up in the thermal phase curves calculated from the outgoing longwave radiation. This will motivate the next test, which will have a thicker atmosphere capable of producing a phase offset in the thermal emission, not just the temperature field.

4.3.1 Global Circulation

Figure 4.8a shows the global temperature field at the pressure level of the maximum zonal-mean zonal velocity for Test 3. As in Test 4 in Chapter 3, it has both a significant hot-spot shift and day-night contrast due to its intermediate mean molecular weight. Figure 4.9a shows the zonal-mean zonal flow, where the primary zonal transport is due to the eastward jet. The zonal flow is consistent with the predictions of Chapter 1, as the westward flow at high latitudes is weaker than Test 2 but stronger than Test 1, as expected from the intermediate radiative damping timescale.

Figure 4.10a shows the temperature profiles around the equator of this test. They are more spread out than those of Test 1 and less spread out than those in Test 2, as ex-

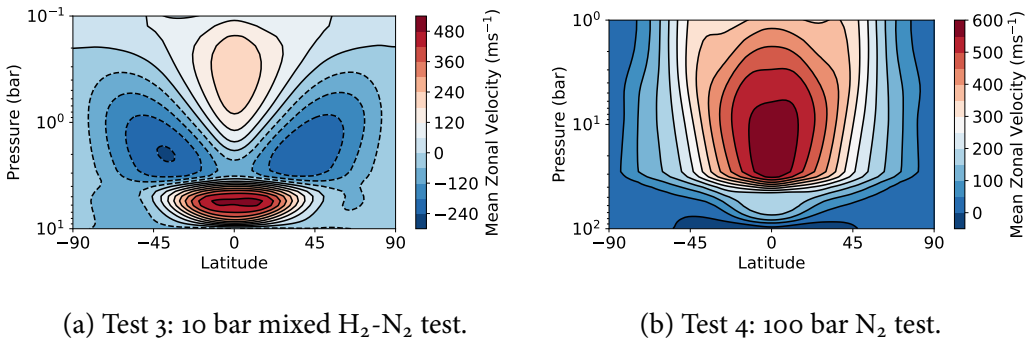


Figure 4.9: Zonal-mean zonal wind of tests 3 and 4.

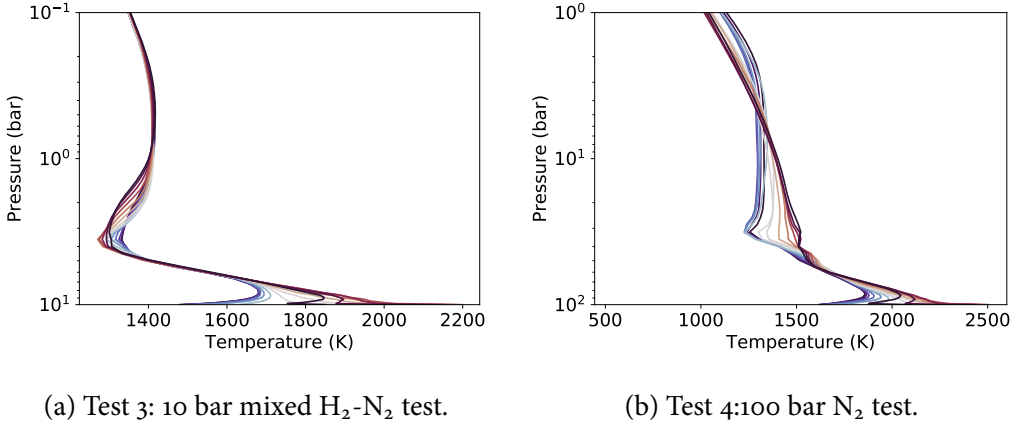
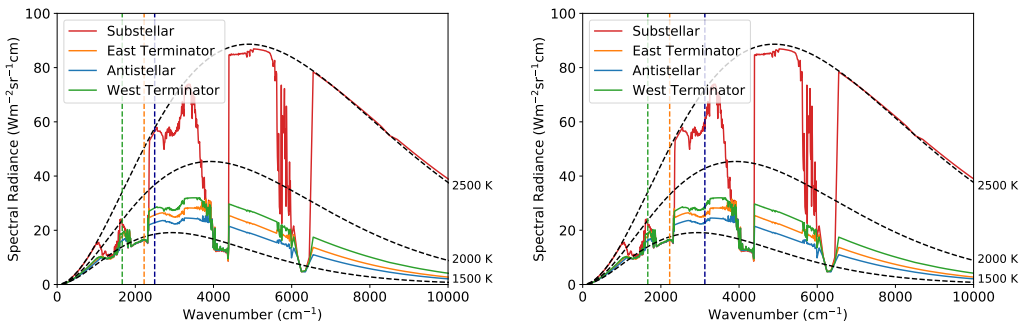


Figure 4.10: Temperature profiles around the equators of tests 3 and 4.

pected again from the intermediate radiative timescale. Overall, the global circulation is similar to the corresponding semi-grey test in Chapter 3.

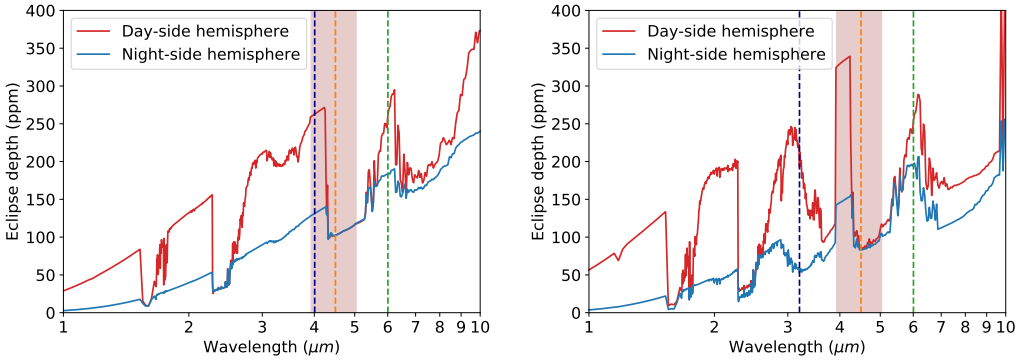
4.3.2 Thermal Emission

Figure 4.11a shows the outgoing longwave radiation from atmospheric columns spaced evenly around the equator of Test 3. The CO absorption features are present as in Tests 1 and 2, and their magnitude is greater than in Test 1 but smaller than in Test 2. This is because Test 2 has a larger day-night contrast, giving greater emission from the day-side surface and larger absorption features. Figure 4.12a shows the simulated emission spectrum of the day-side and night-side of this test. It is similar to the emission spectra of Tests 1 and 2, with the only real observable differences due to



(a) Test 3: 10 bar mixed $\text{H}_2\text{-N}_2$ atmosphere. (b) Test 4: 100 bar N_2 atmosphere.

Figure 4.11: Thermal OLR of tests 3 and 4.



(a) Test 3: 10 bar mixed $\text{H}_2\text{-N}_2$ atmosphere. (b) Test 4: 100 bar N_2 atmosphere.

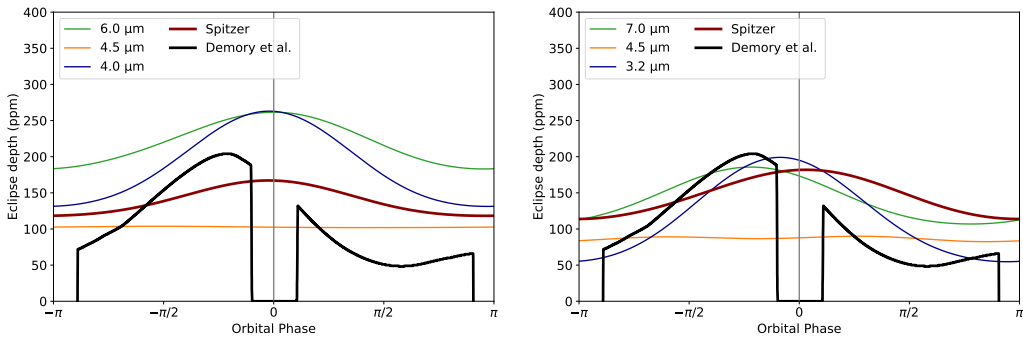
Figure 4.12: Thermal emission spectra of tests 3 and 4.

the temperature. Emission spectra at more phases might reveal differences due to a hot-spot shift in one test but not another.

4.3.3 Thermal Phase Curves

Figure 4.13a shows phase curves simulated from the thermal emission of Test 3 in the same wavelengths as in Figure 4.7. The corresponding test in the previous chapter produced the best-fitting phase curve to the observations of Demory et al. (2016). However, the phase curves of Test 3 in Figure 4.7 show no significant hot-spot shift despite the large hot-spot shift in the temperature field in Figure 4.8a.

The wavelengths of the phase curves cover a range of opacities so should cover a



(a) Test 3: 10 bar H_2 atmosphere.

(b) Test 4: 100 bar N_2 atmosphere.

Figure 4.13: Phase curves at different wavelengths and in the Spitzer bandpass of tests 3 and 4.

range of radiating levels. As expected, the phase curves corresponding to low atmospheric opacity have a large amplitude (day-night contrast) as they are dominated by emission from the surface. At higher opacities, the thermal emission is higher in the atmosphere so the phase curve amplitude is smaller. But there is no phase offset for the phase curve at intermediate opacity as might be expected.

So, why does the hot-spot shift in the temperature field not appear in these phase curves calculated from the outgoing longwave radiation? It appears that in these tests, for any opacity with significant emission from the level of the hot-spot shift, the emission from the surface is always stronger. It therefore dominates the contribution to the phase curve and masking the hot-spot shift. On Hot Jupiters, the hot-spot shift is visible in thermal phase curves as the jet often extends over a wide range of pressure levels and there is no significantly hotter surface to dominate the emission. I will discuss this in more detail in Section 4.5.

For now, I will suggest the hypothesis that it is not possible to observe a hot-spot shift on a tidally locked planet without a sufficiently thick atmosphere. In the next section I will test a 100 bar atmosphere on 55 Cancri e to determine if the hot-spot shift appears in its thermal phase curve.

4.4 100 bar Simulation

The main question arising from the simulations so far is how such a large hot-spot shift was observed by [Demory et al. \(2016\)](#), given the difficulty in recreating it from the simulated OLR. Test 3 has a hot-spot shift of up to 90° on the equator and seems well suited to show this in its thermal emission. However, the OLR is either dominated by at low opacities by the surface emission with no hot-spot shift, or at high opacities by the top-of-atmosphere emission.

What could produce an atmosphere with an observable hot-spot shift? The equatorial jet and hot-spot shift forms above the level of the thermal forcing. Therefore, the radiating level must correspond to the level of the hot-spot shift, with minimal contribution from the level of the thermal forcing. The main problem for these 10 bar atmospheres is that the outgoing radiation is always dominated by the thermal emission of the surface unless the opacity at the observed wavelength is very high. For very high opacity, the emission from the hot-spot shift may be very weak or be dominated by emission from the upper atmosphere.

So an observable shift requires a thicker atmosphere, with more longwave optical depth between the level of shortwave heating and the level of the jet. This is more like the atmosphere of a Hot Jupiter, where the jet is produced by shortwave heating of a range of levels, and the temperature increases less rapidly with depth than in the convective layer of the terrestrial atmospheres of this chapter. Hot Jupiters do indeed display hot-spot shifts in their observed and simulated phase curves ([Amundsen et al., 2016](#)).

In this section, I therefore show the results of Test 4, a 100 bar N_2 atmosphere with otherwise the same parameters as the previous tests. The increased surface pressure should give a longer radiative timescale, increasing the expected hot-spot shift compared to the 10 bar Test 2. I will discuss the global circulation and the simulated ob-

servations, and will show that a hot-spot shift is now apparent in the thermal phase curve at some wavelengths.

4.4.1 Global Circulation

The results of Test 4 are plotted as a time-average from 200 to 400 days. Figure 4.8b shows the global temperature map and winds at the pressure level of Test 4 where the equatorial jet is strongest. There is a large eastward hot-spot shift and large day-night contrast. The increased hot-spot shift compared to Test 2 in Figure 4.2 shows how the higher surface pressure has increased the radiative timescale.

Figure 4.9b shows the zonal-mean zonal wind of Test 4. It is more similar to the zonal wind of a Hot Jupiter simulation ([Showman et al., 2015](#)), with a deep equatorial jet produced mostly by shortwave rather than longwave heating. The prograde eastward flow at all latitudes at the level of the maximum equatorial jet speed is produced by the mechanism discussed in Chapter 1.

Figure 4.10b shows the temperature profiles around the equator of this test. They are similar to the temperature profiles of the other tests, but show higher temperatures at lower pressures on the day-side due to the increased effect of shortwave absorption.

4.4.2 Thermal Emission

Figure 4.11b shows the outgoing longwave radiation from columns spaced around the equator of Test 4. It shows the same absorption features as the other tests, although with deeper absorption features at regions of low opacity than the other tests due to the increased total atmospheric optical depth. Figure 4.12b shows the emission spectrum of the day-side and night-side of this test, and also shows deeper absorption features than the previous tests. The surface is warmer in this test than in Test 3,

due to the higher longwave optical depth of the atmosphere (which will be slightly offset by the increased shortwave optical depth).

In reality, it is probable that other absorbers and continuum absorption would provide non-zero opacity at all thermal wavelengths, so the regions of zero absorption here would not be seen. However, this idealised situation is useful for comparing the effect of different opacities on the thermal emission and phase curves.

4.4.3 Thermal Phase Curves

Figure 4.13b shows phase curves calculated at various wavelengths and in the Spitzer 4.5 μm bandpass for Test 4. Note that the wavelengths are different to those used in previous tests. The key result is that the green line at 7.0 μm shows a large phase offset, a feature that did not appear in any of the phase curves for the other tests in this section. This supports the hypothesis that a sufficiently thick atmosphere is required to observe a hot-spot shift in the phase curve.

The blue line at 3.2 μm shows a large day-night contrast that matches the observed day-night contrast of the black line. The contrast is relatively easy to match with simulations (as seen in all the previous tests), as it mostly increases monotonically with increasing radiative damping rate, or with decreasing opacity. The 4.5 μm phase curve has almost zero amplitude, as the opacity is too large. Even if there were a hot-spot shift it would not be visible due to the small amplitude of the phase curve.

The thick red line calculated using the Spitzer bandpass does not match the observations. Strong CO absorption only is not appropriate to give a mid-atmosphere radiating level – in reality, a more grey atmosphere like that of a Hot Jupiter with less variable opacity might be more appropriate. We could select a composition to match the radiating level and phase curve, but this would be somewhat artificial. The point of this modelling was to show that a thicker atmosphere is required for a hot-spot shift, which can then be observed at some appropriate wavelength. More observa-

tions such as emission spectra are needed to constrain the composition, which would allow for further modelling with more accurate parameters.

I therefore suggest that the observation of the hot-spot shift on 55 Cancri e is evidence for a thicker atmosphere than 10 bar. This is not inconsistent with the results of Chapter 3, where the scaling relations and GCM simulations suggested a maximum hot-spot shift and a best-fit atmosphere of around 10 bar. This was true – the physical hot-spot shift in temperature does benefit from an atmosphere that is not too thick. The key point is that this hot-spot shift will not show up in the outgoing thermal radiation for a 10 bar atmosphere, and so a thicker atmosphere is required.

4.5 Discussion

The first aim of this chapter was to compare the simulations using the new Socrates radiative transfer scheme to the previous semi-grey scheme, and confirm that the same scaling relations and qualitative global circulation applied. Tests 1, 2, and 3 qualitatively matched the corresponding tests in the previous chapter, suggesting that the scaling relations for hot-spot shift and day-night contrast are indeed generally applicable. Tests 1 and 2 showed either a hot-spot shift or day-night contrast in their temperature fields but not both, as in the previous chapter. Test 3 agreed with the previous chapter, showing a significant hot-spot shift and day-night contrast in its temperature field.

However, there was an important difference between the simulated thermal phase curves in this chapter and Chapter 3. Previously, the phase curves were calculated from the $4.5\text{ }\mu\text{m}$ flux emitted from a black-body radiating level chosen at various atmospheric pressure levels. This was necessary as the grey-gas radiative transfer does not represent the flux at particular wavelengths. This approximation meant that if a hot-spot shift appeared in the temperature field at a particular pressure level, it

had to appear in the thermal phase curve calculated using that level.

In this chapter the thermal phase curves are instead calculated directly from the Socrates radiative transfer scheme at specific wavelengths and in the Spitzer 4.5 μm bandpass. This means that a particular wavelength or band does not correspond to a single pressure level, and instead depends on the emission from the entire atmosphere. This is often dominated by a certain range of pressure levels, which is why the radiating level is a useful concept. However, in these tests the relatively low total surface pressure and the fact that the surface is always hotter than the atmosphere meant that the surface emission always dominated the emission of the level of the jet and hot-spot shift. This meant that a significant hot-spot shift did not appear in any of the phase curves of the tests with 10 bar surface pressure.

It is possible to explain this issue with a simple two-layer model of the surface and the pressure level of the hot-spot shift and jet. To observe the hot-spot shift, the flux from its level must be comparable to or greater than the flux from the surface. We assume that the jet forms one scale height above the surface, and assume that its temperature is $T_{jet} = e^{-1}T_{surf}$. Then if there is only one absorbing gas, the magnitudes of the OLR at a given wavelength λ from the jet and the surface are (Pierrehumbert, 2010):

$$OLR_{surf} = B_{surf}(T_{surf}, \lambda) e^{-\kappa w \rho_0 H}, \quad (4.1)$$

$$OLR_{jet} = B_{jet}(T_{jet}, \lambda) e^{-\kappa w \rho_0 H e^{-1}}, \quad (4.2)$$

where $B(T, \lambda)$ is the Planck function, κ is the opacity, w is the mixing ratio of the absorber, ρ_0 is the density at the surface and H is the scale height.

For a low opacity κ , the flux from the surface will dominate, and vice versa. The opacity must therefore be sufficiently high for the flux from the jet to dominate the

flux from the surface. However, if the opacity is too large then $e^{-\kappa w \rho_0 H e^{-1}}$ is too small and there is too little OLR to observe anything (or, it will be dominated by emission from the upper atmosphere above the jet). A hot-spot shift is therefore not observable on a terrestrial planet if the minimum opacity for the OLR from the jet to dominate the OLR from the surface is so large that the jet OLR is then too small to observe.

Setting the two fluxes equal gives the opacity at which they cross, and so the minimum opacity for the flux from the jet level to dominate:

$$B_{surf}(T_{surf}, \lambda) e^{-\kappa_{min} w \rho_0 H} = B_{jet}(T_{jet}, \lambda) e^{-\kappa_{min} w \rho_0 H e^{-1}} \quad (4.3)$$

$$\frac{T_{jet}^4}{T_{surf}^4} e^{-\kappa_{min} w \rho_0 H (e^{-1} - 1)} = 1 \quad (4.4)$$

As $T_{jet} = e^{-1} T_{surf}$,

$$\kappa_{min} w = \frac{4e}{\rho_0 H} \quad (4.5)$$

For a scale height $H = 1 \times 10^4$ m and a surface density of 1 kgm^{-1} , this gives a value of $\kappa_{min} w \approx 1 \times 10^{-3}$. This means that the OLR from the jet level is attenuated from the original Planck function by $e^{-\kappa_{min} w \rho_0 H e^{-1}} = e^{-4}$, or 1.83% of the original value, making it all but unobservable in relation to the upper atmosphere or other effects. So, in this model system of a terrestrial planet with a relatively thin atmosphere dominated by longwave heating from the surface, there is no wavelength or opacity at which we can observe a hot-spot shift. It is either dominated by the surface at low opacities, or attenuated to less than 1.83% when the opacity is high enough that the surface does not dominate.

However, hot-spot shifts are regularly seen in observations and simulations of

Hot Jupiters with thick atmospheres (Amundsen et al., 2016), meaning that the emission from the level of the jet is dominating the emission from the level of shortwave absorption below. This can be explained by two effects in the two-layer model above. First, the pressure (and therefore density) of the “surface” layer is greater, so ρ_o is greater in the above expressions and the emission from the surface is weaker relative to the emission from the jet. Second, the temperature increases less rapidly with pressure than in the terrestrial case, as the heating is due to shortwave absorption rather than longwave emission and convection due to the surface. These effects accounts for the difference between Tests 3 and 4, as in Figure 4.10 Test 4 has a warmer jet level relative to the surface, with greater longwave opacity between it and the surface.

The exact pressure required for there to be an appropriate atmospheric opacity jet emission to dominate the surface emission without being overly attenuated is not possible to define in general, and will vary with parameters like temperature or composition. The results in this chapter suggest that a hot-spot shift (or other atmospheric features) will appear in the thermal emission for a surface pressure of at least 10 to 100 bar. The two-layer model used here makes no assumptions about the equilibrium temperature or composition, so I suggest that this conclusion applies to a wide range of terrestrial planets.

This effect accounts for the difference between the 10 bar tests and the 100 bar Test 4, where a hot-spot shift only appeared in the thermal phase curve of the thicker atmosphere. These simulations therefore present a different conclusion to those in Chapter 3. Instead of a 5 bar atmosphere with a mean-molecular weight of 4.6 g mol^{-1} , they suggest that an atmosphere thicker than 10 bar is required, and that a heavier mean molecular weight may be required to compensate for the increased radiative timescale.

This conclusion does not contradict the work in Chapter 3. Chapter 3 used scaling relations and simulations to identify the largest day-side temperature, day-night

contrast and hot-spot shift possible in the temperature field of 55 Cancri e, as the radiative transfer could not accurately model the outgoing longwave radiation. This chapter, on the other hand, aimed to find the best-fitting phase curve at a particular wavelength. This required a higher surface pressure, which reduced the fit of the mid-atmosphere temperature field to the observations, but matched the phase curve better in the more realistic simulated observations.

It is important to point out that the 100 bar atmosphere did not match the observations in the Spitzer bandpass. This shows that an atmosphere with its opacity dominated by CO is not a good match to the observations. It would not be difficult to tune the composition and opacity of the atmosphere to make the radiating level match the observations, but this would be an artificial exercise. The important result of this chapter is that it is possible to match the observed phase curve in the thermal emission, given an appropriate opacity and thick enough atmosphere.

These simulations also displayed variability similar to that discussed in Chapter 3 ([Pierrehumbert and Hammond, 2018](#)). As in that chapter, it is possible that this means that the observed phase curve corresponds to a period of increased hot-spot shift or day-night contrast, and that the difficulties in fitting a time-mean result are just because the real time-mean atmosphere does not have such an extreme temperature distribution.

It is also possible that processes such as condensable transport or cloud formation are responsible for a more complex climate, or variability in the thermal emission ([Parmentier et al., 2013](#)) . Studies such as [Parmentier et al. \(2016\)](#) and [Lines et al. \(2018\)](#) have shown the strong effect that cloud formation can have on the emitted and reflected radiation. I am supporting Graham Lee in a project to use the DIHRT cloud formation and transport code in simulations similar to those in this chapter. The results showed how a wide variety of clouds could form with a correspondingly varied number of effects on the radiative transfer on the atmosphere. The simulations

were very sensitive to the allowed species and the species outgassed from the surface, so have not yet produced any definite conclusions about the effect of clouds on the climate and thermal phase curve of 55 Cancri e.

4.6 Conclusions

In this chapter, I used a newer version of Exo-FMS with an updated dynamical core and correlated-k radiative transfer to follow up the simulations in the previous chapter. The global circulation and temperature distribution of these simulations qualitatively matched the grey-gas simulations in the older version of Exo-FMS. However, the thermal phase curves calculated with the more realistic radiative transfer did not match the observations in the 10 bar tests, as the thermal emission was dominated by the surface where the hot-spot shift is small.

This suggested that a thicker atmosphere comparable to that of a Hot Jupiter was required. I simulated another test with a surface pressure of 100 bar, and showed that the hot-spot shift now appeared at some wavelengths. I showed why this higher pressure is required with a simple estimate of the emission from the jet level and the surface. This suggests that it may not be possible to observe dynamical features such as hot-spot shifts in thermal phase curves of terrestrial planets with atmospheres thinner than about 10 bar. This may mean that the phase curve measured by Kreidberg et al. (2019) is not yet evidence for the lack of an atmosphere.

I conclude that the more realistic radiative transfer does not easily explain the observed thermal phase curve of 55 Cancri e. The scaling relations of Zhang and Showman (2017) still apply, so the phase curve still implies a mean molecular weight heavier than H₂. These simulations imply a thick atmosphere on 55 Cancri e.

Conclusions

This thesis aimed to understand the atmospheric circulation and global temperature distribution of tidally locked planets, with the goal of interpreting the thermal phase curve of 55 Cancri e. The first two chapters addressed the formation and effect of the atmospheric dynamics, and the last two chapters simulated the atmosphere of this planet and compared the results to observations.

In Chapter 1 I focused on the formation of the zonal flow that is so important to this global circulation. I showed that the Gierasch-Rossow-Williams mechanism can be applied to tidally locked planets, and demonstrated that the same balance of momentum fluxes applies in a hierarchy of models. This gave an improved understanding of the momentum budget and equilibrium state of these atmospheres. It would be useful to follow up this work by applying this mechanism and balance to predict scaling relations for observables.

Chapter 2 used this prediction of the zonal flow to explain the global temperature distribution seen in simulations and observations of the atmospheres of these planets. I linearised a shallow-water model on an equatorial beta-plane around an equatorial jet and its associated height perturbation. The resulting response to day-night forcing matched GCM simulations well. This showed that the hot-spot shift was formed by a superposition of the Doppler shifted maximum of the response, and the zonally uniform height perturbation in geostropic balance with the imposed equatorial jet.

I then applied the theory of the first two chapters to the problem of a real planet. Chapter 3 aimed to interpret a thermal phase curve measured of the lava planet 55 Cancri e, by comparing it to a suite of GCM simulations with different bulk atmospheric parameters. I selected the parameters based on one-dimensional scaling relations for the expected hot-spot shift and day-night contrast. These scaling relations described the GCM results qualitatively, although were not exact enough to match the observations perfectly. The simulations could match either the observed hot-spot shift given a low molecular weight atmosphere and a high surface pressure, or the observed day-night contrast given a high molecular weight atmosphere and a low surface pressure. The “best-fit” simulation selected using the scaling relations had a hot-spot shift of 25° east compared to the observed value of 41° . I suggested that a more realistic model of the climate and the outgoing radiation could be needed to match the observations. Cloud formation on the night-side may also be important in reality, which would raise the thermal radiating level of the night-side and lower the apparent temperature, possibly explaining the difference between the simulations and observations.

In Chapter 4, I used an improved model of 55 Cancri e based on the suggestions in Chapter 3. The main developments were the coupling to a correlated-k radiative transfer scheme Socrates, and the upgrade to a newer dynamical core on a cubed-sphere grid. This new core and grid gave more stable simulations that ran faster. The radiative transfer scheme Socrates allowed for modelling of specific gaseous absorbers in the atmosphere, as well as spectrally resolved outgoing longwave radiation. This allowed phase curves to be calculated at specific wavelengths and in the $4.5\text{ }\mu\text{m}$ bandpass used in the observed phase curve. I showed that the global circulation of the tests with the same bulk parameters as in Chapter 3, suggesting that the more realistic radiative transfer was approximated well by the semi-grey model. However, the phase curves calculated with the new model did not match the phase

curves calculated via radiating level in Chapter 3. I suggested that a sufficiently thick atmosphere is required for the hot-spot shift in the temperature field to appear in the thermal phase curve, and demonstrated this with a 100 bar test and a simple two-layer model. I concluded that the phase curve of [Demory et al. \(2016\)](#) is evidence for an atmosphere with surface pressure significantly larger than than 10 bar and a mean molecular weight greater than that of H₂.

These chapters addressed the initial question step by step, from the formation of the zonal flow on a tidally locked planet to the implications of observations of its thermal emission. The first two chapters provided a mechanism for the formation of the zonal flow and hot-spot shift on a tidally locked planet They demonstrated that the hot-spot shift is a result of wave-mean flow interactions and has a clear structure, rather than being the result of eastward heat advection. The last two chapters showed that an atmosphere on 55 Cancri e can give a broadly similar temperature distribution to that reconstructed by [Demory et al. \(2016\)](#). They concluded that the phase curve is evidence for an atmosphere of surface pressure significantly larger than than 10 bar and a mean molecular weight greater than that of H₂.

The next step in this work will be to apply the theory to more useful situations, using the shallow-water model to predict equilibrium states of tidally locked atmospheres and the resulting temperature distribution expected. The shallow-water models also predict non-stationary stable and unstable modes to be possible on these planets, similar to the variability seen in simulations ([Pierrehumbert and Hammond, 2018](#)) or obsrvations ([Demory et al., 2015; Armstrong et al., 2017](#)). Investigating the behaviour of potentially very strong atmospheric transience might give a whole new window into these atmospheres. Finally, more detailed and accurate modelling of processes such as radiative transfer and cloud formation may help GCM simulations to better fit observed spectra and phase curve/

The study of exoplanetary atmospheres is still very young, and has allowed the

work in this thesis to be touched by a great range of stimulating ideas, techniques, and (occasional) real data. I hope that the huge potential for exoplanetary science to contribute to atmospheric and planetary science can be realised, and that there are many more surprises to come.

Bibliography

- Amundsen, D.S. et al. The uk met office global circulation model with a sophisticated radiation scheme applied to the hot jupiter hd 209458b. *Astronomy & Astrophysics*, 595:A36, 2016.
- Angelo, I. and Hu, R. A Case for an Atmosphere on Super-Earth 55 Cancri e. *The Astronomical Journal*, 154(6):232, Dec. 2017.
- Arcangeli, J. et al. Climate of an ultra hot Jupiter-Spectroscopic phase curve of WASP-18b with HST/WFC3. *Astronomy & Astrophysics*, 625:A136, 2019.
- Armstrong, D.J. et al. Variability in the atmosphere of the hot giant planet hat-p-7 b. *Nature Astronomy*, 1(1):0004, 2017.
- Barnes, R. Tidal locking of habitable exoplanets. *Celestial Mechanics and Dynamical Astronomy*, 129(4):509–536, 2017.
- Boutle, I.A. et al. Exploring the climate of Proxima B with the Met Office Unified Model. *Astronomy & Astrophysics*, 601:A120, May 2017.
- Boyd, J.P. The Effects of Latitudinal Shear on Equatorial Waves. Part I: Theory and Methods. *Journal of Atmospheric Sciences*, 35(1):2236–2258, Dec. 1978.
- Boyd, J.P. *Chebyshev & Fourier Spectral Methods*. Springer, 2000.
- Brogi, M. et al. Rotation and winds of exoplanet hd 189733 b measured with high-dispersion transmission spectroscopy. *The Astrophysical Journal*, 817(2):106, 2016.
- Carone, L., Keppens, R. and Decin, L. Connecting the dots: a versatile model for the atmospheres of tidally locked Super-Earths. *Monthly Notices of the Royal Astronomical Society*, 445(1):930–945, Sept. 2014.
- Carone, L., Keppens, R. and Decin, L. Connecting the dots - II. Phase changes in the climate dynamics of tidally locked terrestrial exoplanets. *Monthly Notices of the Royal Astronomical Society*, 453(3):2412–2437, Nov. 2015.
- Charnay, B., Meadows, V. and Leconte, J. 3D Modeling of GJ1214b's Atmosphere: Vertical Mixing Driven by an Anti-Hadley Circulation. *The Astrophysical Journal*, 813(1):15, Nov. 2015.

- Cho, J.K., Polichtchouk, I. and Thrastarson, H.T. Sensitivity and variability redux in hot-jupiter flow simulations. *Monthly Notices of the Royal Astronomical Society*, 454(4):3423–3431, 2015.
- Courant, R., Friedrichs, K. and Lewy, H. Über die partiellen differenzengleichungen der mathematischen physik. *Mathematische annalen*, 100(1):32–74, 1928.
- Cowan, N.B. and Agol, E. Inverting phase functions to map exoplanets. *The Astrophysical Journal Letters*, 678(2):L129, 2008.
- Cowan, N.B. and Agol, E. The statistics of albedo and heat recirculation on hot exoplanets. *The Astrophysical Journal*, 729(1):54, 2011.
- Crida, A. et al. Mass, radius, and composition of the transiting planet 55 cnc e: using interferometry and correlations. *The Astrophysical Journal*, 860(2):122, 2018.
- Dawson, R.I. and Fabrycky, D.C. Radial velocity planets de-aliased: a new, short period for super-Earth 55 Cnc e. *The Astrophysical Journal*, 722(1):937, 2010.
- Demory, B.O. et al. Detection of a transit of the super-Earth 55 Cancri e with warm Spitzer. *Astronomy & Astrophysics*, 533:A114, Sept. 2011.
- Demory, B.O. et al. Variability in the super-earth 55 cnc e. *Monthly Notices of the Royal Astronomical Society*, 455(2):2018–2027, 2015.
- Demory, B.O. et al. A map of the large day–night temperature gradient of a super-Earth exoplanet. *Nature*, 532(7598):207–209, Mar. 2016.
- Ding, F. and Pierrehumbert, R.T. Convection in condensable-rich atmospheres. *The Astrophysical Journal*, 822(1):24, 2016.
- Dorn, C. et al. A new class of super-earths formed from high-temperature condensates: Hd219134 b, 55 cnc e, wasp-47 e. *Monthly Notices of the Royal Astronomical Society*, 484(1):712–727, 2018.
- Dragomir, D. et al. New most† photometry of the 55 cancri system. *Proceedings of the International Astronomical Union*, 8(S293):52–57, 2012.
- Drummond, B. et al. Observable signatures of wind-driven chemistry with a fully consistent three-dimensional radiative hydrodynamics model of hd 209458b. *The Astrophysical Journal Letters*, 855(2):L31, 2018.
- Edwards, J.M. and Slingo, A. Studies with a flexible new radiation code. I: Choosing a configuration for a large-scale model. *Quarterly Journal of the Royal ...*, 1996.
- Gillon, M. et al. Improved precision on the radius of the nearby super-earth 55 cnc e. *Astronomy & Astrophysics*, 539:A28, 2012.
- Goldreich, P. and Soter, S. Q in the Solar System. *Icarus*, 5(1-6):375–389, 1966.

- Hammond, M. and Pierrehumbert, R.T. Linking the Climate and Thermal Phase Curve of 55 Cancri e. *The Astrophysical Journal*, 849(2):152, Nov. 2017.
- Hammond, M. and Pierrehumbert, R.T. Wave-Mean Flow Interactions in the Atmospheric Circulation of Tidally Locked Planets. *The Astrophysical Journal*, 869(1):65, Dec. 2018.
- Held, I.M. and Hou, A.Y. Nonlinear axially symmetric circulations in a nearly inviscid atmosphere. *Journal of the Atmospheric Sciences*, 37(3):515–533, 1980.
- Held, I.M. and Suarez, M.J. A proposal for the intercomparison of the dynamical cores of atmospheric general circulation models. *Bulletin of the american Meteorological society*, 75(10):1825–1830, 1994.
- Heng, K. and Showman, A.P. Atmospheric Dynamics of Hot Exoplanets. *Annual Review of Earth and Planetary Sciences*, 43(1):509–540, May 2015.
- Heng, K. and Workman, J. Analytical models of exoplanetary atmospheres. I. Atmospheric dynamics via the shallow water system. *Astrophysical Journal, Supplement Series*, 213(2):27, Aug. 2014.
- Heng, K., Frierson, D.M.W. and Phillipps, P.J. Atmospheric circulation of tidally locked exoplanets: II. Dual-band radiative transfer and convective adjustment. *Monthly Notices of the Royal Astronomical Society*, 418(4):2669–2696, Oct. 2011.
- Hide, R. Dynamics of the atmospheres of the major planets with an appendix on the viscous boundary layer at the rigid bounding surface of an electrically-conducting rotating fluid in the presence of a magnetic field. *Journal of the Atmospheric Sciences*, 26(5):841–853, 1969.
- Iga, S.I. and Matsuda, Y. Shear Instability in a Shallow Water Model with Implications for the Venus Atmosphere. *Journal of Atmospheric Sciences*, 62(7):2514–2527, July 2005.
- Ito, Y. et al. Theoretical emission spectra of atmospheres of hot rocky super-earths. *The Astrophysical Journal*, 801(2):144, 2015.
- Joshi, M., Haberle, R. and Reynolds, R. Simulations of the atmospheres of synchronously rotating terrestrial planets orbiting m dwarfs: conditions for atmospheric collapse and the implications for habitability. *Icarus*, 129(2):450–465, 1997.
- Kataria, T. et al. The Atmospheric Circulation of the Super Earth GJ 1214b: Dependence on Composition and Metallicity. *The Astrophysical Journal*, 785(2):92, Apr. 2014.
- Kataria, T. et al. The atmospheric circulation of the hot jupiter wasp-43b: Comparing three-dimensional models to spectrophotometric data. *The Astrophysical Journal*, 801(2):86, 2015.

- Koll, D.D.B. and Abbot, D.S. Deciphering thermal phase curves of dry, tidally locked terrestrial planets. *The Astrophysical Journal*, 802(1):21, Mar. 2015.
- Koll, D.D.B. and Abbot, D.S. Temperature Structure and Atmospheric Circulation of Dry Tidally Locked Rocky Exoplanets. *The Astrophysical Journal*, 825(2):99, July 2016.
- Komacek, T.D. and Showman, A.P. Atmospheric Circulation of Hot Jupiters: Dayside-Nightside Temperature Differences. *The Astrophysical Journal*, 821(1):16, Apr. 2016.
- Komacek, T.D., Showman, A.P. and Tan, X. Atmospheric Circulation of Hot Jupiters: Dayside-Nightside Temperature Differences. II. Comparison with Observations. *The Astrophysical Journal*, 835(2):198, Feb. 2017.
- Kreidberg, L. et al. Absence of a thick atmosphere on the terrestrial exoplanet LHS 3844b. *Nature*, 2019.
- Laraia, A.L. and Schneider, T. Superrotation in terrestrial atmospheres. *Journal of the Atmospheric Sciences*, 72(11):4281–4296, 2015.
- Leconte, J. et al. Asynchronous rotation of earth-mass planets in the habitable zone of lower-mass stars. *Science*, 347(6222):632–635, 2015.
- Lin, S.J. A “Vertically Lagrangian” Finite-Volume Dynamical Core for Global Models. *Monthly Weather Review*, 132(10):2293–, 2004.
- Lines, S. et al. Simulating the cloudy atmospheres of hd 209458 b and hd 189733 b with the 3d met office unified model. *Astronomy & Astrophysics*, 615:A97, 2018.
- Liu, B. and Showman, A.P. Atmospheric circulation of hot jupiters: insensitivity to initial conditions. *The Astrophysical Journal*, 770(1):42, 2013.
- Longuet-Higgins, M.S. The eigenfunctions of laplace’s tidal equation over a sphere. *Philosophical Transactions of the Royal Society of London. Series A, Mathematical and Physical Sciences*, 262(1132):511–607, 1968.
- Louden, T. and Wheatley, P.J. Spatially resolved eastward winds and rotation of hd 189733b. *The Astrophysical Journal Letters*, 814(2):L24, 2015.
- Luger, R. et al. Starry: Analytic occultation light curves. *The Astronomical Journal*, 157(2):64, 2019.
- Lutsko, N.J. The response of an idealized atmosphere to localized tropical heating: Superrotation and the breakdown of linear theory. *Journal of the Atmospheric Sciences*, 75(1):3–20, 2018.
- Madhusudhan, N., Lee, K.K. and Mousis, O. A possible carbon-rich interior in super-earth 55 cancri e. *The Astrophysical Journal Letters*, 759(2):L40, 2012.

- Madhusudhan, N. et al. Exoplanetary atmospheres—chemistry, formation conditions, and habitability. *Space science reviews*, 205(1-4):285–348, 2016.
- Majeau, C., Agol, E. and Cowan, N.B. A two-dimensional infrared map of the extra-solar planet hd 189733b. *The Astrophysical Journal Letters*, 747(2):L20, 2012.
- Matsuno, T. Quasi-Geostrophic Motions in the Equatorial Area. *Journal of the Meteorological Society of Japan Ser II*, 44(1):25–43, 1966.
- Mayne, N.J. et al. The unified model, a fully-compressible, non-hydrostatic, deep atmosphere global circulation model, applied to hot jupiters-endgame for a hd 209458b test case. *Astronomy & Astrophysics*, 561:A1, 2014.
- Mayne, N.J. et al. Results from a set of three-dimensional numerical experiments of a hot Jupiter atmosphere. *Astronomy & Astrophysics*, 604:A79, Aug. 2017.
- McArthur, B.E. et al. Detection of a Neptune-mass planet in the ρ_1 Cancri system using the Hobby-Eberly Telescope. *The Astrophysical Journal Letters*, 614(1):L81, 2004.
- Mendonça, J.M. et al. Thor: a new and flexible global circulation model to explore planetary atmospheres. *The Astrophysical Journal*, 829(2):115, 2016.
- Mendonça, J.M. et al. Revisiting the phase curves of wasp-43b: Confronting re-analyzed spitzer data with cloudy atmospheres. *The Astronomical Journal*, 155(4):150, 2018.
- Menou, K. Magnetic scaling laws for the atmospheres of hot giant exoplanets. *The Astrophysical Journal*, 745(2):138, 2012.
- Merlis, T.M. and Schneider, T. Atmospheric dynamics of Earth-like tidally locked aquaplanets. *Journal of Advances in Modeling Earth Systems*, 2(4):13–n/a, Dec. 2010.
- Miguel, Y. Observability of molecular species in a nitrogen dominated atmosphere for 55 cancri e. *Monthly Notices of the Royal Astronomical Society*, 482(3):2893–2901, 2018.
- Miguel, Y. et al. Compositions of hot super-earth atmospheres: exploring kepler candidates. *The Astrophysical Journal Letters*, 742(2):L19, 2011.
- Moses, J.I. Chemical kinetics on extrasolar planets. *Philosophical Transactions of the Royal Society A: Mathematical, Physical and Engineering Sciences*, 372(2014):20130073, 2014.
- Noda, S. et al. The circulation pattern and day-night heat transport in the atmosphere of a synchronously rotating aquaplanet: Dependence on planetary rotation rate. *Icarus*, 282:1–18, Jan. 2017.

- Norton, W. Tropical wave driving of the annual cycle in tropical tropopause temperatures. Part II: Model results. *Journal of the atmospheric sciences*, 63(5):1420–1431, 2006.
- Parmentier, V. and Crossfield, I.J.M. Exoplanet Phase Curves: Observations and Theory. *Handbook of Exoplanets*, 564(7):116–22, 2017.
- Parmentier, V., Showman, A.P. and Lian, Y. 3d mixing in hot jupiters atmospheres-i. application to the day/night cold trap in hd 209458b. *Astronomy & Astrophysics*, 558:A91, 2013.
- Parmentier, V. et al. Transitions in the Cloud Composition of Hot Jupiters. *The Astrophysical Journal*, 828(1):22, Sept. 2016.
- Pierrehumbert, R. and Gaidos, E. Hydrogen Greenhouse Planets Beyond the Habitable Zone. *The Astrophysical Journal Letters*, 734(1):L13, June 2011.
- Pierrehumbert, R.T. *Principles of Planetary Climate*. Cambridge University Press, 2010.
- Pierrehumbert, R.T. and Ding, F. Dynamics of atmospheres with a non-dilute condensable component. *Proceedings of the Royal Society A: Mathematical, Physical and Engineering Sciences*, 472(2190):20160107, 2016.
- Pierrehumbert, R.T. and Hammond, M. Atmospheric circulation of tide-locked exoplanets. *Annual Reviews, Submitted*, 2018.
- Polichtchouk, I. et al. Intercomparison of general circulation models for hot extra-solar planets. *Icarus*, 229:355–377, 2014.
- Putman, W.M. and Lin, S.J. Finite-volume transport on various cubed-sphere grids. *Journal of Computational Physics*, 227(1):55–78, Nov. 2007.
- Read, P. Super-rotation and diffusion of axial angular momentum: II. A review of quasi-axisymmetric models of planetary atmospheres. *Quarterly Journal of the Royal Meteorological Society*, 112(471):253–272, 1986.
- Read, P.L. and Lebonnois, S. Superrotation on venus, on titan, and elsewhere. *Annual Review of Earth and Planetary Sciences*, 46:175–202, 2018.
- Ribstein, B., Zeitlin, V. and Tissier, A.S. Barotropic, baroclinic, and inertial instabilities of the easterly Gaussian jet on the equatorial β -plane in rotating shallow water model. *Physics of Fluids*, 26(5):056605, May 2014.
- Rothman, L. et al. Hitemp, the high-temperature molecular spectroscopic database. *Journal of Quantitative Spectroscopy and Radiative Transfer*, 111(15):2139–2150, 2010.

- Shell, K.M. and Held, I.M. Abrupt Transition to Strong Superrotation in an Axisymmetric Model of the Upper Troposphere. *Journal of Atmospheric Sciences*, 61(2): 2928–2935, Dec. 2004.
- Showman, A.P. and Guillot, T. Atmospheric circulation and tides of “51 pegasus b-like” planets. *Astronomy & Astrophysics*, 385(1):166–180, 2002.
- Showman, A.P. and Polvani, L.M. The Matsuno-Gill model and equatorial superrotation. *Geophysical Research Letters*, 37(1):L18811–n/a, Sept. 2010.
- Showman, A.P. and Polvani, L.M. Equatorial Superrotation on Tidally Locked Exoplanets. *The Astrophysical Journal*, 738(1):71, Sept. 2011.
- Showman, A.P., Lewis, N.K. and Fortney, J.J. Three-dimensional atmospheric circulation of warm and hot jupiters: Effects of orbital distance, rotation period, and nonsynchronous rotation. *Astrophysical Journal*, 801(2):95, Mar. 2015.
- Stevenson, K.B. et al. Thermal structure of an exoplanet atmosphere from phase-resolved emission spectroscopy. *Science*, 346(6211):838–841, 2014.
- Sugimoto, N., Takagi, M. and Matsuda, Y. Fully developed superrotation driven by the mean meridional circulation in a venus gcm. *Geophysical Research Letters*, 46 (3):1776–1784, 2019.
- Thrastarson, H.T. and Cho, J.Y. Effects of initial flow on close-in planet atmospheric circulation. *The Astrophysical Journal*, 716(1):144, 2010.
- Thuburn, J. and Lagneau, V. Eulerian Mean, Contour Integral, and Finite-Amplitude Wave Activity Diagnostics Applied to a Single-Layer Model of the Winter Stratosphere. *Journal of Atmospheric Sciences*, 56(5):689–710, Mar. 1999.
- Tinetti, G. et al. The science of ARIEL (Atmospheric Remote-sensing Infrared Exoplanet Large-survey). In MacEwen, H.A. et al, editors, *Proceedings of the SPIE*, page 99041X. Univ. College London (United Kingdom), SPIE, July 2016.
- Tsai, S.M., Dobbs-Dixon, I. and Gu, P.G. Three-dimensional structures of equatorial waves and the resulting super-rotation in the atmosphere of a tidally locked hot Jupiter. *Astrophysical Journal*, 793(2):141, Oct. 2014.
- Tsiaras, A. et al. Detection of an atmosphere around the super-earth 55 cancri e. *The Astrophysical Journal*, 820(2):99, 2016.
- Von Braun, K. et al. 55 cancri: Stellar astrophysical parameters, a planet in the habitable zone, and implications for the radius of a transiting super-earth. *The Astrophysical Journal*, 740(1):49, 2011.
- Wang, H., Boyd, J.P. and Akmaev, R.A. On computation of Hough functions. *Geoscientific Model Development*, 9(4):1477–1488, Apr. 2016.

- Wang, P. and Mitchell, J.L. Planetary ageostrophic instability leads to superrotation. *Geophysical Research Letters*, 41(12):4118–4126, 2014.
- Weinbaum, S.G. The Lotus Eaters. *Astounding Stories*, 15(2):52–71, 1935.
- Wetzel, S. et al. Laboratory measurement of optical constants of solid sio and application to circumstellar dust. *Astronomy & Astrophysics*, 553:A92, 2013.
- Winn, J.N. et al. A Super-Earth Transiting a Naked-Eye Star . *The Astrophysical Journal*, 737(1):L18, Aug. 2011a.
- Winn, J.N. et al. A super-earth transiting a naked-eye star. *The Astrophysical Journal Letters*, 737(1):L18, 2011b.
- Zhang, X. and Showman, A.P. Effects of Bulk Composition on the Atmospheric Dynamics on Close-in Exoplanets. *The Astrophysical Journal*, 836(1):73, Feb. 2017.

APPENDIX A

Exo-FMS

A General Circulation Model (GCM) simulates the fluid dynamics of an atmosphere or ocean, coupled to other models of physical processes such as radiative transfer or convection. GCMs are valuable tools for investigating the atmospheric dynamics of new types of planet, as they can simulate a great variety of planetary atmospheres without prior knowledge of what should happen. In this appendix, I will review the structure and functionality of the GCM “Exo-FMS” that I used to model planetary atmospheres in this thesis.

Exo-FMS is hosted at <https://github.com/OxfordPlanetaryClimate>, and will be made public soon.

A.1 Structure

Exo-FMS is intended to have a simple structure with as few changes as possible to the original code release of the cubed-sphere dynamical core (<https://www.gfdl.noaa.gov/cubed-sphere-quickstart/>). In this section, I will give an overview of the modelling structure “FMS”, and the interface that I built between the dynamical core and the modules for different physical processes.

A.1.1 FMS

Exo-FMS is built on the GFDL “Flexible Modelling System” (FMS), which is a “software framework for supporting the efficient development, construction, execution, and scientific interpretation of atmospheric, oceanic, and climate system models” (<https://www.gfdl.noaa.gov/fms/>). In the context of Exo-FMS, FMS is the framework of the model, handling the compiling and running of the model, data input and output, parallelization via MPI, and many utilities such as time-keeping or initialisation.

A.1.2 Physics Interface

Exo-FMS is based on a single interface between the dynamical core and the physics modules. I produced this interface to simplify the addition of new physics modules to the model. It also allows the modules to be swapped in and out for different planets, which is very valuable for simulating exoplanets that may have different processes at work in their atmospheres. Developing the new interface allowed more use of the object-oriented style of the cubed-sphere dynamical core, giving a better code structure than the previous latitude-longitude version.

A.1.3 Physics Modules

The default Exo-FMS setup provides access to a number of different physics modules. These are separate to the GFDL cubed-sphere dynamical core, and are coupled to it through the physics interface described above. The simplest configuration applies dry convective adjustment, a Rayleigh drag at the surface, and semi-grey radiative transfer (Pierrehumbert, 2010). These modules were used for the simulations in Chapters 1, 2 and 3. The simulations in Chapter 4 use the more realistic radiative transfer model Socrates (Edwards and Slingo, 1996). It would be useful in the

future to couple the model to a moist convective adjustment scheme, or a chemical equilibrium model.

A.1.4 Utilities

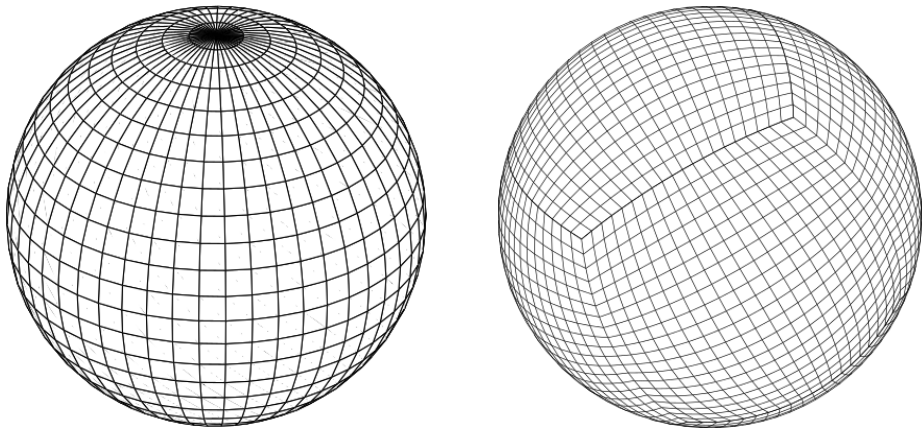
I also produced Python utilities to run the model and process its output. The Python interface to run the model writes the model runscript, the namelists containing the run parameters, and the diagnostic file containing the desired model outputs. It then re-grids the output fields from a cubed-sphere grid to a latitude-longitude grid for analysis using the “cubedsphere” Python package (<https://github.com/JiaweiZhuang/cubedsphere>).

A.2 Finite-Volume Dynamical Core

[Lin \(2004\)](#) describes the finite-volume dynamical core that simulates the fluid dynamics of the atmosphere. A finite-volume core (as opposed to a finite-difference core, or a spectral core) uses a grid of points, each with a surrounding volume that exchanges fluxes with the adjacent volumes.

A.2.1 Latitude-Longitude

The simulations in Chapter 3 used an older version of Exo-FMS from [Pierrehumbert and Ding \(2016\)](#). This version used a latitude-longitude grid, shown in Figure A.1a. It became clear that the poles of this grid were a source of instability, which is a common problem due to the decreased size of the grid cells there. To avoid these instabilities, and to provide an opportunity to simplify the model structure and remove legacy code, I upgraded the model to use a cubed-sphere grid.



(a) A latitude-longitude grid, showing the decreased cell size at the poles that can create instability.

(b) A cubed-sphere grid, with a smaller amount of variability in the cell sizes but six minor poles at the vertices of the cube.

Figure A.1: The old latitude-longitude grid and the new cubed-sphere grid used in Exo-FMS.

A.2.2 Cubed-Sphere

This cubed-sphere grid shown in Figure A.1b was used for the other simulations in this thesis, from the latest release (<https://www.gfdl.noaa.gov/cubed-sphere-quickstart/>) of the cubed-sphere dynamical core (Putman and Lin, 2007). A cubed-sphere grid is essentially a grid on the six faces of a cubed, projected onto the surface of a sphere. This creates six “poles” on the grid from the vertices of the cube, as well as small variations in the grid cell sizes. This can produces instabilities at the poles, or artifacts in the pattern of the grid (Putman and Lin, 2007), but these were never a serious issue in the simulations in this thesis.

APPENDIX B

Pseudo-Spectral Methods for the Shallow-Water Equations

In this appendix, I will describe the pseudo-spectral collocation methods used to solve the linearised shallow-water equations in Chapters 1 and 2. I will give a general description of a pseudo-spectral method, then show the methods I used to solve the shallow-water equations on the beta-plane and on a sphere.

B.1 Pseudo-Spectral Collocation Method for a Single Equation

A Pseudo-Spectral Collocation Method expands the solution to a partial differential equation or system of equations as a series of “basis functions” and then imposes the condition that the equation is satisfied at a number of “collocation points” (Boyd, 2000). The resulting matrix equation provides the coefficients of the series and therefore a solution to the initial equation.

For a linear ordinary differential equation:

$$Lu = q \quad (\text{B.1})$$

where L is a differential operator acting on the variable u , and q is the forcing or eigenvalue term, the solution is written as a sum of a series of basis functions:

$$u(x) = \sum a_n \psi_n(x) \quad (\text{B.2})$$

We impose the condition that the differential equation is satisfied at N “collocation points”, the positions of which depend on the set of basis functions.

This is equivalent to specifying that the “residual” – the difference between the exact solution and the pseudo-spectral series solution – is zero at these points. This provides N equations to solve for the N unknowns a_n , which gives the matrix equation:

$$\mathbf{H}\mathbf{a} = \mathbf{f} \quad (\text{B.3})$$

where matrix elements H_{ij} are the operator L applied to the modes ϕ_j at the collocation points x_i , and the vector elements f_i are the terms q evaluated at the collocation points x_i :

$$H_{ij} = L\phi_j(x_i) \quad (\text{B.4})$$

$$f_i = q(x_i) \quad (\text{B.5})$$

Solving Equation B.3 gives the coefficients a_n of the solution $u(x)$. For a system of equations rather than a single equation, L is a matrix and u and q are vectors.

B.2 Beta-Plane Shallow Water Equations

The shallow-water equations on the beta-plane can be solved directly without reduction to a tidal equation. This allows the use of parabolic cylinder functions to represent each variable, which correspond to the exact solutions with zero background flow. So, while the above solution of the tidal equation with Chebyshev functions applies more generally, this specific solution with parabolic cylinder functions can be exactly correct and can provide more insight into the effect of background flow on the modes of the system.

We can apply the same method as above to a system of equations rather than a single equation. For a system of forced, time-independent equations:

$$\mathbf{Lu} = \mathbf{q} \quad (\text{B.6})$$

The condition that the differential equation is satisfied at the collocation points gives the equivalent matrix equation to Equation B.3:

$$\mathbf{Ha} = \mathbf{f} \quad (\text{B.7})$$

\mathbf{H} is an $M \times N$ square matrix with elements:

$$H_{ij}^{kl} = L^{kl} \phi_j(x_i) \quad (\text{B.8})$$

i.e. the operator L^{kl} which acts on the l th variable in the k th equation, applied to the j th basis function and evaluated at the i th collocation point. \mathbf{f} is a vector made up of N subvectors f_i , which are the forcing terms in each equation evaluated at each collocation point.

$$\mathbf{H} = \begin{pmatrix} \begin{pmatrix} H_{ij} & \dots \\ \vdots & \ddots \\ \vdots & \ddots \end{pmatrix}^{kl} & \dots \\ \dots & \begin{pmatrix} \alpha_i \\ \vdots \\ \vdots \end{pmatrix} \end{pmatrix} = \begin{pmatrix} \begin{pmatrix} f_i \\ \vdots \\ \vdots \end{pmatrix} \end{pmatrix} \quad (\text{B.9})$$

\mathbf{H} is the same as the matrix in Equation B.4 with the elements H_{ij} replaced by submatrices H_{ij}^{kl} . Solving this system returns the coefficients of the basis functions, and the solutions are:

$$u(y) = \sum_{n=0}^N a_n \phi_n; \quad v(y) = \sum_{n=0}^N b_n \phi_n; \quad h(y) = \sum_{n=0}^N c_n \phi_n \quad (\text{B.10})$$

This gives a linear matrix equation with one solution corresponding to the coefficient vectors a_n, b_n, c_n of the forced solution.

Without forcing, the shallow-water equations define an eigensystem where the eigenvalue is the frequency ω .

$$\mathbf{Lu} = \omega \mathbf{Pu} \quad (\text{B.11})$$

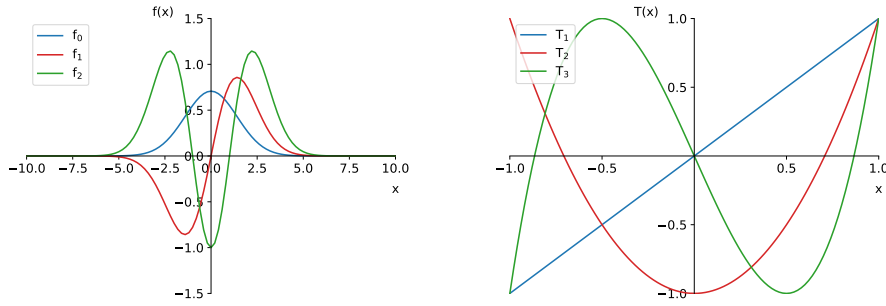
The pseudo-spectral equation is then:

$$\mathbf{Ha} = \omega \mathbf{Ra} \quad (\text{B.12})$$

\mathbf{R} is an $M \times N$ square matrix with elements:

$$R_{ij}^{kl} = P^{kl} \phi_j(x_i) \quad (\text{B.13})$$

i.e. the eigenvalue operator P^{kl} acting on the l th variable in the k th equation, applied to the j th basis function and evaluated at the i th collocation point.



(a) Parabolic Cylinder Functions

(b) Chebyshev polynomials.

Figure B.1: The basis functions used for the pseudo-spectral methods to solve the shallow-water equations on a beta-plane and on a sphere.

$$\mathbf{H} = \begin{pmatrix} \begin{pmatrix} H_{ij} & \dots \end{pmatrix}^{kl} & \dots \\ \vdots & \ddots \\ \vdots & \ddots \end{pmatrix} \begin{pmatrix} \alpha_i \\ \vdots \\ \vdots \end{pmatrix} = \omega \begin{pmatrix} \begin{pmatrix} R_{ij} & \dots \end{pmatrix}^{kl} & \dots \\ \vdots & \vdots & \ddots \end{pmatrix} \begin{pmatrix} \alpha_i \\ \vdots \\ \vdots \end{pmatrix} \quad (\text{B.14})$$

This gives an eigenvalue matrix equation, with N eigenvalues and eigenvectors, corresponding to the frequencies and coefficient vectors a_n, b_n, c_n for each free mode. Not all N modes must be physically realistic, so we identify the spurious modes by inspecting the eigenvalues for different values of N .

B.3 Spherical Shallow-Water Equations

This method is used in Chapters 1 and 2 to solve the shallow-water equations on a sphere. These equations are undefined with respect to u and v at the poles (although real solutions do exist), so we cannot solve for all the variables simultaneously as on the beta-plane. Instead, we reduce the three shallow-water equations to one equation in ϕ , also known as “Laplace’s Tidal Equation”. This equation can be solved with a pseudo-spectral method, and then used to find the solutions for u and v .

The linear shallow-water equations on the sphere are:

$$\begin{aligned}\frac{\partial u'}{\partial t} + \frac{\partial(\bar{u}u')}{a \cos \theta \partial \lambda} + v' \frac{\partial \bar{u}}{a \partial \theta} - \frac{\bar{u}v' \tan \theta}{a} &= 2\Omega v' \sin \theta - \frac{g \partial h'}{a \cos \theta \partial \lambda} \\ \frac{\partial v'}{\partial t} + \frac{\partial(\bar{u}v')}{a \cos \theta \partial \lambda} + \frac{2\bar{u}u' \tan \theta}{a} &= -2\Omega u' \sin \theta - \frac{g \partial h'}{a \partial \theta} \\ \frac{\partial h'}{\partial t} + v' \frac{\partial \bar{h}}{a \partial \theta} + \bar{u} \frac{\partial h'}{a \cos \theta \partial \lambda} + \bar{h} \nabla_H \cdot \mathbf{v}' &= 0,\end{aligned}\quad (\text{B.15})$$

where h is the height of the layer, $\mathbf{v} = (u, v)$ is the velocity, θ is latitude, λ is longitude, t is time, a is radius, g is gravity, and Ω is angular velocity. Overbars denote zonal-mean quantities (the background flow and height \bar{u} and \bar{h}). Dashes denote perturbations to this background state.

The background state is stationary and in gradient wind balance:

$$\frac{1}{a} \frac{\partial}{\partial \theta} (\bar{h} + h_g) = - \left(2\Omega \bar{u} \sin \theta + \frac{\bar{u}^2}{a} \tan \theta \right). \quad (\text{B.16})$$

The perturbed variables are wavelike in longitude and are uniformly damped, so are proportional to $\exp[i m \lambda + \alpha t)$. All variables are made non-dimensional with velocity scale $2\Omega a$, height scale $(2\Omega a)^2/g$ and time scale $1/(2\Omega)$, and denoted as such by an asterisk. This gives the following non-dimensional shallow-water equations:

$$\begin{aligned}\alpha^* u_m^* + im \frac{\bar{u}^* u_m^*}{\cos \theta} + v_m^* \frac{\partial \bar{u}^*}{\partial \theta} - \bar{u}^* v_m^* \tan \theta &= v_m^* \sin \theta - \frac{im h_m^*}{\cos \theta}, \\ \alpha^* v_m^* + im \frac{\bar{u}^* v_m^*}{\cos \theta} + 2\bar{u}^* u_m^* \tan \theta &= -u_m^* \sin \theta - \frac{\partial h_m^*}{\partial \theta}, \\ \alpha^* h_m^* + im \bar{u}^* \frac{h_m^*}{\cos \theta} &= -\frac{\epsilon^*}{\cos \theta} \left[imu_m^* + \frac{\partial}{\partial \theta} (\cos \theta v_m^*) \right],\end{aligned}\quad (\text{B.17})$$

where Lamb's parameter is $\epsilon \equiv (2\Omega a)^2/gH$.

These can be written as

$$\begin{aligned}-\hat{\sigma}^* u_m^* - \bar{\zeta}^* v_m^* + \frac{mh_m^*}{\cos \theta} &= 0, \\ \hat{\sigma}^* v_m^* + f_1^* u_m^* + \frac{dh_m^*}{d\theta} &= 0, \\ \hat{\sigma}^* \epsilon \alpha h_m^* + \frac{mu_m^*}{\cos \theta} + \frac{1}{\cos \theta} \frac{d}{d\theta} (\nu \cos \theta) &= 0,\end{aligned}\quad (\text{B.18})$$

where

$$\bar{\zeta}^* = f^* - \frac{1}{\cos \theta} \frac{d}{d\theta} (\bar{u} \cos \theta) \quad (\text{B.19})$$

is the absolute vorticity of the background flow,

$$f_1 = f + 2\bar{u} \tan \theta \quad (\text{B.20})$$

is an effective Coriolis parameter modified by the background flow, and

$$\hat{\sigma}^* = \sigma^* - \frac{m\bar{u}}{\cos \theta} \quad (\text{B.21})$$

is the Doppler-shifted time-derivative of the variables (see Chapter 2).

Solving the first two shallow-water equations gives the two velocity components in terms of the height field:

$$\begin{aligned} u_m^* &= \frac{-\hat{\sigma}^* h_m^* m / \cos \theta - \bar{\zeta}^* dh_m^* / dy}{\Delta} \\ v_m^* &= \frac{\hat{\sigma}^* dh_m^* / dy + f_1^* h_m^* m / \cos \theta}{\Delta} \end{aligned} \quad (\text{B.22})$$

where $\Delta = f_1^* \bar{\zeta}^* - \hat{\sigma}^{*2}$.

Then, substituting these into the third shallow-water equation, while changing variables to $\mu = \sin \theta$ and $\phi_m^* = (1 - \mu^2)^{-m/2} h_m^*$ to avoid the polar singularities ([Iga and Matsuda, 2005](#)), gives:

$$\frac{\partial^2 \phi_m^*}{\partial \mu^2} - B(\sigma^*, \mu) \frac{\partial \phi_m^*}{\partial \mu} - A(\sigma^*, \mu) \phi_m^* = \frac{F(\theta, x)}{i\sigma} \quad (\text{B.23})$$

where

$$\begin{aligned}
A(\sigma^*, \mu) &\equiv \frac{1}{1 - \mu^2} \left[m(m+1) - m\mu \frac{1}{\Delta^*} \frac{\partial \Delta^*}{\partial \mu} + \epsilon \Delta^* \right. \\
&\quad \left. + \frac{m}{\Delta^* \hat{\sigma}^*} \left(f_1^* \frac{\partial \Delta^*}{\partial \mu} - \Delta^* \frac{\partial f_1^*}{\partial \mu} \right) \right] \\
B(\sigma^*, \mu) &\equiv \frac{1}{\Delta^*} \frac{\partial \Delta^*}{\partial \mu} + \frac{2\mu(m+1)}{(1 - \mu^2)} \\
\Delta^* &\equiv f_1^* \bar{\zeta}^* - \hat{\sigma}^{*2}
\end{aligned} \tag{B.24}$$

This equation is then solved with a pseudo-spectral method using the Chebyshev polynomials plotted in Figure B.1 ([Wang et al., 2016](#)).

The tidal equation can be modified to represent the beta-plane by setting $\cos \theta = 1$ and $f_1 = f$